Proceedings of the 18th CEReS International Symposium on Remote Sensing "Asian Network for Environmental Monitoring and Related Studies"

October 24, 2012

Center for Environmental
Remote Sensing (CEReS)
Chiba University, Japan

Proceedings of the 18th CEReS International Symposium on Remote Sensing "Asian Network for Environmental Monitoring and Related Studies"

October 24, 2012

Chiba University, Japan

Preface

The 18th CEReS International Symposium entitled "Asian network for environmental monitoring and related studies" was held on the Nishi-Chiba campus of Chiba University on October 24, 2012. The Center for Environmental Remote Sensing (CEReS) restarted in April 2010, in accordance with the second middle-term (2010-2015) of Chiba University, as one of the national centers for joint usage and research accredited by the Ministry of Education, Culture, Sports, Science and Technology. Originally CEReS was established in 1995 as a research center for nationwide collaboration of the academic community of remote sensing. In relation to various environmental issues, remote sensing is indispensable for solving various problems on regional as well as global scales. Through the joint research activities in both national and international arenas, CEReS is pursuing the goal of maximizing the use of remote sensing, and establishing a comprehensive information center for environmental research and problem solution. Also, in collaboration with the graduate schools of Chiba University, CEReS has contributed to educating and fostering students and young researchers in various disciplines of remote sensing. The CEReS International Symposium on Remote Sensing provides us with an important opportunity in which researchers in the field of remote sensing can directly communicate with each other. The following is a list of our recent symposia:

- The 9th CEReS International Symposium on Remote Sensing - Monitoring of Environmental Change in Asia- , December 16-17, 2003.
- The 10th CEReS International Symposium on Radiation Budged and Atmospheric Parameters Studied by Satellite and Ground Observation Data - Toward the Understanding of Long Term Trend in Asia, February 17-18, 2005.
- The 11th CEReS International Symposium on Remote Sensing - Maximization of the Use of Satellite Data for Understanding the Earth Environment, December 13-14, 2005.
- The 12th CEReS International Symposium on Remote Sensing - Global Estimation of Biomass Using the Next Generation Sensor, January 10, 2007.
- The 13th CEReS International Symposium on Remote Sensing - Disaster Monitoring and Mitigation in Asia, October 29-30, 2007.
- The 14th CEReS International Symposium and SKYNET workshop on Remote Sensing of the Atmosphere for Better Understanding of Climate Change, November 13-14, 2008
- The 15th CEReS International Symposium on Remote Sensing -Achievement and New Challenge of Environmental Remote Sensing -, December 15-16, 2009.
- The 16th CEReS International Symposium on Climate Change Studies through Activities of SKYNET and Virtual Laboratory for Climate Diagnostics, October 21-23, 2010.
- The 17th CEReS International Symposium on Microwave Remote Sensing for Environmental Diagnosis, March 1, 2012.
- The 18th CEReS International Symposium on Asian Network for Environmental Monitoring and Related Studies, October 24, 2012.

As can be seen from this list, various topics of remote sensing studies have been discussed in the series of CEReS Symposia. On the basis of such long-term activities of CEReS, the 18th CEReS international symposium was held to strengthen our coordinated efforts for establishing an Asian network for remote sensing as well as related studies. As director of CEReS, I sincerely hope that this symposium is recognized as one of the important cornerstones for the development of our network activity in the international arena related to environmental remote sensing.

December 17, 2012
Hiroaki Kuze
Director of CEReS

TABLE OF CONTENTS

ORAL SESSION

POSTER SESSION

CARBON SEQUESTRATION CAPACITY OF FORESTS IN BEIJING BASED ON MULTISOURCE DATA

Qi-Jing Liu and Guang-Hua Wang

Department of Forest Sciences, Beijing Forestry University, Beijing 100083, China
E-mail of first author: liuqijing@gmail.com, and second author: 312152897@qq.com

KEY WORDS: Mountain forest, urban forest, carbon storage, remote sensing, biomass expansion factor

ABSTRACT: Both satellite images and ground data were applied for extracting carbon storage and its changes in Beijing municipality, including 1) allometric equations for 12 tree species were established based on destructive sampling, 2) biomass expansion factors were extracted by fitting biomass against timber volume, 3) remote sensing models were established based on Landsat TM images, 4) carbon storage of mountain forest was estimated with the models for 2004 and 2009, respectively, by combining TM imagery with forest inventory data, and 5) carbon storage in urban area was estimated for 2005 and 2009, respectively, on the basis of urban tree census data. Prediction on carbon sequestration from 2011 to 2015 was also conducted. Carbon storages of mountain forest in 2004 and 2009 were 5.24 Tg C and6.16 Tg tC, respectively, and carbon densities were 12.0 tC/ha and 14.1 tC/ha, including roots. Carbon sequestration rate during the period of 2004--2009 was 0.42 tC/(ha•yr), and that of urban area was 0.24 tC/(ha•yr). By model prediction, carbon sequestration in mountain forest and urban trees for the five-year period of 2011—2015 was totally 0.96 Tg tC.

INTRODUCTION

Containing the changing climate is a common task for all countries in the world. Developing countries may face the obligation of reducing green house gas emission. Chinese government actively promised to mitigate CO2 emission thorough saving energy and expanding forest area. Countries all over the world, particularly the developed ones, are engaging in censusing carbon deposit in forest ecosystem, apparently in a bid to get carbon credits, as well as the evaluation effects of forest management.

Fro carbon accounting, there are a number of approaches to measure and predict carbon storage and baance in forest ecosystem. From individual trees to regional scales, carbon storage can be estimated with different methods, including allometric equations, stand survey and remote sensing. Ground survey and empirical models are essential for scale transforming. Among all, species-specific biomass models for many tree species are yet to be established.

The current study focuses on the following aspects. (1) To extract basic parameters for measuring carbon storage, in addition to accuracy improving. (2) To estimate forest carbon storage and sequestration capacity. (3) To establish remote sensing models for carbon storage accounting in Beijing municipality.

METHODS

Study area is the entire Beijing municipality, including urban and rural areas. The total area is 163 thousand km^2 with extents of 160 km in south-north and 176 km in east-west. The mountain area accounts for 61.3%, and the rest is plain. Forest coverage is 46.55% or 0.469 million ha. Most area is under 200 m in elevation, with the peak at 2303 m. The main forest types are *Pinus tabulaeformis* forest, *Byota orientalis* forest, and *Quercus mongolica* forest.

Data included ground data and remote sensing images. Ground data included forest inventory data (2005), urban tree census data of 2005 (number of stems only), and tree census of central urban area of 2009 (with DBH distribution). As for remote sensing data, Landsat-5 TM/ETM images (2001.09 and 2009.09) were adopted.

Allometric equations for 12 tree species, and biomass expansion factors for eight forest types were established by destructive harvesting. Regressive models were built for eight forest types in pixel scale, and equations with high coefficients of regression were selected for estimating regional carbon storage. Based on carbon storages in two times with an interval of 5 years, the carbon increase capacity in the study area was calculated. TM images were rectified in both topographic and atmospheric effects before regression analysis against biomass.

RESULTS

Biomass models

Allometric equatios showed significant correlations with P values <0.0001 and regression coefficients >0.8, as listed in Table 1. As for biomass expansion factor, the linear relationship between biomass and timber volume showed high regression coefficients $R > 0.9$ and $P<0.0001$, as listed in Table 2. Remote sensing models are listed in table 3.

Table 1. Allometric equations for 12 tree species in Beijing

Species	Sample	DBH(cm)	α	β
Pinus tabu.	32	4.5-34.8	-2.1735	2.2461
Quercus mong.	31	3.7-28.9	-1.6324	2.2638
Quercus varia.	24	5.4-25.2	-1.9100	2.3080
Populus dav.	28	5.9-38.9	-2.8450	2.5682
Betula pla.	29	4.7-21.3	-2.6587	2.4305
Juglans man.	25	4.8-23.0	-1.1770	1.9544
Robinia pseu.	26	4.7-24.2	-2.4786	2.4201
Byota orie.	27	3.3-33.0	-1.7245	2.0033
Pinus bung.	18	2.6-28.7	-1.9840	2.1459
Malus bacca	17	1.8-8.2	-0.5522	1.6895
Sophora japo.	18	6.6-14.5	-2.8816	2.3962
Syringa beij.	15	2.9-10.5	0.1711	1.1616

Allometric equation was in the form of $\ln(B) = \beta \times \ln(D) + \alpha$, where B is biomass (kg), D is diameter at breast height, β and α are parameters.

Table 2. Biomass expansion factors for eight forest types in Beijing

Forest type	Sample	a
Byota orie.	58	0.8125
Rbinia	38	0.7
Betula	48	0.665
Deciduous	113	0.6363
Quercus	85	1.166
Larix	61	0.4248
Populus	46	0.5763
Pinus tabu.	82	0.722

Biomass factor is in the form of $B= aV$, where B is biomass (t), V is timber volume (m^3), and a is parameter.

Table 3. TM-derived regression models for estimating carbon storage(t/ha) of eight forest types

Type	Plots	Model	R^2	Sig
Byota	25	$C_1 = 1.072 + 4.256Var_3 + 0.64Mean_4 - 0.016Aspect$	0.569	0.000
Robinia	17	$C_2 = -0.496 + 38.096TM_4 + 1.68Ent_5$	0.323	0.029
Betula	19	$C_3 = 22.784 + 144.304PVI - 80.144Sec_4$	0.429	0.011
Deciduous	24	$C_4 = 1.776 + 0.464Slope + 3.92Var_7$	0.424	0.003
Quercus	40	$C_5 = -4.128 + 28.608NDVI - 0.016Cor_4$	0.358	0.005
Larix	23	$C_6 = 14.448 + 1.2RVI - 0.704Mean_4$	0.587	0.000
Populus	25	$C_7 = 0.272 - 168.576PCA_3 + 2.88Var_5 + 26.992Sec_3$	0.459	0.004
Pinus	40	$C_8 = -9.2 + 1.216RVI + 3.248Var_5 + 56.528Sec_5$	0.632	0.000

TM_i is band i of TM image in reflectance. PCA_i represents the i-th component in principle component analysis. *Brightness, Greenness* and *Wetness* are same as literal meanings, derived from tasseled cap transformation. *DVI, RVI, NDVI, PVI* and *TSAVI* are vegetation index, ratio vegetation index, normalized vegetation index, vertical vegetation index and transformed soil-vegetation index, respectively. The following items are based on texture analysis: $Mean_i$—mean value in band i, Var_i—variance, Ent_i—entropy, Sec_i—secondary moment, Cor_i—correlation. For topographic elements, *Slope* and *Aspect* are same as literal meanings.

Carbon storage

Based on forest inventory data, total carbon storage in plantation and natural forest was 5.24 million tC in 2004. In 2009, by remote sensing, the storage was 6.16 million tC. Spatially, carbon density was high in plain area (central and southeast), and low in the mountain area. Carbon density ranged from 10 to 25 tC/ha, lower than the national average. The increase of biomass carbon in the five-year period was 529 tC or 0.24 tC/(ha·yr). Based on relative growth rate, the predicted carbon increase in the period 2011-2015 was 0.96 million tC.

DISCUSSION

Remote sensing is an effective approach for deriving carbon storage in large scales, which is time cost effective and time saving. The low carbon density in the study area implies that the forest quality needs to be improved, although the site conditions are not ideal for tree growth due to the shallow soil layer and poor nutrient contents. As to the accuracy of remote sensing simulation, there is much left to do for improving the capability for estimating regional carbon storage. (Reference omitted)

IDENTIFICATION OF LAND VEGETATION WITH SATELLITE DATA, LIDAR TECHNOLOGY AND UAV SYSTEM

K. Wikantika, S. Darmawan, P. Kandia, R. Ragajaya , F. Hadi, J. Tantra, D. Suwardhi, A.B. Harto

[1]Remote Sensing and GIS Research Group, Faculty of Earth Science and Technology, Bandung Institute of Technology
[2]Center for Remote Sensing, Bandung Institute of Technology
Gedung LabTek IX-C, 3rd Floor, Jl. Ganesha 10, Bandung (40132), Indonesia
Email: ketut@gd.itb.ac.id, wikantika@yahoo.com

1 Introduction

Over the past few decades, evidence has mounted that planetary-scale changes are occurring rapidly. These are, in turn, changing the patterns of forcings and feedbacks that characterise the internal dynamics of the Earth System. Key indicators, such as the concentration of CO2 in the atmosphere, are changing dramatically, and in many cases the linkages of these changes to human activities are strong (Steffen & Tyson, 2004).

The Earth system components consist of land, ocean, and atmosphere. They interfaces between them (land-ocean, land-atmosphere, ocean-atmosphere). The earth is dynamically changing due to a combination of external forcing - gravity force, radiation of solar and a large and complex array of feedbacks and forcings within Earth's environment itself. The internal dynamics of the system is what keeping the earth a planet habitable for life. As time goes by, changes happens on these main part of the earth, they affect the functioning of the Earth system. There are global, regional and local changes.

It is increasingly clear that the Earth System is being subjected to a wide range of new planetary-scale forces that originate in human activities, ranging from the artificial fixation of nitrogen and the emission of greenhouse gases to the conversion and fragmentation of natural vegetation and the loss of biological species. It is these activities and others like them that give rise to the phenomenon of global change (Steffen & Tyson, 2004).

Global changes affect regional level and local level as well. The accumulation of local changes will affect regional scale, and finally this will affect it globally. These changes need to be monitored and observed so that we can study the dynamical changes, also for prevention and preparation for the further situation that might be the result from them that are affecting human life.

Because of that, the need of tools or methods to identify the changes are necessary. There are many approaches can be done in order to indentify or observe the earth, field calculation would give the near-real result of the earth changes, but conventional action has many flaws in it, for example, for a large scale area it will be time consuming, high in budget, and the amount of human resource needed would not be effective and efficient. One of the widely used method now is geospatial technology, one of them is remote sensing approach (Ragajaya et al., 2012).

Remote sensing can identify phenomenon or object in multi-temporal, multi-sensor, multi-scale approaches. Remote sensing can give accessibility on monitoring large vegetation field. It acts as a data source that can give reliable information with a large coverage area. One of the information that can be obtained using remote sensing technology is vegetation index. With the use of visible light sensor and near-infrared sensor, we can calculate the vegetation index of an area. The vegetation index is used to estimate the plants age and its condition (Tantra et al., 2012).

This paper focus on three main subjects that has been observed using a few technologies of remote sensing. First is biomass estimation using the image of ALOS-PALSAR. Secondly is modeling individual oil palm trees with LiDAR technology, and lastly, monitoring sugar-cane plantation using UAV (Unmanned Aerial Vehicle) system.

2 Application of radar data, LIDAR and UAV system

2.1. Biomass Estimation Using Polarimetric ALOS-PALSAR Data

This experiment carried out at Subang area, West Java, by firstly calculating the biomass by doing in situ destructive and non destructive sampling where the frequency and intensity of the biomass is measured and observed. Followed by procurement of ALOS PALSAR satellite image data that covers the area of sampling. This is where the remote sensing technology is applied. In processing Radar image software is used to make the process multilook, filtering process, the process of geocoding and perform polarimetric decomposition to calculate and estimate the biomass. This procedure can be explained in the diagram below.

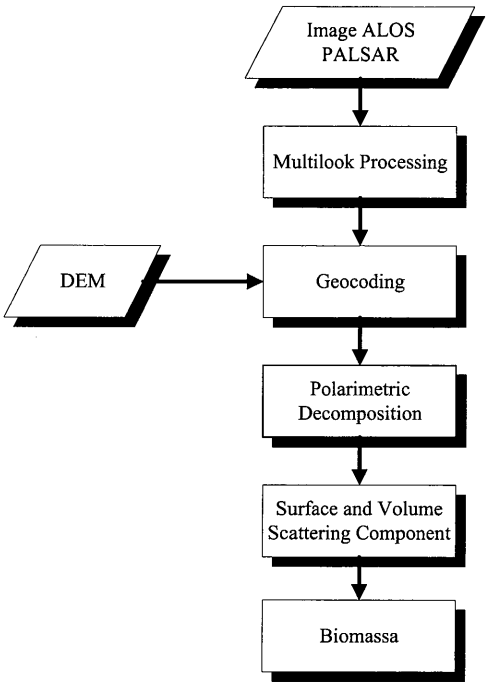

Figure 2. 1 Flowchart of the Biomass Estimation using Remote Sensing

Next is the modeling of WCM (Water Cloud Model) using mathematical equations to calculate stem volume and then converted to the amount of biomass. The basic concept of this equation is the interrelation between value of backscatter from forest and forest parameter.

Stem volume of a plant of forest equation is driven from Water Cloud Model. The value of biomass can be obtained and estimated from the number of stem volume by using the following method (Askne et al., 2003).

Biomass = 0,6 x *stem volume* (1)

Polarimetric decomposition is based on a model according to mechanism of scattering (scattering). Practically, there are many types of polarimetric decomposition models, one of which was Freeman Decomposition.

Lastly, analyse the data used to calculate and estimate the amount of biomass, data processing, and the results that have been obtained from the calculation of the biomass (Ragajaya et al., 2012).

2.2. Modeling individual oil palm trees with LiDAR technology

This research use LiDAR data which in the process consist of four main parts, where the sensor laser transmitting infra-red light to earth surface and record its reflectance. Then GPS is used to determine aircraft posisition and the 3D coordinate of the aircraft can be driven. IMU is used to measure the attitude of the aircraft, this complete the parameter of Radar position when obtaining the data, lastly is photos taken from the aircraft using ditigal camera in order to get orhophoto. LiDAR data processing begins with the process of data classification.

The data obtained in the form of point clouds data and must be grouped. This stage is divided into two phases namely the semi-automatic classification and manual classification. Point clouds will be divided into four classes of ground points, vegetatiton low, medium and high vegetation vegetation. This process also uses orthofoto true color.

Then the class of point clouds will be processed and interpolated to obtain a two-dimensional raster DTM and DSM. Point cloud on ground classes will be processed into DTM and high grade point cloud on vegetation at the highest point hit Z will be processed into DSM. Once the process of decreasing the pixel values in raster between DSM and DTM is done, thus obtained Canopy Height Model (CHM). CHM is the height difference between the surface of the tree canopy and the soil surface, the height of the tree.

The statistics in the form of distribution of the height of the tree can be used as a parameter to perform the detection and calculation of the amount of palm oil. This process is performed using Terrasolid Software. This method can be seen in the diagram below (Kandia et al., 2012).

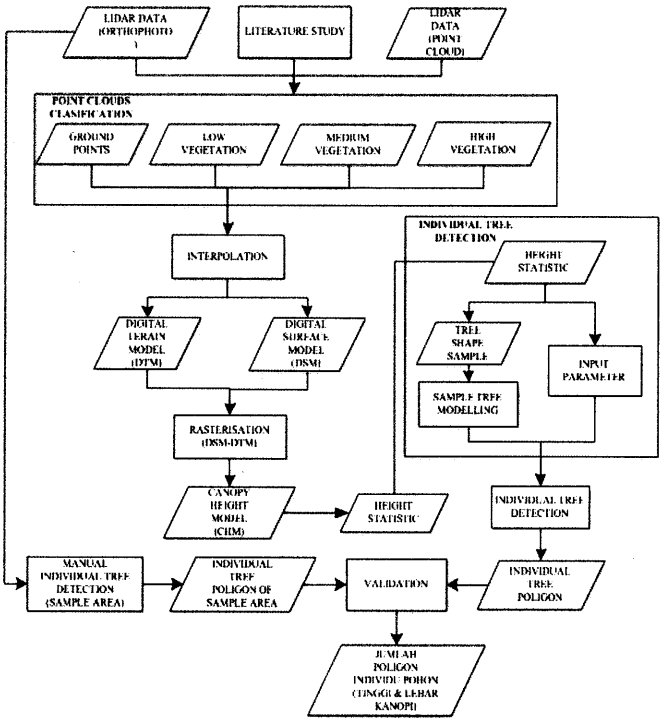

Figure 2. 2 Flowcharts of LiDAR for Oil Palm Tree Modeling

2.3. Monitoring sugar-cane plantation by UAV system

Study Sites

The study site for this experiment is Trangkil sugar factory's sugarcane field located on Pati, Central Java. The total size of the sugarcane field is about 12.000 Ha that spread between latitude 6° 24,3' S – 6° 59,3' S and longitude 110° 39,7' E - 111° 37,6' E.The experiment carries out on four different locations which is Trangkil, NgepungRejo, Babalan, and Puluhan Tengah. 200 Ha of area is observed on each location. These locations was selected because of their high heterogeneity of sugarcane field's age, on each location exist 2 month old sugarcane until 12 month old sugarcane field.

Remote Sensing Data

The observations carry out by using unmanned aerial vehicle as the platform that is equipped with a true color camera and a near-infrared camera. For the true color camera we use Canon E90 and for the near-infrared camera we use a modified Canon PowerShot SX230 HS that was added near-infrared sensor in it. Our near-infrared camera has 3 bands which is near-infrared, green and blue. The flight plans were carefully planned to ensure all of the selected areas are covered, the required overlap is reached, and the desired resolution is reached.

The mosaic orthophoto then processed to produce vegetation index of observed area. That vegetation index then will be correlated to sugarcane age. The commonly used vegetation index is Normalized Digital Vegetation Index (NDVI). However in this experiment we use a different vegetation index in order to avoid mistakes from imperfectly overlayed mosaic.

Enhanced Normalized Digital Vegetation Index (ENDVI) is used because it only requires input data from our single near-infrared camera. This mathematical model is proposed by the producer of the near-infrared camera, the equation is:

$$ENDVI = \frac{(NIR+GREEN)-(2\times BLUE)}{(NIR+GREEN)+(2\times BLUE)} \quad (2)$$

Where NIR is the digital number value of near-infrared band, BLUE is the digital number value of blue channel, and GREEN is the digital number value of green band. By using that equation, there is no need to use the true color mosaic. However the true color mosaic is still needed for visual interpretation.

Field Data

Other than photogrammetric data that have been discussed before, we collect data directly from the field. These data contain information about location of each sample and information related to the condition of sugarcane plant such as age, varietals, BRIX value and chlorophyll. BRIX is a value (in percent) of number of solid material that is dissolved in the sugarcane's sap. Nonetheless, there is no correlation between BRIX and chlorophyll with ENDVI value. Therefore, these variables will no longer discussed (Tantra et al., 2012).

3 Results

3.1. Biomass Estimation Using Polarimetric ALOS-PALSAR Data

The results of this study in the form of a table value μ and the amount of biomass on primary, and sparse forest landcover, landcover estate, residential landcover and landcover waters are presented in the appendix. In addition it is shown also chart comparison between the values of μ and the amount of biomass to determine the relationship. The results of the total biomass for primary forest landcover was 2815.33 tons, for a rare forest landcover was 563.21 tons, for landcover plantation was 316.96 tons, for settlement landcover was 68.80 tons, while for landcover waters is 21.65 ton.

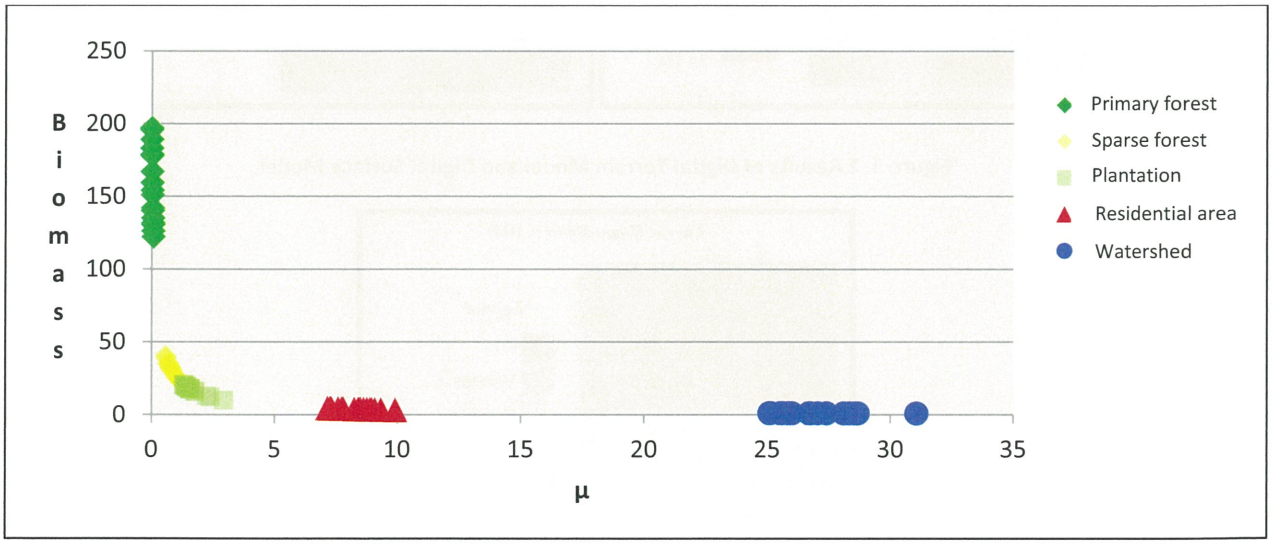

Figure 3. 1 Comparison of μ and the number of biomass

3.2. Modeling individual oil palm trees with LiDAR technology

The average height of the CHM namely 12.5 meters, with a value range between -0.5676 meters to 17.8 meters and a minimum height of 3 meters. In this study, the results obtained DTM and DSM has been considered both shown with accuracy LiDAR has quantified until level 15 cm and 30 cm, and the classification of point cloud is already using the best parameters and refined by manual classification to perform brush that point classified into class -defined classes. The result that the DTM height intervals in the range of 60-80 m and DSM 60 m up to 94 m. But when there is a high CHM extract minus trees, views of the value contained 226 pixel raster value in the amount of 204 683 value of only 0.1%. This is most likely due to the low points on LiDAR Data. Low points called noise (fault / disturbance) on LiDAR. The solution eliminates the low points should be point clouds on the data that has value minus CHM is also grouped into a new class, the class of Low Points, then the in-class and will not delete appears again when generate the DTM, DSM and when extracting CHM.

Table 3. 1 The Results of the Classification Statistics of Point Clouds

Class	*Description*	*Points*
1	*Default*	0
2	*Ground*	136.420
3	*Low Vegetation*	10.274
4	*Medium Vegetation*	8.100
5	*High Vegetation*	445.451
6	*Building*	0
	Total points	**600.245**

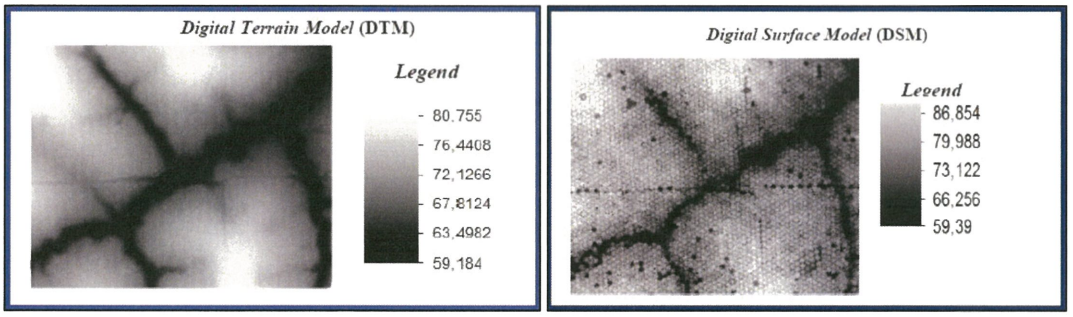

Figure 3. 2 Results of Digital Terrain Model and Digital Surface Model

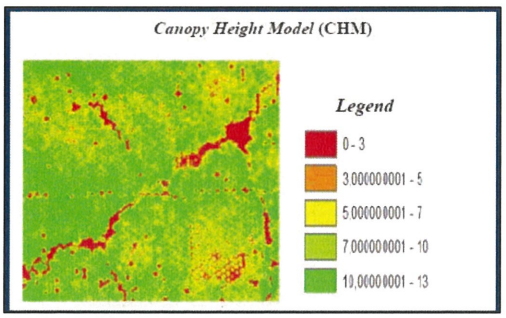

Figure 3. 3 Canopy Height Model

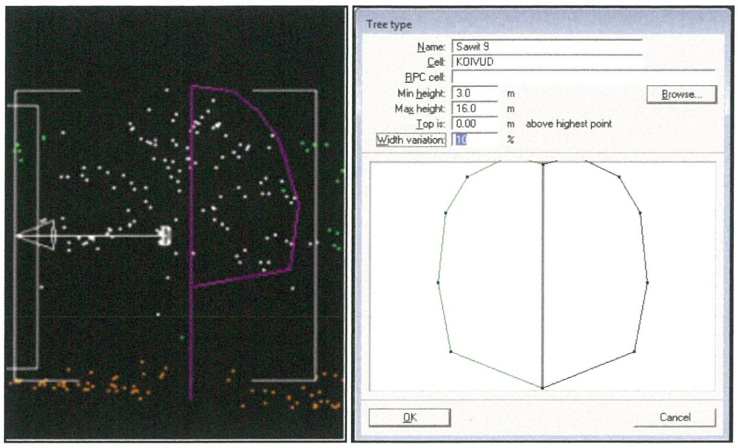

Figure 3. 4 Point Clouds Sample Model and Individual Tree Model

The model is formed using sample of point clouds, which is from individual trees in the study area. Further step is the model follows point cloud distribution.

3.3. Monitoring sugar-cane plantation by UAV system

Figure 3. 5 True Color Mosaic Orthophoto of Babalan Area (Left) and Near-Infrared Mosaic Orthophoto of Babalan Area (Right)

Based on the true color mosaic orthophoto we can visually interpret the object on the image and differentiate sugarcane field's age. Using the near-infrared mosaic orthophoto, we calculate its ENDVI value using scientific image processing software.

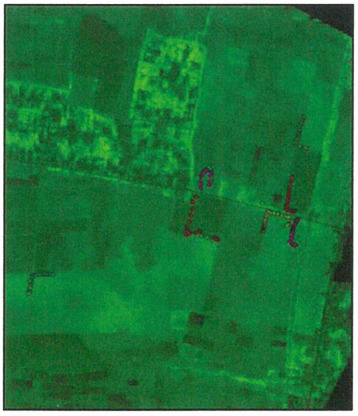

Figure 3. 6 ENDVI Image With Plotted Sample Points

From the calculated ENDVI and field data, we get the correlation of ENDVI value and sugarcane age as follow:

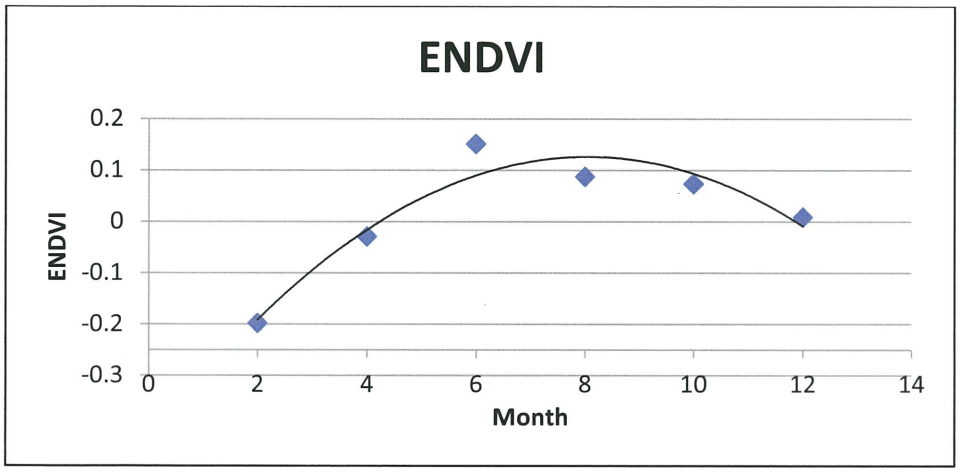

Figure 3. 7 ENDVI Graph

As we can see from the figure above, different sugarcane age can have the same ENDVI value. One ENDVI value can be passed twice, first when the sugarcane is in vegetative phase (0-6 month) and the second is on generative phase (6-12 month). Therefore, firstly we must interpret visually whether the sugarcane field is on vegetative phase or generative phase before we use ENDVI value to estimate the sugarcane's age.

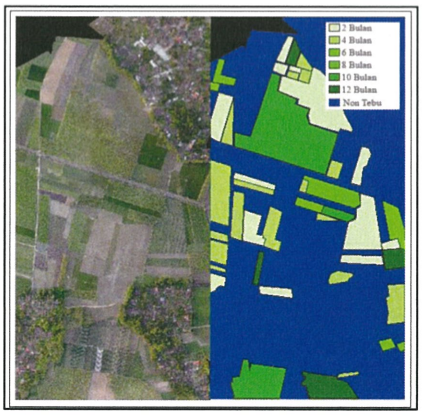

Figure 2.2 1 Sugarcane field age estimation thematic map

4 Conclusion

It has been shown that various platforms of remote sensing technology can be used in many applications. The changes of the earth represents in many aspect of characteristic area and environmental problem, to observe and study, those aspects need to be considered to determine the method and technology used in order to obtain satisfying results with effective and efficient approach.

5 Reference

Askne et al. (2003). Multitemporal Repeat-Pass SAR Interferometry of Boreal Forests. *IEEE Transactions on Geosciences and Remote Sensing* , Vol 41, No.7.

Kandia, P., Wikantika, K., & Budi Harto, A. (2012). *Pembentukan Model dan Parameter untuk Estimasi Kelapa Sawit Menggunakan Data Light Detection and Ranging (LiDAR) (Studi Kasus : Perkebunan Kelapa Sawit, Sumatera Selatan).* Bandung Institute of Technology.

Ragajaya, R., Wikantika, K., & Hadi, F. (2012). *Perhitungan Biomassa Dengan Metode Polarimetrik SAR Menggunakan Citra ALOS PALSAR.* Bandung: Bandung Institute of Technology.

Steffen, W., A., S., & Tyson, P. D. (2004). *Global Change and the Earth System.* IGBP Secretariat.

Tantra, J., Suwardhi, D., & Darmawan, S. (2012). *Sugarcane Field's Age Identification and Monitoring.* Bandung: Bandung Institute of Technology.

Aerosol climatology of the East Asia region studied by using ground-based remote sensor data of SKYNET network

Pradeep Khatri[1] and Tamio Takamura[2]

[1]CEReS, Chiba University, Chiba, Japan, Email: pradeep@restaff.chiba-u.jp

[2]CEReS, Chiba University, Chiba, Japan, Email: takamura@faculty.chiba-u.jp

Abstract

With the aim of better understanding the optical characteristics of the East Asian aerosols and their climatological impacts, we analyzed multiyear data collected at typical sites of SKYNET network that represent aerosols of different origins and backgrounds. Aerosol optical parameters and their climatic impacts in the urban areas were observed to vary spatially and temporally having different values of aerosol optical parameters and heating rate. This study suggests that the Asian dust aerosols near the source region may have weak light absorption capacity and weak heating rate. For the study conducted in biomass burning active area, we noted the existence of optically thicker small size ranged aerosols having signification contribution in aerosol heating rate during biomass burning season. By analyzing data collected at the East China Sea region, the study suggests that, especially in the spring season, air masses from the arid and urban regions of the Asia may transport aerosols of different origins to cause the aerosols of this region optically thicker and more light absorptive in nature that can have strong heating rate.

1. Introduction

Aerosols, the suspended particles in our atmosphere, are known to have adverse effects on human health, agriculture, visibility reduction, climate change and so on. In the field of atmospheric science, aerosols are being studied for last several years because they are known to influence the Earth`s climate directly and indirectly. The physical, chemical, and radiative characteristics of such aerosol particles are known to vary spatially and temporally. Such characteristics of aerosols have made it difficult to understand the roles of aerosols on regional and global climate change. However, understanding the roles of aerosols on regional and global climate change is important to not only atmospheric scientists, but also to policy makers and general public.

The East Asia is recognized as one of the important sources of both anthropogenic and natural aerosols. The aerosols emitted from this region can transport over long distances

to cause significant direct and indirect climate forcing to change the Earth's climate on regional and global scale (Khatri et al., 2010; Takamura et al., 2007; Nakajima et al., 2007). Because of the complicated nature of the East Asian aerosols and their potential impacts on regional and global climate change, the atmospheric and climate research communities have paid their attention to understand the physical, chemical, and optical characteristics of aerosols of this region. As a result, several field studies, such as Transport and Chemical Evolution over the Pacific (TRACE-P) (Jacob et al., 2003), Asian Pacific Regional Aerosol Characterization Experiment (ACE-Asia) (Hubert et al., 2003), Asian Atmospheric Particle Environmental Studies (APEX) (Nakajima et al., 2003), Atmospheric Brown Cloud East Asian Regional Experiment 2005 (EAREX 2005) (Nakajima et al., 2007) had been conducted in this past in this region. Though those field observations performed detailed investigations about aerosol particles of this region, the study periods were limited at specific locations. As the aerosols vary spatially and temporally, it is necessary to use long term observation data of multiple locations for the purpose of understanding the characteristics of the East Asian aerosols and their roles on regional climate in detail. Such type of study has become possible now because of the existence of SKYNET network. SKYNET (http://atmos.cr.chiba-u.ac.jp/) is a network for observations of aerosols, clouds, radiation, and meteorological parameters. This network has a various kinds of instruments at different parts of the Asia and Europe. Data collected at different sites by various types of the instruments are transferred to the data server of Chiba University through different ways. The observation data of this network have been widely used to understand aerosol climatology in regional and/or global scale as well as to validate several data products obtained from satellite sensors and numerical model simulations. Among several instruments in this network, the sky radiometer, manufactured by PREDE Co. Ltd. Japan, is the key instrument to monitor columnar aerosols. This instrument is similar to the CIMEL sun photometer of AERONET, which is operated by NASA. In this study, we study the optical characteristics of the East Asian aerosols and their roles on atmospheric heat budget by using long term observation data of sky radiometer collected at different SKYNET sites.

2. Instrumentation and Data

The sky radiometer can measure spectral direct and diffuse intensities at predefined scattering angles and wavelengths. Presently there are two models of sky radiometer: POM-01 and POM-02. The POM-01 and POM-02 instruments can measure direct and diffuse intensities up to 7 and 11 wavelengths, respectively. POM-02 is the improved version, which can be even used to measure cloud optical thickness. Generally, the wavelengths, in which the absorptions caused by atmospheric gases are negligible, are chosen in the sky radiometer for aerosol observations. The standard wavelengths for aerosol observation are 0.4, 0.5, 0.675, 0.87, and 1.02 microns for POM-01 and additional wavelengths of 0.34 and 0.38 microns for POM-02. An inversion program, named as Skyrad.pack (Nakajima et al., 1996), is available to derive columnar aerosol optical parameters such as, spectral aerosol optical thickness, single scattering albedo, asymmetry parameter, refractive indices as well as volume size distribution. Table 1 summarizes the observation sites, dominant aerosol types, model of the sky radiometer, and observation period for data used in this study. As shown in Table 1, we selected typical observation sites of SKYNET network that have aerosols of different characteristics and backgrounds. In this study, we used data collected at (i) five different urban areas, where human activities are dominant and aerosols are mainly anthropogenic, (ii) Dunhuang(40.146^{0}N,94.799^{0}E), China, where dust aerosols are dominant throughout the year, (iii) Phimai, Thailand(15.184^{0}N,102.565^{0}E), where biomass burning activities are in large numbers during the dry season, and (iv) Fukuejima, Japan(32.752^{0}N,128.682^{0}E), which is basically a remote site, but can receive long range transported aerosols from the continental regions of the East Asia. Data collected at above mentioned different sites, which represent typical atmospheric scenarios of the East Asia, allow us to study the optical characteristic of aerosols of different sources and their impacts on atmospheric heat budget.

3. Data analysis method

Skyrad.pack is the software package to analyze data observed by sky radiometer instrument. The theotrical background of the Skyrad.pack software is described by Nakajima et al. (1996). Figure 1 shows the standard data analysis procedure of sky radiometer instrument. In order to analyze sky radiometer data, at first, two calibration

constants, namely solid view angle ($\Delta\Omega$) and calibration constant for direct irradiance, i.e. V_0 are required. There are several methods to determine $\Delta\Omega$ in the laboratory as described by Nakajima et al. (1996). Similarly, V_0 is generally determined using Normal Langely method, which basically needs very high stable atmospheric condition and need to take the instrument to high mountains. Such techniques of determining $\Delta\Omega$ and V_0 are laborious, expensive, and time consuming.

Table 1. Site name, dominant aerosol type, sky radiometer model, and observation period for data used in this study.

Site (Latitude, Longitude)	**Dominant aerosol type**	**Instrument type**	**Observation period**
Chiba, Japan (32.625^0N,140.104^0E)	Anthropogenic aerosols	POM-02	2005/09-2011/02
Seoul, Korea (32.46^0N,126.949^0E)		POM-01	2005/11-2011/02
Pune, India (18.537^0N,73.805^0E)		POM-01	2004/01-2009/06
Delhi, India (28.629^0N,77.174^0E)		POM-01	2006/02-2007/04
Rome, Italy (41.905^0N,12.548^0E)		POM-01	2009/10-2011/02
Dunhuang, China (40.146^0N,94.799^0E)	Dust aerosols	POM-01	1998/10-2006/12
Phimai, Thailand (15.184^0N,102.565^0E)	Biomass burning aerosols in the dry season	POM-02	2005/01-2010/12
Fukuejima, Japan (32.752^0N,128.682^0E)	Marine and long ranged transported aerosols	POM-02	2006/03-2011/02

The greatest advantage of the sky radiometer instrument is that those calibration constants can be determined using normal observation data themselves. The sky radiometer uses disk scan method and Improved Langley method to determine $\Delta\Omega$ and V_0, respectively. The details of those methods are reported by Nakajima et al. (1996). In order to determine $\Delta\Omega$, disk scan data are required. They are data measured by the instrument by scanning the area of 2^0X2^0 around the solar disk form up to down and from left to right with an angular resolution of 0.1^0. The Skyrad.pack software package contains a program to calculate $\Delta\Omega$ using such disk scan data. Figure 1 shows the flow chart to calculate V_0. The method to calculate V_0 is denoted by solid black lines in Figure

1. In brief, after determining $\Delta\Omega$ using disk scan data, the measured direct and diffuse intensities up to the scattering angle of 30^0 are used in the Skyrad.pack inversion program along with data of surface reflectance, columnar ozone concentration, and atmospheric pressure to determine the optical thicknesses of aerosols, atmospheric gases, and ozone through radiative transfer simulation. From the latitude and longitude of observation area and local time, solar zenith angle (θ_0) can be calculated. θ_0 can be approximated to optical air mass(m_0) according to $m_0 = 1/\cos\theta_0$. Thus determined total optical thickness due to aerosols, atmospheric gases, and ozone and optical air mass(m_0) for observation data of certain days can be used with corresponding measured direct intensities to determine V_0. As V_0 is the important parameter for the estimate of volume size distribution and other important optical parameters such as, single scattering albedo, phase function, refractive indices etc, we applied a strict data screening criteria and estimate the monthly averaged V_0. From the time series of V_0 , one can also understand the possible problem in the instrument during observation. Basically, the time series of V_0 should not show up and down, but it may decrease linearly with the passage of time due to filter degradation. Thus determined V_0 for each month is then again used with sky radiometer observed direct and diffuse intensities up to maximum scattering angle, $\Delta\Omega$, surface reflectance, columnar ozone concentration, and atmospheric pressure data to calculate spectral aerosol optical thickness, single scattering albedo, and refractive indices as well as phase function and volume size distribution. The flow chart of this calculation is given by red solid lines in Figure 1. The quality check and cloud screening of thus retrieved aerosol optical parameters were done using the algorithm of Khatri and Takamura (2009). Thus obtained aerosol optical parameters were used in SBDART radiative transfer model (Ricchhiazzi et al. 1998) to estimate aerosol radiative forcing at the surface and top of the atmosphere (TOA) as well as heating rate.

It is important to note that the reported values in this study are analyzed using version 4.2 of Skyrad.pack software by using wavelength independent surface reflectance of 0.1 and constant ozone concentration of 0.3 atm-cm. Version 5.0 of Skyrad.pack software has been also developed recently. In future, we plan to analyze data using both versions 4.2 and 5.0 softwares with improvement in the data analysis technique. In the future, all data will be reanalyzed by using spectral surface reflectance from MODIS sensor and ozone

concentration from OMI sensor by keeping much strict criteria to select data while estimating monthly averaged V_0. Furthermore, the quality check of data will be performed by combing the cloud-screening algorithm of Khatri and Takamura (2009) and more additional data screening criteria of Hashimoto et al. (2012).

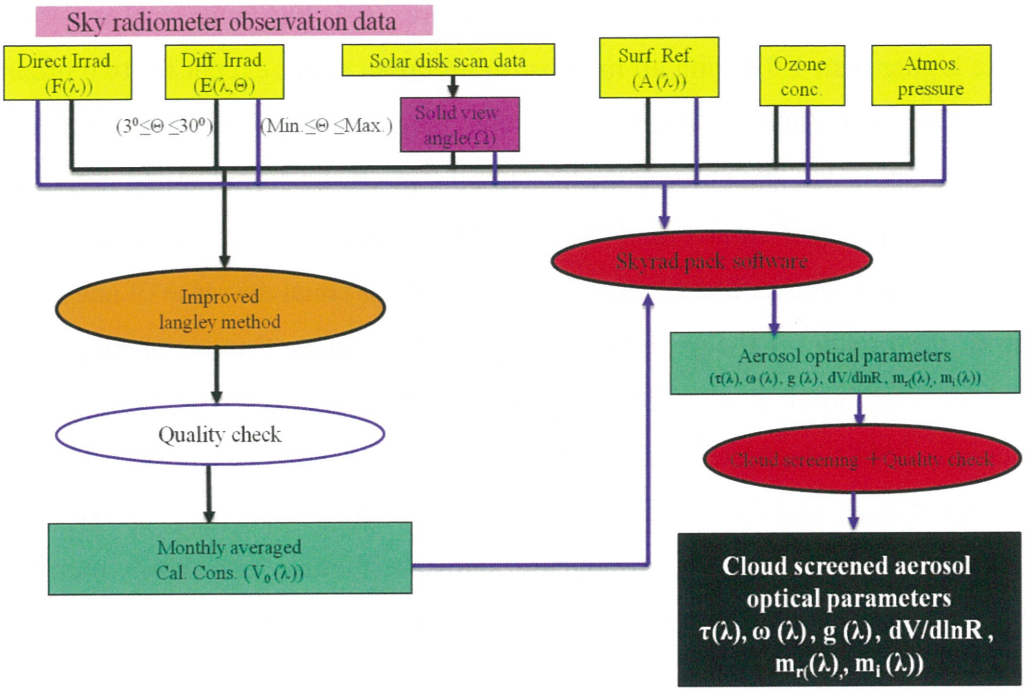

Figure 1. A standard data analysis procedure of sky radiometer.

4. Aerosol climatologies over different observation areas of different atmospheric scenarios

4.1. Urban area

Figure 2 shows the monthly variations of (a) aerosol optical thickness (AOT) at 500nm , (b) angstrom exponent, (c) single scattering albedo (SSA) at 500nm, (d) aerosol forcing at the surface, (e) aerosol forcing at the top of the atmosphere (TOA), and (f) aerosol heating rate for data collected at different urban sites of SKYNET network. In urban areas, generally aerosols are produced due to human activities. In Figure 2(a), we observed different values of AOT(500nm) at different urban areas, which was obvious as human activities and the level of air pollutants can be different at different regions. It is likely that values of AOT(500nm) are higher during summer months in comparison to

other months. This might be due to excess water vapor in the atmosphere in the summer months than other months. The water soluble aerosols can increase their size then AOT can be increased under such atmospheric condition. Figure 2(b) shows monthly variations of angstrom exponent. Angstrom exponent is a parameter describing the wavelength dependency behavior of AOT. Higher the angstrom exponent, smaller the size of dominant aerosols and vice versa. As shown in Figure 2(b), the values of angstrom exponent were higher than 1.0 during all months for all urban areas, except for two urban areas of India. The high values of angstrom exponent suggest the presence of relatively small size ranged aerosols. The anthropogenic aerosols produced from human activities in the urban areas are small in size and they can have such relatively large angstrom exponents. Interestingly, both urban areas of India show the gradual decrease of angstrom exponent up to the middle of the year and then gradual increase. Similar phenomenon was reported by Padithurai et al. (2008) for observations conducted at New Delhi. Padithurai et al. (2008) suggested that dust aerosols from Thar desert and vicinity gradually transport from March to June. Such mid range values of angstrom exponent suggest the mixture of dust and anthropogenic aerosols. Figure 2(c) shows monthly variations of SSA(500nm). We observed dissimilar values of SSA(500nm) at different months for different urban areas. As urban areas are the sources of both strong light absorbing aerosol, such as black carbon and strong light scattering aerosol, such as sulfate, SSA(500nm) depends on the relative amounts of such light scattering and absorption aerosols. In Figure 2(c), we observed large variations in SSA(500nm) during winter months and less variations in summer months among values of different urban areas. Noting that winter and summer months are generally dry and wet, respectively, the largely scatted values in the winter months for different urban areas may resemble the relative amount of light absorbing BC aerosol. Figures 2(d), 2(e), and 2(f) show the 24 hours averaged monthly variations of aerosol radiative forcing at the surface and top of the atmosphere (TOA) as well as heating rate, respectively. Those parameters depend on the values of aerosol optical parameters including, AOT, SSA, and angular distribution of phase function. Depending on the different magnitudes of aerosol optical parameters at different urban aerosol, their climatological impacts are different. For example, in Figure 2(a), we observed high and low values of AOT(500nm) in the urban atmospheres of

Rome and New Delhi, respectively. Because aerosol radiative forcing at the surface and TOA strongly depend on the values of AOT and SSA, we observed relatively low and high negative values of aerosol forcing at the surface and TOA in the urban atmospheres of Rome and New Delhi, respectively. The aerosol radiative forcing at the surface and TOA were found to be around -60Wm^{-2} and -30Wm^{-2} during May and June in the urban atmosphere of New Delhi, which were mainly due to relatively high values of AOT on those months. Aerosol radiative forcing is defined as the difference in the net (downward-upward) radiative fluxes with and without aerosols. The difference in the aerosol radiative forcing between surface and TOA is defined as the atmospheric forcing. The atmospheric forcing suggests the amount of energy absorbed in the atmosphere due to the existence of light absorbing aerosols. Such energy absorbed by light absorbing aerosols can be translated to heat the atmosphere. In Figure 2(f), the heating rates at different urban areas are shown. The heating rates for different urban areas were different because the amounts of energy trapped in the atmosphere were different on different urban areas due to the existence of aerosols having different optical characteristics.

4.2. Dunhuang, China

Figure 3 shows the monthly variations of (a)aerosol optical thickness (AOT) at 500nm , (b) angstrom exponent, (c) single scattering albedo (SSA) at 500nm, (d) aerosol forcing at the surface, (e) aerosol forcing at the top of the atmosphere (TOA), and (f) aerosol heating rate for data collected at Dunhuang, China(40.146^{0}N,94.799^{0}E) site of SKYNET network. Dunhuang is an arid region with dust as the dominant aerosol in the atmosphere. Recently, the light absorption capacity of Asian dust is a subject of debate. For observations conducted in the vicinity of the East China sea, some researchers reported relatively low SSA when significant dust aerosols arrived the observation area (e.g,. Nakajima et al., 2003; Khatri et al., 2011), though dust aerosols have been reported to have SSA as high as 0.95 (Nakajima et al., 1989; Kaufman et al., 2001). For understanding the optical characteristics of dust aerosols near the source region, data observed at Dunhuang are very useful. As shown in Figure 3(a), the aerosols in the Dunhuang region have high AOT during February to May. During this period, Asian

dusts emitted from the desert areas of Asia are often observed in the distances far from the source region. Figure 3(b) shows low values of angstrom exponent in all months. This

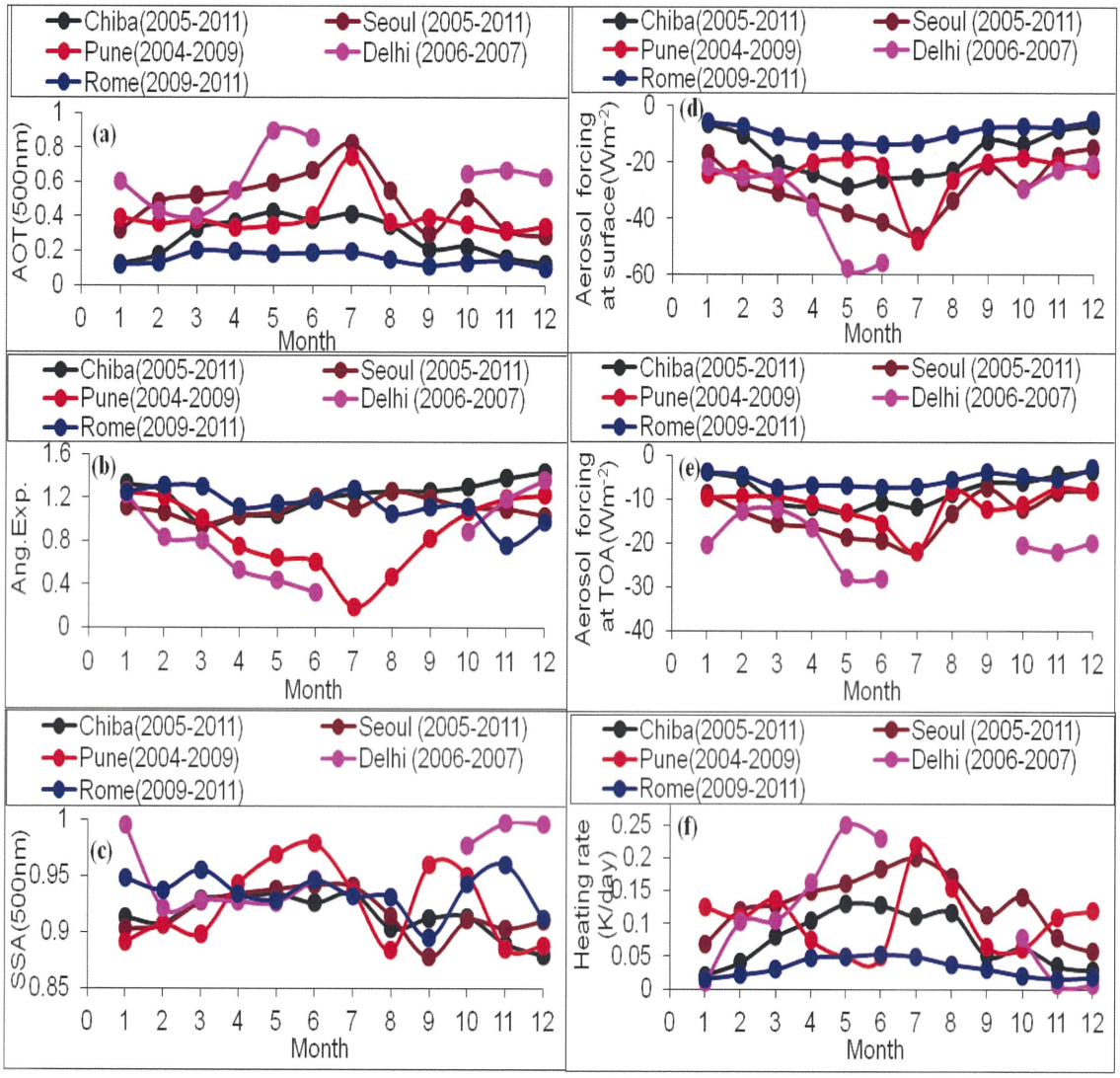

Figure 2. Monthly variations of (a)aerosol optical thickness (AOT) at 500nm , (b) angstrom exponent, (c) single scattering albedo (SSA) at 500nm, (d) aerosol forcing at the surface, (e) aerosol forcing at the top of the atmosphere (TOA), and (f) aerosol heating rate for data collected at different urban sites of SKYNET network.

suggests that coarse mode aerosols are dominant in this region throughout the year. Figure 3(b) further shows that the angstrom exponent further decreased during the period of February to May. In those months, we observed the increase of AOT(500nm) in Figure 3(a). This suggests that the large sized dust aerosols are emitted from the Asian dust

region during this period. Thus emitted dust aerosols then transport over long distances. Figure 3(c) shows the monthly variation of SSA(500nm). The values of SSA(500nm) were found to around 0.95 or higher than it during spring season, in which season dust aerosols are transported from desert areas to far distances. This quantitative value of SSA(500nm) observed in this study agrees with those reported by Nakajima et al. (1989) and Kaufman et al., (2001), suggesting that Asian dusts near the source region have relatively high SSA. This result gives some clues to explain the observed low SSA values by some studies (e.g., Nakajima et al., 2003; Khatri et al., 2011) during the arrival of dust aerosols in the East China Sea region. These observed relatively low SSA were likely due to a strong interaction between anthropogenic air pollutants and mineral dust aerosols (Chuang et al., 2003; Tang et al., 2004) during their transport from the source region because dust aerosols when transport from desert and arid regions of the Asia also push air pollutants out of the continents of the downstream area (Nakajima et al., 2007). Figures 3(d), 3(e), and 3(f) show the climatic effects of aerosols particles of this region. Because of optically thicker aerosols during February to May, we observed decrease in aerosol radiative forcing at the surface and TOA on those months in comparison to results for other months. As mentioned above, the difference in the aerosol radiative forcings at the surface and TOA denotes the amount of energy trapped within the atmosphere, which can be translated to heat the atmosphere. In this study, we observed the heating rate less than 0.1K/day during all months.

4.3. Phimai, Thailand

Phimai site of SKYNET network is regarded to be suitable site to study the optical characteristics of aerosols emitted from the biomass burning activities. In this region, biomass burning activities are in large number during dry season. Biomass burning activities generally produce small size ranged aerosols with light absorbing aerosols such as black carbon. In Figure 4, monthly variations of (a)aerosol optical thickness (AOT) at 500nm , (b) angstrom exponent, (c) single scattering albedo (SSA) at 500nm, (d) aerosol forcing at the surface, (e) aerosol forcing at the top of the atmosphere (TOA), and (f) aerosol heating rate are shown for data collected at Phimai (15.184^0N,102.565^0E), Thailand site of SKYNET network. As shown in Figures 4(a) and 4(b), we observed

distinct seasonal variations of AOT(500nm) and angstrom exponent. During the months having relatively high AOT(500nm), we observed relatively high values of angstrom exponent too. This suggests that the increase in AOT(500nm) in this region were caused by small size ranged aerosols, which were possibly emitted from biomass burning and/or other human activities in this region. Interestingly, we observed very high monthly AOT(500nm) up to around 0.7 with monthly averaged angstrom exponent of around 1.5

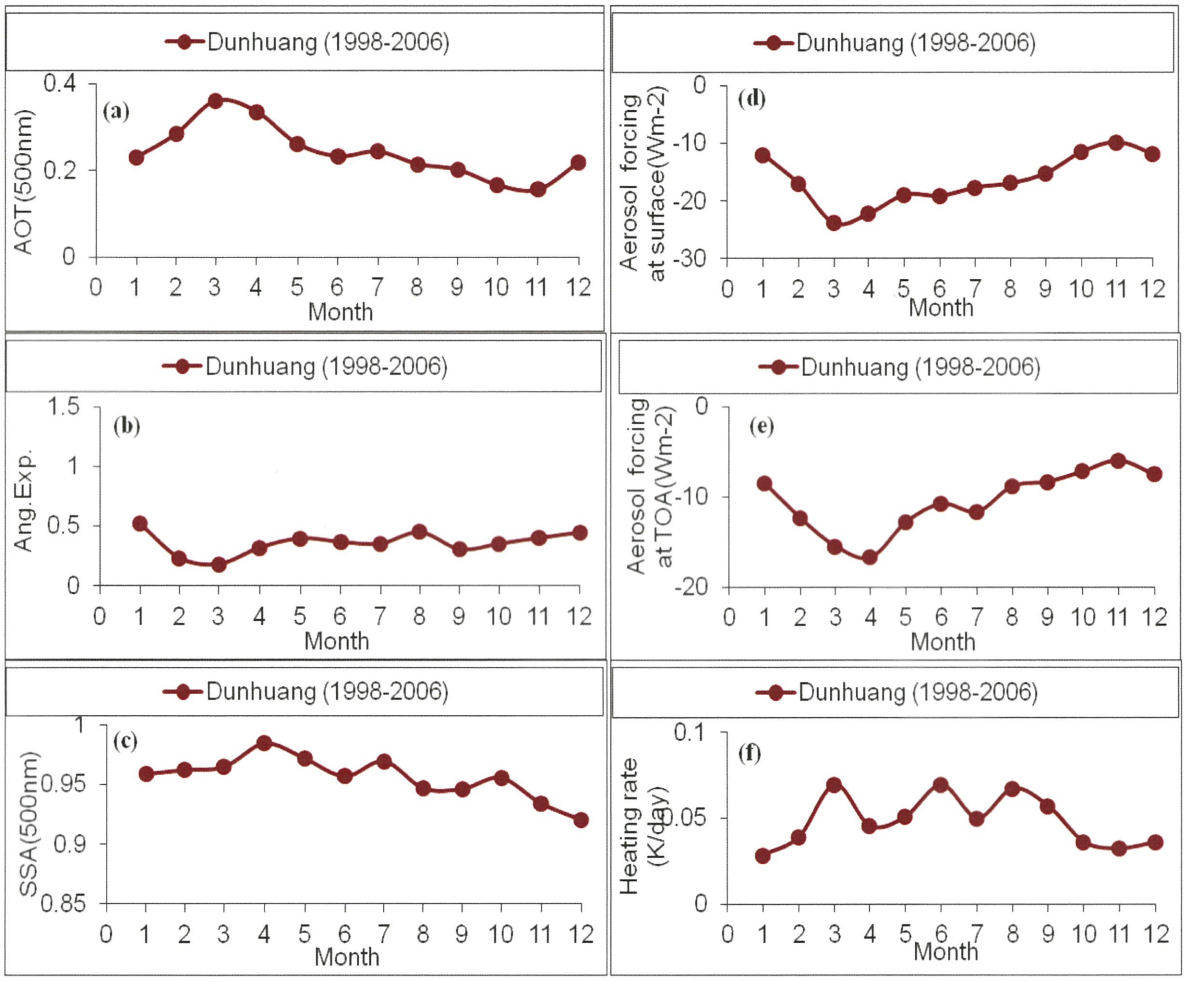

Figure 3. Monthly variations of (a)aerosol optical thickness (AOT) at 500nm , (b) angstrom exponent, (c) single scattering albedo (SSA) at 500nm, (d) aerosol forcing at the surface, (e) aerosol forcing at the top of the atmosphere (TOA), and (f) aerosol heating rate for data collected at Dunhuang, China(40.146^{0}N,94.799^{0}E) site of SKYNET network.

in March. After reaching the peak values on March, both AOT(500nm) and angstrom exponent started to decrease reaching the minimum values on July. Figure 4(c) shows the monthly variations of SSA(500nm). The sudden decrease of SSA(500nm) on August is not clearly known now. Except the SSA(500nm) value for August, other seasons show the value higher than around 0.93. Using the radiative transfer model, we calculated the aerosol radiative forcing at the surface and TOA as well heating rate. The aerosol radiative forcing at the surface decreased up to around -30Wm^{-2} on March whereas it was only around -10 Wm^{-2} on July when the monthly optical thickness was around 0.2. Due to the existence of optically thicker aerosols during February to April, the heating rates up to around 0.12K/day were observed in those months whereas the heating rate was only around 0.02 K/day in July.

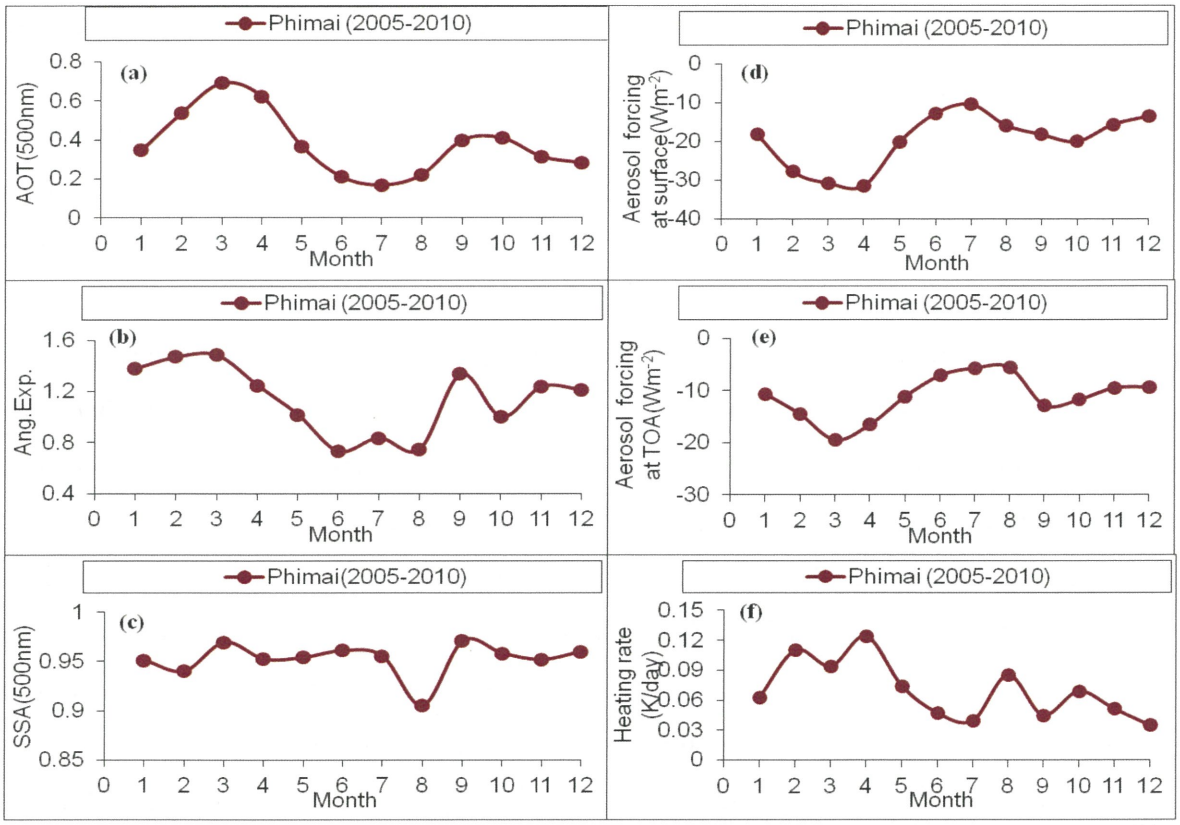

Figure 4. Monthly variations of (a)aerosol optical thickness (AOT) at 500nm , (b) angstrom exponent, (c) single scattering albedo (SSA) at 500nm, (d) aerosol forcing at the surface, (e) aerosol forcing at the top of the atmosphere (TOA), and (f) aerosol heating rate for data collected at Phimai (15.184^{0}N,102.565^{0}E), Thailand site of SKYNET network.

4.4. Fukuejima, Japan

Fukuejima(32.752^{0}N,128.682^{0}E) is the super site of SKYNET network, which is located in the Fukuejima island, Nagasaki, Japan. Basically, the observation site is located in the remote area, however, this site frequently receives aerosols transported from desert, arid, and continental regions of the East Asia. Figure 5 shows the monthly variations of (a)aerosol optical thickness (AOT) at 500nm , (b) angstrom exponent, (c) single scattering albedo (SSA) at 500nm, (d) aerosol forcing at the surface, (e) aerosol forcing at the top of the atmosphere (TOA), and (f) aerosol heating rate for data collected at Fukuejima(32.752^{0}N,128.682^{0}E), Japan site of SKYNET network. As shown in Figure 5(a), the monthly averaged AOT(500nm) were higher than around 0.3 during most of the months. Such high values of AOT(500nm) were not caused by emissions from local sources because there are no major sources of anthropogenic aerosols near the observation site. On the other hand, they were due to aerosols transported from long distances from the continental regions of Asia. In Figure 5(b), monthly variation of angstrom exponent is shown. As expected, we observed mid range values of angstrom exponents during March, April, and May in this observation site because a mixture of dust and anthropogenic aerosols are transported to this region in the spring season. The low angstrom exponent in July is not clearly known now. In general, fine mode aerosols are dominant in this region during all months except March, April, and May. The most striking information revealed from data of this site was that monthly SSA(500nm) values were around 0.9 or even lower than this. It indicates that aerosols of this region are light absorptive in nature. Recalling the fact that there are no major sources of anthropogenic aerosols in this region, such low SSA values in this study indicate that the air masses arriving this region or passing this region are from urban sectors of the Asia where productions of strongly light absorbing aerosol, such as black carbon, is significant. Due to the existence of optically thicker aerosols in this region, the aerosol radiative forcing vales at the surface were observed to take values lower than -20Wm^{-2}during most of the months. On the other hand, the aerosol radiative forcing values at TOA were around -10Wm^{-2} during most of the months. The difference of aerosol radiative forcing between the surface and TOA causes to heat the atmosphere. Comparing to other months, the

heating rates were higher during March, April, and May in this observation site. Heating rates in between 0.2K/day to 0.3K/day were observed during those months.

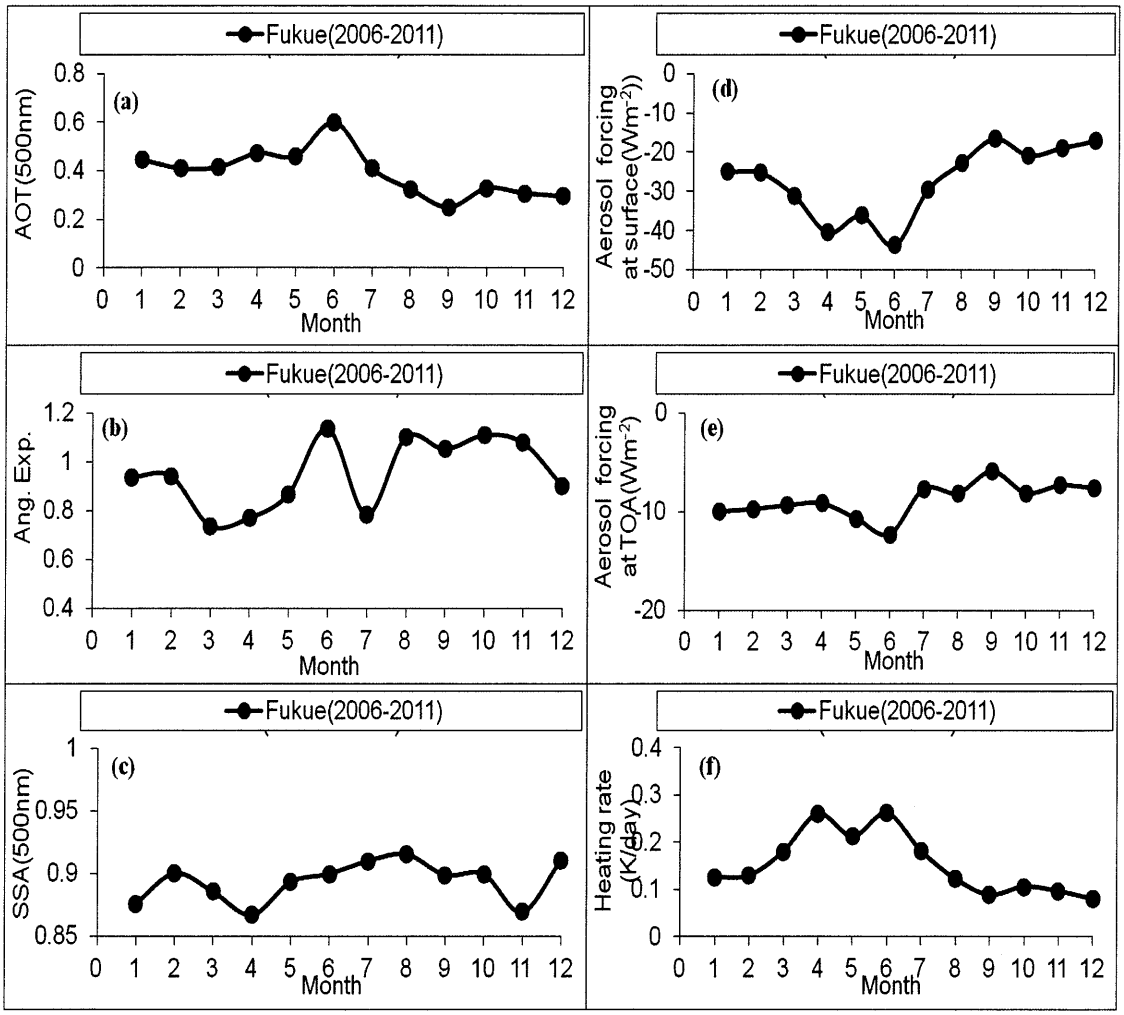

Figure 5. Monthly variations of (a)aerosol optical thickness (AOT) at 500nm , (b) angstrom exponent, (c) single scattering albedo (SSA) at 500nm, (d) aerosol forcing at the surface, (e) aerosol forcing at the top of the atmosphere (TOA), and (f) aerosol heating rate for data collected at Fukuejima(32.752^{0}N,128.682^{0}E), Japan site of SKYNET network.

5. Summary

East Asia is the major source of both natural and anthropogenic aerosols. Those aerosols are pointed to affect the climate system of our Earth in different ways. Because the aerosols vary spatially and temporally, it is necessary to use long term observation data of multiple locations of the East Asia to understand the characteristics of the East

Asian aerosols and their roles on atmospheric heat budget. In view of this recognition, this study used long-term observation data collected at typical sites of SKYNET network, which represent aerosols of different origins, to study the monthly variations of key aerosol optical parameters and the climatic effects of aerosols. In this study, we selected SKYNET sites located at urban areas, arid region, biomass burning region, and marine atmospheric region to cover aerosols of different types. For the study of urban aerosols, we selected Chiba(Japan), Seoul(Korea), Pune(India), New Delhi(India), and Rome(Italy). For reference, the Indian sites and European site outside of East Asian were chosen. The optical properties of aerosols and their roles on atmospheric heat budget were found to be different depending on the site. The SSA values at 500nm at those urban sites were found to range from 0.8 to around 1.0 depending on the observation site and season. Similarly, the aerosol heating rate due to absorption of light by aerosols also ranged from around 0.02K/day to around 0.25K/day, depending on observation site and season. For the study conducted by taking data of arid region of Dunhuang, which may be regarded as the suitable site to study the characteristics of Asian dust, we observed that Asian dust aerosols may have SSA at 500nm as high as around 0.95, suggesting that Asian dust aerosols themselves are weak in aerosol light absorption. From our observation data of Dunhuang, we found aerosol heating rate in between around 0.03K/day to 0.07K/day. For observations conducted in the Phimai, Thailand, where biomass burning aerosols are considerable in the dry season, we noted that both AOT and angstrom exponent can increase by the emission of relatively small size ranged aerosols in the dry season. The values of SSA at 500nm during dry season were observed to be around 0.94. The heating rate increased up to around 0.12K/day in the month with the highest AOT at 500nm, whereas the value was around 0.04K/day in the month with the lowest AOT at 500nm. Finally, a marine site named as Fukejima, which is located at the East China Sea region, was chosen to understand the effects of long range transported aerosols from far distances. Interestingly, we observed relatively high AOT and low SSA at 500nm during most of the months at this site, suggesting the strong influence of the air masses transported from the arid and urban regions of the Asia. The values of SSA at 500nm were observed to range in between 0.85 to 0.9. We further observed the mid range value of angstrom exponent in the spring season, suggesting the mixture of coarse and fine mode aerosols in

this season. The heating rate as high as around 0.25K/day was observed in the spring season in this region.

Acknowledgements

This research is supported by the Global Environmental Research Fund (B-083) of the Ministry of the Environment, Japan and "Virtual Laboratory for Diagnosing the Earth's Climate System" program of the Ministry of Education, Culture, Sports, Science and Technology (MEXT), Japan. This research is also performed as a part of SKYNET activities by the Observational Research Project for Atmospheric Change in Troposphere (GEOSS program) of the Ministry of Education, Culture, Sports, Science and Technology, Japan.

References

Chuang, P. Y., R. M. Duvall, M. S. Bae, A. Jefferson, J. J. Schauer, H. Yang, J. Z. Yu, and J. Kim (2003), Observations of elemental carbon and absorption during ACE-Asia and implications for aerosol radiative properties and climate forcing, *J. Geophys. Res.,108(D23), 8634*, doi:10.1029/2002JD003254.

Hashimoto, M., T. Nakajima, O. Dubovik, M. Campanelli, H. Che, P. Khatri, T. Takamura, and G. Pandithurai (2012), Development of a new data-processing method for SKYNET sky radiometer observations, *Atmos. Meas. Tech. Discuss.*, **5**, C2259–C2262.

Huebert, B. J., T. Bates, P. B. Russell, G. Shi, Y. J. Kim, K. Kawamura, G. Carmichael, and T. Nakajima(2003), An overview of ACE-Asia: Strategies for quantifying the relationships between Asian aerosols and their climatic impacts, *J. Geophys. Res., 108(D23), 8633*, doi:10.1029/2003JD003550.

Jacob, D. J., J. H. Crawford, M. M. Kleb, V. S. Connors, R. J. Bendura, J. L. Raper, G. W. Sachse, J. C. Gille, L. Emmons, and C. L. Heald (2003), Transport and Chemical Evolution over the Pacific (TRACE-P) aircraft mission: Design, execution, and first results, *J. Geophys. Res.,108(D20), 9000*, doi:10.1029/2002JD003276.

Kaufman, Y. J., D. Tanre, O. Dubovik, A. Karnieli, and L. A. Remer (2001), Absorption of sunlight by dust as inferred from satellite and ground-based remote sensing, *Geophys. Res. Lett.,28*, 1479–1482.

Khatri, P., and T. Takamura (2009), An algorithm to screen cloudaffected data for sky radiometer data analysis, *J. Meteor. Soc. Japan, 87*, 189–204.

Khatri, P., T. Takamura, A. Shimizu, and N. Sugimoto (2010), Spectral dependency of aerosol light-absorption over the East China Sea region, *Sci. Online Lett. Atmos, 6*, 1-4.

Khatri, P., T. Takamura, A. Yamazaki, Y. Kondo, A. Shimizu, and N. Sugimoto (2011), Light absorptive dust aerosols and their effects on atmospheric heat budget over the East China Se a region in the spring season, paper presented at 2011 Fall meeting of the meteorological society of Japan, Nagoya University, Nagoya, Japan, 16-18 Nov., 2011, 421.

Nakajima, T., M. Tanaka, M. Yamano, M. Shiobara, K. Arao, and Y. Nakanishi (1989), Aerosol optical characteristics in the yellow sand events observed in May, 1982 in Nagasaki, part II: Model, *J. Meteorol. Soc. Jpn.,67*, 279–291.

Nakajima, T., G. Tonna, R. Rao, P. Boi, Y. Kaufman and B. Holben (1996), Use of sky brightness measurements from ground for remote sensing of particulate polydispersions. *App. Opt.,* 35, 2672-2686.

Nakajima, T., M. Seguchi, T. Takemura, I. Uno, A. Higurashi, D. Kim, B. J. Sohn, S.-N. Oh, T. Y. Nakajima, S. Ohta, I. Okada, T. Tamakura, and K. Kawamoto (2003), Significance of direct and indirect radiative forcing of aerosols in the East China Sea region, *J. Geophys. Res.,108(D23), 8658*, doi:10.1029/2002JD003261.

Nakajima, T., S. –C. Yoon, V. Ramanathan, G. –Y. Shi, T. Takemura, A. Higurashi, T. Takamura, K. Aoki, B. –J. Sohn, S. –W. Kim, H. Tsuruta, N. Sugimoto, A. Shimizu, H. Tanimoto, Y. Sawa, N. –H., Lin, C. –T Lee, D. Goto, and N. Schutgens (2007), Overview of the Atmospheric Brown Cloud East Asian Regional Experiment 2005 and a study of the aerosol direct radiative forcing in east Asia, *J. Geophys. Res., 112*, D24S91, doi:10.1029/2007JD009009.

Pandithurai, G., S. Dipu, K. K. Dani, S. Tiwari, D. S. Bisht, P. C. S. Devara, and R. T. Pinker(2008), Aerosol radiative forcing during dust events over New Delhi, India, *J. Geophys. Res., 113*, D13209, doi:10.1029/2008JD009804.

Ricchiazzi, P., S. Yang, C. Gautier, and D. Sowle (1998), SBDART: A research and teaching software tool for plane-parallel radiative transfer in the Earth's atmosphere, *Bull. Am. Meteorol. Soc., 79*, 2101–2114.

Tang, Y., G. R. Carmichael, G. Kurata, I. Uno, R. J. Weber, C. –H. Song, S. K. Guttikunda, J., -H. Woo, D. G. Streets, C. Wei, A. D. Clarke, B. Huebert, and T. L. Anderson (2004), Impacts of dust on regional tropospheric chemistry during the ACE-Asia experiment: A model study with observations, *J. Geophys. Res.,109*, D19S21, doi:10.1029/2003JD003806.

Takamura, T., N. Sugimoto, A. Shimizu, A. Uchiyama, A. Yamazaki, K. Aoki, T. Nakajima, B. J. Sohn, and H. Takenaka (2007), Aerosol radiative characteristics at Gosan, Korea, during the Atmospheric Brown Cloud East Asian Regional Experiment 2005, *J. Geophys. Res., 112*, D22S36, doi: 10.1029/2007JD008506.

Takemura, T., T. Nakajima, A. Higurashi, S. Ohta, and N. Sugimoto (2003), Aerosol distributions and radiative forcing over the Asian-Pacific region simulated by Spectral Radiation-Transport Model for Aerosol Species (SPRINTARS), *J. Geophys. Res.,108(D23), 8659*, doi:10.1029/2002JD003210.

GLOBAL MONITORING OF ATMOSPHERIC METHANE SOURCES USING SATELLITE DATA

Jong-Geol Park[1] , Soo-Young Park[2] and Ippei Harada[3]

[1]Associate Professor, Tokyo University of Information Sciences
4-1 Onaridai, Wakaba-ku, Chiba, Japan; Tel: + 81-43-2364644;
E-mail: amon@rsch.tuis.ac.jp

[2]Postdoctor, Tokyo University of Information Sciences
4-1 Onaridai, Wakaba-ku, Chiba, Japan; Tel: + 81-43-2364639;
E-mail: tokyopark@hotmail.com

[3]Assistant, Tokyo University of Information Sciences
4-1 Onaridai, Wakaba-ku, Chiba, Japan; Tel: + 81-43-2364639;
E-mail: iharada@rsch.tuis.ac.jp

KEY WORDS: methane, global sources, SCIAMACHY, emission concentration, growth rate

ABSTRACT:

In this study, we determine the global emission concentration of methane using SCIAMACHY data. We analyzed land and sea area to investigate the nine-year changes in methane concentrations from 2003 to 2011. Moreover, by subtracting the concentration of methane from land and sea, we can found the methane emission concentration of land. As a result, it is cleared that a big amount of CH4 emission concentration was found not only in the Northern Hemisphere paddy fields but also in the Southern Hemisphere broadleaf evergreen areas (Central Africa and South America). And we also found that the global land CH4 growth rate is 3-5ppb/year during 9 years.

1. INTRODUCTION

A greenhouse gas is a gas in atmosphere that absorbs and emits radiation within the thermal infrared range. This process is the original cause of the greenhouse effect. The primary greenhouse gases in the Earth's atmosphere are water vapor, carbon dioxide (CO2), methane (CH4), nitrous oxide (N2O), and ozone (O3). Which from four of the principal greenhouses gases are human activities results (CO2, CH4, N2O, and the halocarbons). These gases increase concentrations of the long-lived greenhouse gases (LLGHGs). Greenhouse gases affect the temperature of the Earth. Since the beginning of the Industrial Revolution, the burning of fossil fuels have contributed to the increase in carbon dioxide in the atmosphere from 280ppm to 390ppm, despite the uptake of a large portion of the emissions through various natural "sinks" involved in the carbon cycle. In the past few years, many workers have noted that the combined effect on climate of the increase in the concentrations of a large number of trace gases could rival or even exceed the increasing concentration of carbon dioxide. Atmospheric CH4 is the second most important anthropogenic greenhouse gas after CO2. CH4's mixing ratio has increased by a factor of 2.5 compared to preindustrial levels and reached almost 1,800 ppb today. The direct radiative forcing of anthropogenic CH4 is 0.48W/m2 that is almost one third that of anthropogenic CO2 (1.66W/m2) [5]. CH4 emissions are separated into anthropogenic and natural sources. According to Lelieveld et al. (1998) and IPCC (2001), natural sources amount is only one-third of the total CH4 emission budget, which the most important natural source is wetland. Anthropogenic sources account for the other two-thirds of the total CH4 emission budget, with the most important being energy consumption (coal mining and combustion, oil- and gas-related emissions), domestic ruminants and waste treatment, rice paddies, biomass burning, landfills and waste water. A study from Nisbet et al. (2009) suggests that the emission of methane from plants under normal conditions is due to the transport of water containing dissolved methane from the soil to the atmosphere through transpiration. Transpiration could help to explain the satellite-observed methane enhancement over the tropical regions of South America and some of the published ground-based measurements (Carmo 2005, Miller 2007). Recent studies have proposed that there is an additional significant CH4 source that could radically impact the current CH4 budget estimates. Keppler et al. (2006) suggested that living plants with CH4 emissions (aerobic) 10–40% of the total annual source, may be a major CH4 source on a global scale. Wang et al (2008) have confirmed that some plant species emit methane under aerobic condition in the Inner Mongolia steppe. After a decade of near stable concentrations, the growth rate of atmospheric methane has started to increase again.

Recently SCIAMACHY (launch 2002) and GOSAT (launch 2009) enabled precise measurements of atmospheric CH4 from space. Unfortunately the global source strength of CH4 remains uncertain. In this study, we will focus on CH4 sources of global area using these satellite data, vegetation map and MODIS NDVI to investigate the characteristics of this CH4 sources.

2. DATA

The World Data Centre for Greenhouse Gases (WDCGG) is one of the WDCs under the Global Atmosphere Watch (GAW) program. It serves to gather, archive and provide data on greenhouse gases (CO2, CH4, CFCs, N2O, surface ozone, etc.) and related gases (CO, NOx, SO2, VOC, etc.) in the atmosphere and ocean, as observed under GAW and other programs. Vegetation Index (VI) have trended to estimate a large number of vegetation properties such as LAI, biomass, chlorophyll concentration in leaves. The enhanced vegetation index(EVI) is an `optimized` index designed to enhance the vegetation signal with improved sensitivity in high biomass region and improved vegetation monitoring and reduction in atmosphere influences. Global Land Cover by National Mapping Organization (GLCNMO) has twenty land cover classes using 16-day composite MODIS data of 2003.The SCanning Imaging Absorption spectroMeter for Atmospheric CHartographY (SCIAMACHY) instrument (Burrows 1995) is a part of the atmospheric chemistry payload of the European Space Agencies (ESA) environmental satellite ENVISAT, launched in March 2002. SCIAMACHY is the first satellite instrument that measures near-infrared spectra in the 1–2.4μm spectral range from space at high spectral resolution. The SCIAMACHY near-infrared spectra contain atmospherically interesting molecules such as CH4, CO2, CO, and H2O, of which the bulk resides in the troposphere. Retrieval algorithms applied to this wavelength range include the Iterative Maximum A Posteriori-DOAS (IMAP-DOAS) algorithm (Frankerberg 2005). The Greenhouse Gases Observing Satellite (GOSAT) instrument was launched in January 2009 with the aim of measuring the column amounts of CO2 and CH4. GOSAT has a CO2 target to achieve 4 ppm accuracy for a three month regional average using a combination of short-wavelength infrared (SWIR), and infrared (IR) channels (Kuze 2009).

3. ANALYSIS AND RESULT

3.1 Data process

Frankenberg's method was used to reduce cloud effect from SCIAMACHY data. By using a cloud free pixel data, a 15-day composite data was made to understand the CH4 source and its circulation. In addition, this data was spatially and temporally interpolated.

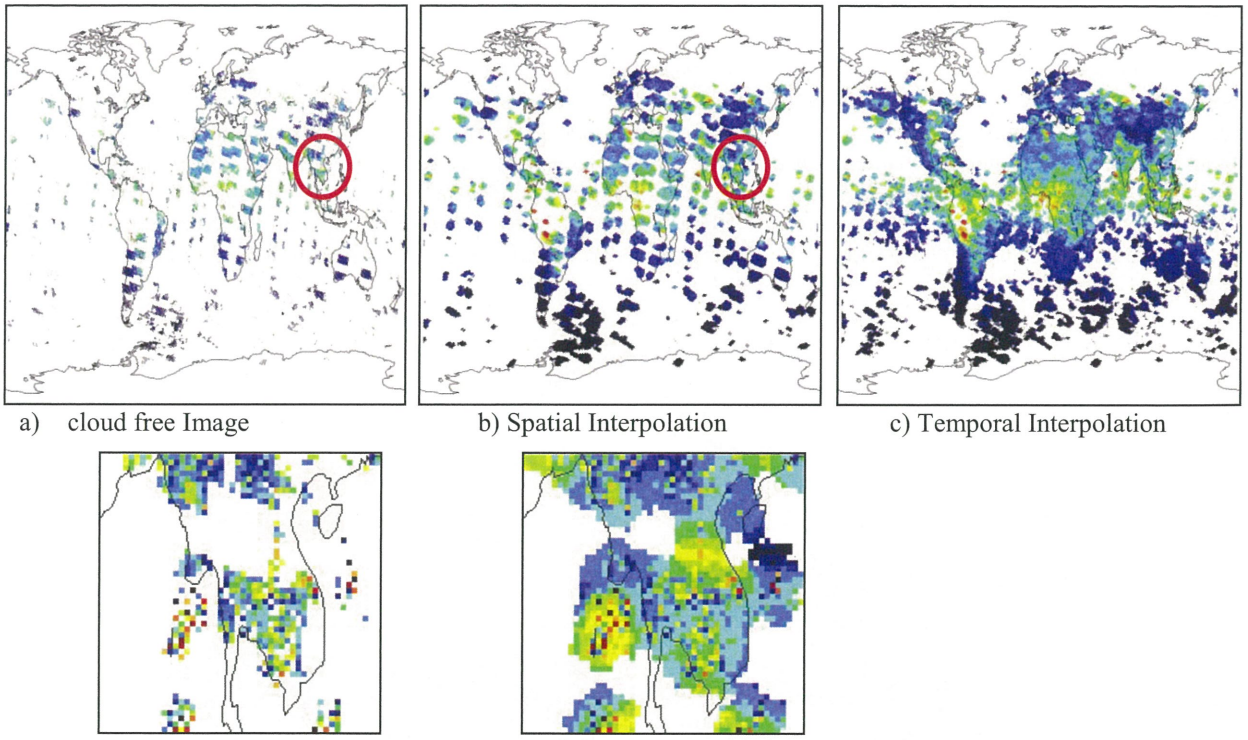

a) cloud free Image b) Spatial Interpolation c) Temporal Interpolation

Figure1. Cloud Free and Interpolation CH_4 concentration SCIMACHY

As a result, the data was made up in 24 scenes per year during a period from 2003 to 2011. After removing the clouds, GOSAT data was distributed as a monthly data. Cloud free GOSAT data is valid because of the use of Thermal And Near infrared Sensor for carbon Observation-Cloud and Aerosol Imager (TANSO-CAI). GOSAT can only provide us four years of data, which is not sufficient, so we use it as SCIAMACHY data supplement (Figure 1).

3.2 Change in methane concentration on land

Figure 2 shows the concentration of CH_4 by terrestrial latitude band for nine years. CH_4 concentration in the Northern Hemisphere mid-latitude regions is higher than other regions. It increased approximately by 20ppb from 2003 (1750ppb) until 2011(1780ppb).Mainly in September, the high concentration areas are distributed on the paddy fields of Asia. It shows that in the rice harvest period, CH_4 concentration raised up to 1780ppb max. CH_4 concentration in the high latitudes of the north hemisphere is 1680ppb, near the equator is 1740ppb and in the south hemisphere is lower than 1670ppb. After 2007 every year, from January to February, it becomes clear that the CH_4 concentration was increasing near the equator. There were no concentration changes of CH_4 from 2003 to 2006 but from 2007 to 2011 we understand that it was increasing.

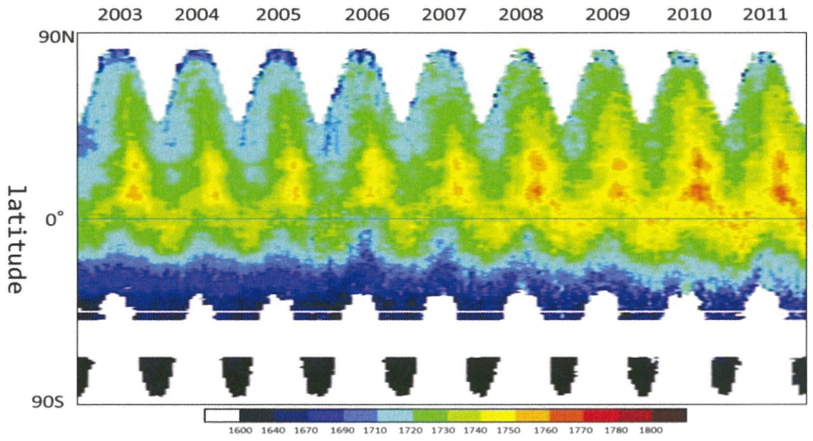

Figure 2. Land methane concentration in time series from 2003 to 2011

3.3 CH4 emission concentration

CH4 emission concentration is defined as the emission of land CH4 concentration. Time series changes in the CH4 concentration of land can be relatively compared. it is difficult to compare the CH4 emission concentration because of the different background concentration of CH4. Therefore, we can assume that a very small amount of CH4 is emitted from the sea surface, that CH4 concentration of the sea is used as a same latitude background. The difference of CH4 concentration between land and sea is equal to the CH4 emission concentration of land at the same latitude(Figure 3). As a result, it is cleared that a big emission concentration of CH4 was found not only in the Northern Hemisphere paddy fields but also in the Southern Hemisphere broadleaf evergreen areas (Central Africa and South America)(Figure 4).

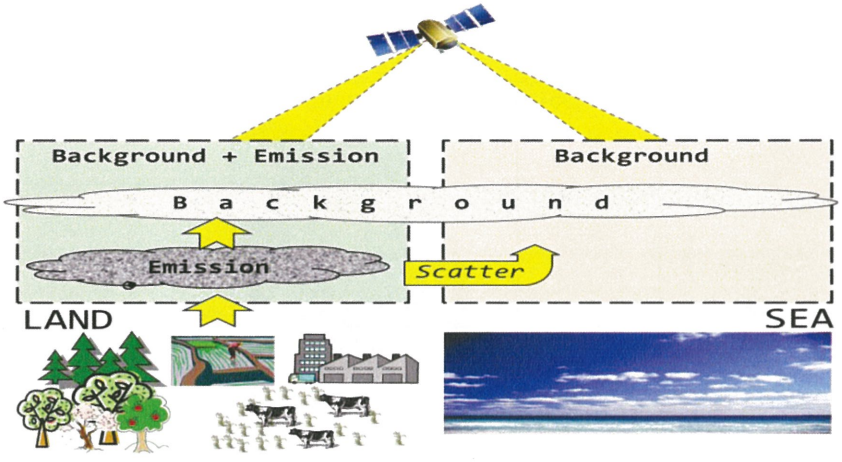

Figure 3. CH_4 emission concentration

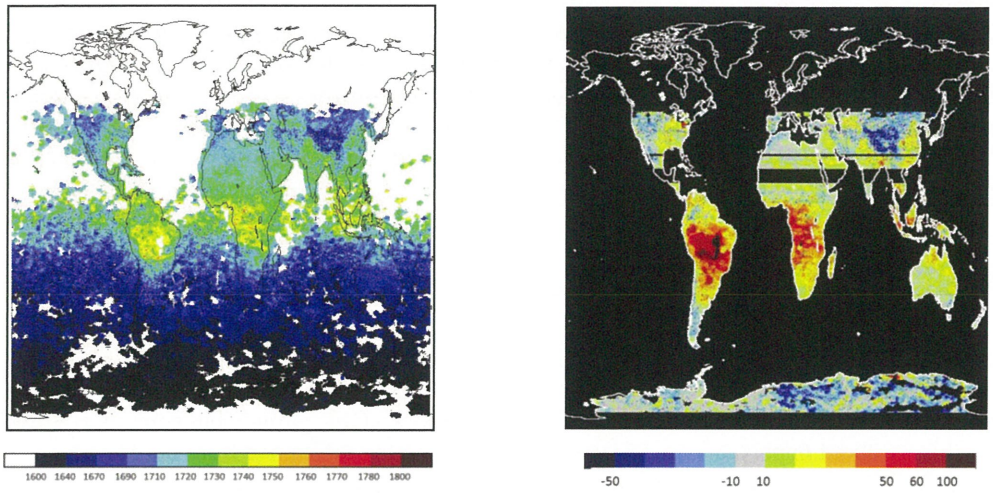

Figure 4. CH4 concentration (a) and CH_4 emission concentration (b) in January 2004

Figure 5 shows the emission concentration of CH4 by terrestrial latitude band for nine years. In mid-latitude of Northern Hemisphere areas there is a lot of CH4 emission concentration (figure 2), but figure 5 shows a higher emission concentration in the Southern Hemisphere. We understood that CH4 emission concentration increased in the Southern Hemisphere from 2007.

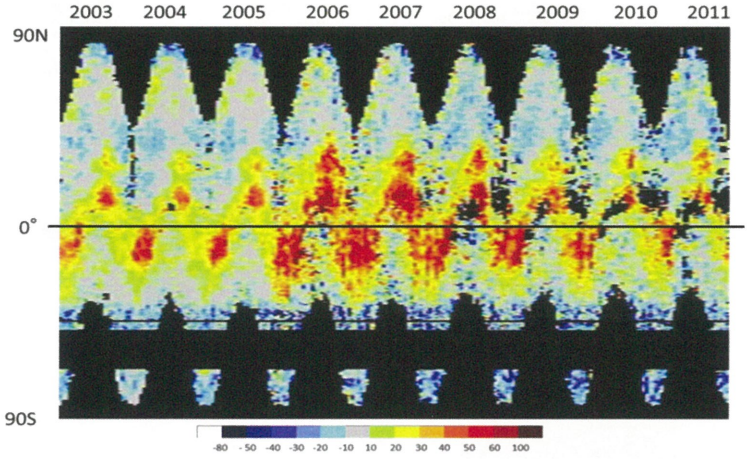

Figure 5. Ch_4 emission concentration time series from 2003 to 2011

3.4 Relation between CH4 emission concentration area and Lancover type

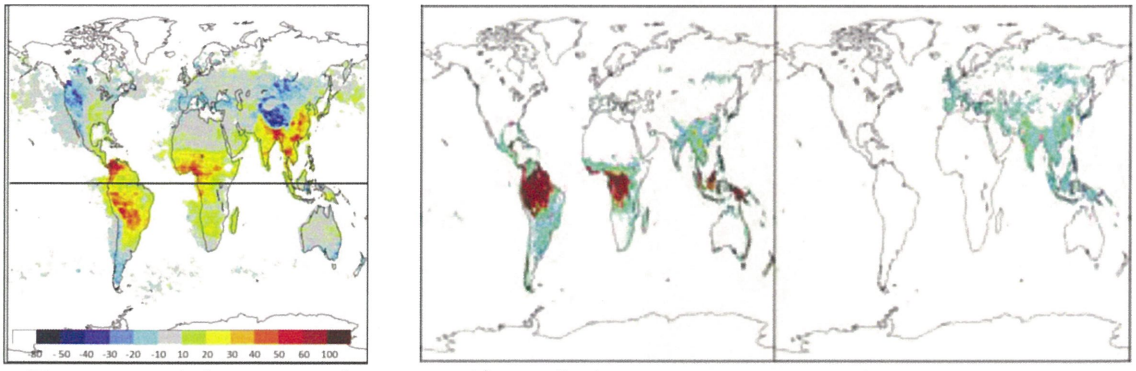

a) CH_4 average emission concentration b) Broadleaf Evergreen c) Paddy field

Figure 6. The comparison of the CH_4 emission concentration and Land Cover Type by MODIS

We understood that CH4 emission concentration increased in the Southern Hemisphere from 2007. Figure 6 shows CH4 average emission in 2009 and the vegetation map that was used to determine the geographical features of the CH4 emission concentration areas. From that we understood that there are a lot of broadleaf evergreen areas near the equator of the southern hemisphere, which emits 50-80ppb/year of methane (b). CH4 emission concentration areas of the northern hemisphere are consistent with the distribution of paddy fields which emits 80ppb/year (c). And because of the clouds in Northern hemisphere high latitude areas, we don't dispose of enough data to extract information about CH4 emission concentration on wetland areas.

3.5 The growth rate of CH4 concentration

We investigated the CH4 concentration's growth rate during 9 years of its data that reduces a seasonal change effect. As a result, in almost of land, there was a trend of 3- 5 ppb/year, but especially, in Brazil, China and Indonesia we noticed that it increased to more than 6ppb/year (Figure 7). According to the WMO-GAW, the average growth rate is 2.2ppb/year during 10 years until 2009. From 2003 to 2006 there was no CH4 growth, but announced that from 2006 it has been increasing by about 6ppb/year. This means that there is no big difference from our results.

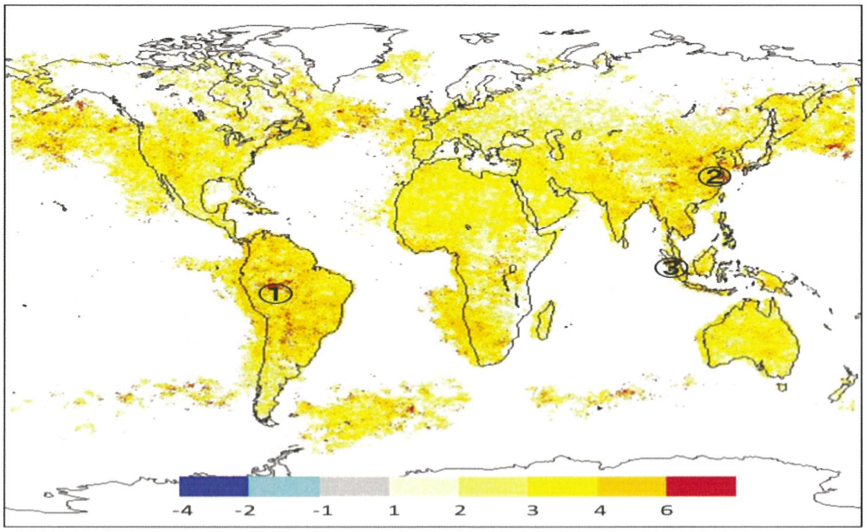

1. Brazil

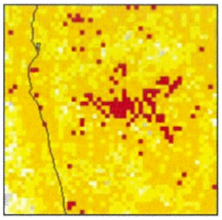

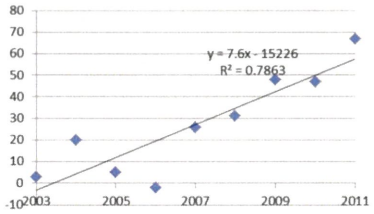

2. China

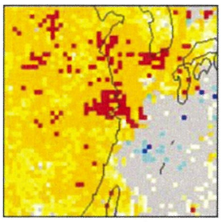

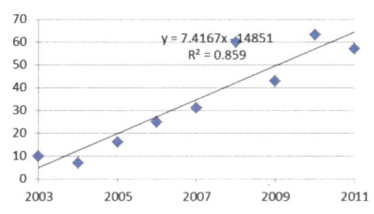

3. Indonesia

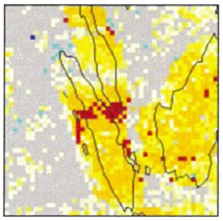

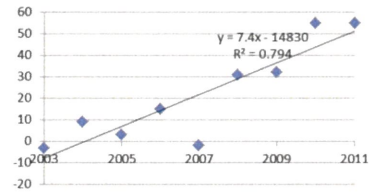

Figure 7. CH_4 growth rate during 9years

4. CONCLUSION

In this study, we examined separately the changes in methane concentration in land and sea areas using a time series SCIMACHY. Paddy field in Southeast Asia showed the highest among the CH4 concentration areas by 1780ppb. According to the MODIS NDVI comparison, the CH4 concentration increases by the paddy growth. And in the harvest time, the CH4 concentration raises its maximum. Methane concentration in the sea becomes higher gradually during 9 years. It reaches its maximum at the mid-latitude of the northern hemisphere, but becomes lower as it goes to the polar regions. Assuming that CH4 does not emit in the sea, the increase in CH4 concentration of sea areas is caused by the flowing CH4 emitted in land. The difference of land and sea methane concentration is the emission of land CH4 concentration. According to the land CH4 emission concentration, the high CH4 emission concentration areas are not only in paddy fields(80ppb/year) but also broadleaf evergreen areas in South America and Central Africa(50- 80ppb/year).

Finally, we removed the seasonal variation of CH_4 concentration from land during 9 years to investigate the CH_4 growth rate. As a result, in most of land areas, the growth rate of CH_4 concentration is 3-5ppb/year, but in some areas in Brazil, Indonesia and China is more than 6ppb/year. Next, it is necessary to search the cause of this growth rate increasing in these 3 areas.

ACKNOWLEDGEMENT

This research was supported by JSPS KAKENHI Grant-in-Aid for Scientific Research (C) and

References from Journals:

Burrows, J. P., H¨olzle, E., Goede, A. P. H., Visser, H., and Fricke, W.: SCIAMACHY – Scanning Imaging Absorption Spectrometer for Atmospheric Chartography, Acta Astronautica, 35(7), 445–451, 1995.

Carmo, J.B. DO, Keller, M., Dias, J.D., DE Camrgo, P.B. and Crill, P., 2006, A source of methane from upland forests in the Brazilian Amazon. Geophysical Research Letters, 33, L04809, doi:10.1029/2005GL025436.

Frankenberg, C., Platt, U., and Wagner, T.: Iterative maximum a posteriori (IMAP-)DOAS for retrieval of strongly absorbing trace gases: Model studies for CH4 and CO2 retrieval from nearinfrared spectra of SCIAMACHY onboard ENVISAT, Atmos. Chem. Phys., 5, 9–22, 2005.

Houweling, S., Rockmann, T., Aben, I., Keooler, F., Krol, M., Meirink, J. F., Glugokencky, E. J., and Frankenberg, C., Atmospheric constraints on global emissions of methane from plants, GEOPHYSICAL RESEARCH LETTERS, VOL. 33, L15821, doi:10.1029/2006GL026162, 2006

Keppler, F.,Hamilton, J.T.G., Brass.M. and Rockmann, T., 2006, Methane emissions from terrestrial plants under aerobic conditions. Nature, 439, pp. 187–191.

Kuze, A.; Suto, H.; Nakajima, M.; Hamazaki, T. Thermal and near infrared sensor for carbon observation Fourier-transform spectrometer on the Greenhouse Gases Observing Satellite for greenhouse gases monitoring. Appl. Opt. 2009, 48, 6716-6733.

Lelieveld, J., Crutzen, P.J. and Dentener, F.J., 1998, Changing concentration, lifetime and climate forcing of atmospheric methane. Tellus, 50B, pp. 128–150.

Miller, J.B., Gatti, L.V., D'Amelio, M.T.S., Crotwell, A.M., Dlugokencky, E.J., Bakwin, P., Artaxo, P. and Tans, P.P., 2007, Airborne measurements indicate large methane emissions from the eastern Amazon basin. Geophysical Research Letters, 34, L10809, doi:10.1029/2006GL029213.

Sanhueza, E. and Donoso, L. Methane emission from tropical savanna Trachypogon sp. grasses, Atmos. Chem. Phys., 6, 5315–5319, 2006

Sheshakumar K. Goroshi & R. P. Singh & S. Panigrahy & J. S. Parihar, Analysis of Seasonal Variability of Vegetation and Methane Concentration over India using SPOT-VEGETATION and ENVISAT-SCIAMACHY Data, J Indian Soc Remote Sens (September 2011) 39(3):315–321 DOI 10.1007/s12524-011-0097-z

Zhi, P.W, Xing, G.H. Geoff W.G. Yang, S. and Gullesge, J. Aerobic Methane Emission from Plants in the Inner Mongolia Steppe, Environ. Sci. Technol. 2008, 42, 62–68

References from Books:

IPCC, 2001, Climate Change 2001: The Scientific Basis. Contribution of Working Group I to the Third Assessment Report of the Intergovernmental Panel on Climate Change, J.T.Houghton, Y. Ding, D.J. Griggs, M. Noguer, P.J. van der Linden, X. Dai, K. Maskell and C.A. Johnson (Eds) (Cambridge, UK: Cambridge University Press).

IPCC, 2007, Climate Change 2007: The Physical Science Basis. Contribution of Working Group I to the Fourth Assessment Report of the Intergovernmental Panel on Climate Change,S. Solomon, D. Qin, M. Manning, Z. Chen, M. Marquis, K.B. Averyt, M. Tignor and H.L. Miller (Eds) (Cambridge, UK: Cambridge University Press).

Supporting Elephant Conservation in Sri Lanka through MODIS imagery

Kithsiri Perera*[a] and Ryutaro Tateishi[b]
[a]Faculty of Engineering and Surveying and Australian Centre for Sustainable Catchments, University of Southern Queensland, West Street, Toowoomba 4350 QLD Australia
[b]Centre for Environmental Remote Sensing (CEReS), Chiba University, 1-33 Yayoi-cho, Inage-ku, 263-8522, Japan.

Abstract: The latest government sponsored national elephant survey was conducted in Sri Lanka in 2011, revealing the number as 5,879. This is about 10% of the total elephant population of the sub-continent. The forest cover, the living environment of these elephants in Sri Lanka is about 19,500 sq km (2012 estimation). With a very high human population density of the island (332 people per sq km, 2010), the pressure for land to feed people and elephants is becoming critical, putting the lives of both sides at risk in rural areas. Resent reports indicated about 250 elephants are killed annually by farmers in man-elephant conflicts. Apart from various local level remedies for this issue, this study suggests the conservation of elephant population can be supported by remote sensing imagery based studies. Freely available MODIS sensor imagery can be considered as a successful candidate for the purpose. The advantage of spatial resolution of MODIS image (250m x 250m) to automatically filter out very small forest patches in the mapping process. Also, the daily receiving of imagery helps to monitor micro-level temporal green area changes, which helps to understand possible local level movements of elephants. However, the coarse image resolution is not capable to delineate finer boundaries between forest and settlements and farmlands. This study used MODIS 250m imagery to map Sri Lanka's forest cover (2012) and examined the possibility to identify sizeable forest patches that elephants can roam. Finer resolution images available in Google Earth were used to examine the accuracy and structure of forest- rural village-farm environment. In future study steps, actual elephant movement information will be gathered from local authorities and existing and potential bio-corridors will be tried to identify. Furthermore, monthly green area change maps and field investigations can be produced to gain a better understanding of elephant movements. Such information will provide a very influential source of data for wild elephant conservation of Sri Lanka.

Keywords: MODIS, Human-Elephant conflict, Sri Lanka, Conservation

1. Introduction

Sri Lanka, an island with 65,610 sq km land area has a rich biodiversity with a wide array of flora and fauna (27% of Sri Lanka's plants are endemic) (Mongabay.com, 2006). The central hills of the island are the source for over 100 rivers flowing to all directions in radial shape. The population of the country has dramatically increased from early last century recently passed 20 million. When the British Empire took the control of Sri Lanka in 1843, about 90% of the Island was covered by forest (Alagan, 2009).

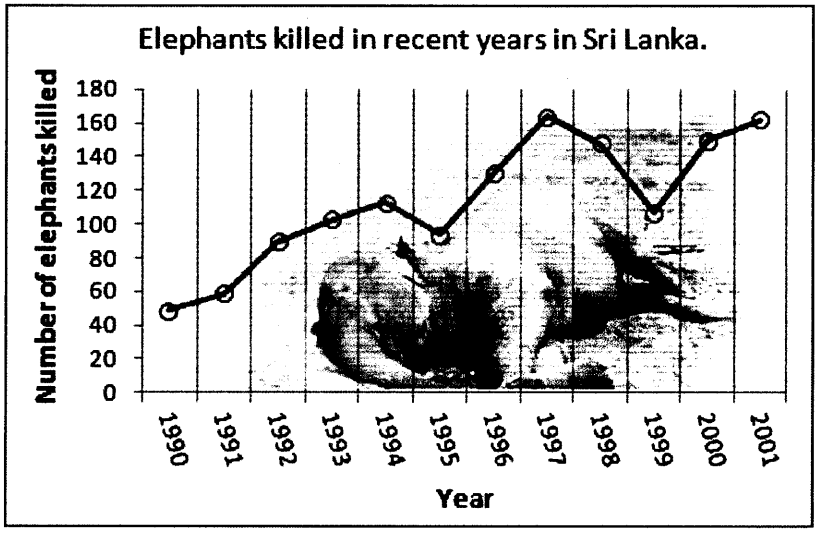

Figure 1. Elephant deaths have recorded a sharp increase in recent years. A bulk of the deaths is a result of HEC (source, IRI Technical Report 10-02, 2005).

This rich forest cover of the country was the breeding ground for Asian Elephants (*Elephas maximus*), that suffered by a rapid decrease in last 100 years. At the early stage, forest has been lost due to the spread of plantation agriculture introduced by the British administration. In the twentieth century deforestation was caused by expansion of informal settlements due to population increase, national development projects, government planned settlement programs, and land encroachments (Rathnayake et. al, 2002; Alagan, 2009; FRA, 2001). The rural area population has also increased sharply parallel to urban population, due to the natural increase and improvements in free healthcare system of the country (Dept of Statistics, Sri Lanka, 2001). This population pressure and rapid changes in land cover caused a massive pressure for space, igniting human-elephant conflicts and rapid increase of elephant deaths (Figure 1). Figure 2 shows the population increase with regard to selected rural districts where the bulk of forest cover is available. The increase of population has caused a tremendous pressure on land use rendering an adverse impact on wildlife.

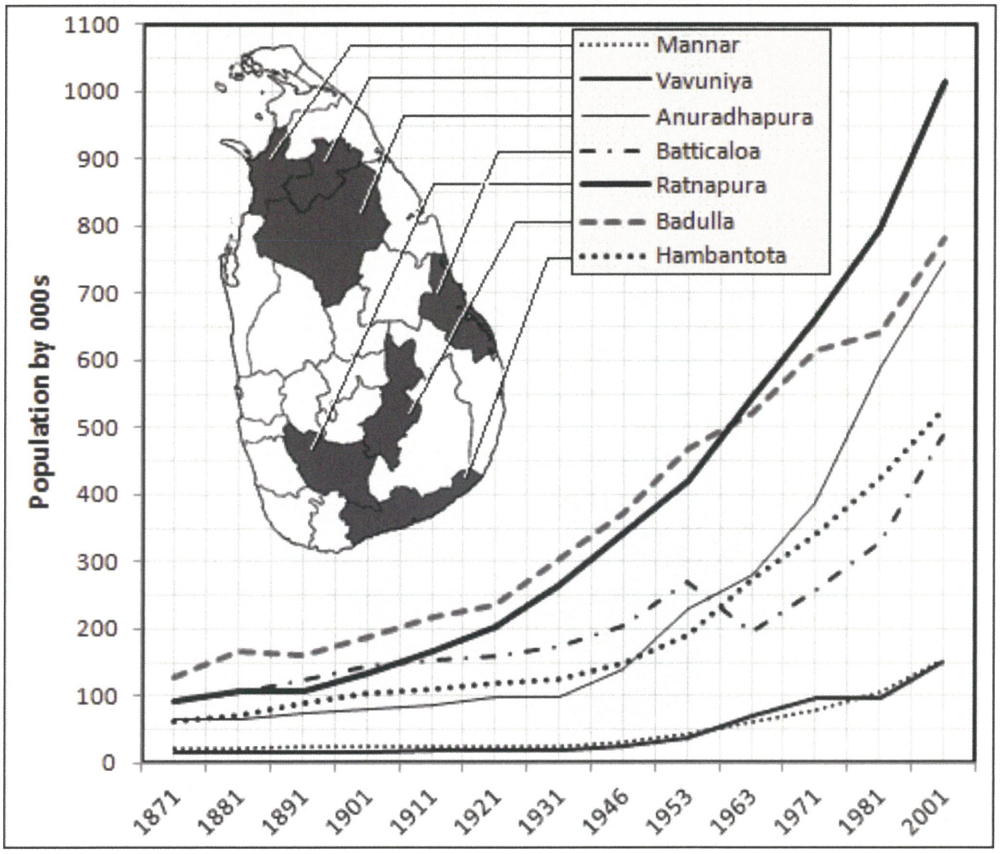

Figure 2. Increase of population in selected rural districts where a bigger potion of forest cover is available.

2. Forest Cover of Sri Lanka

Sri Lanka is characterized with a considerable topographic diversity from high mountain peaks to flat low lands (FRA, 2001). The central region of Sri Lanka rises over 2,500m (Mt Pidurutalagala 2,524 m) and a sizable area in the country exceeds 1500m above sea level, where a thick forest cover was available before large scale plantations begun in 18th century. A vast flatland along the coastal belt lies below 500 m from sea level, where most of the present day forests are located. River network flow in a radial pattern from central hills of Sri Lanka divides the island into 103 river basins (Wijesuriya 1989; Perera & Tateishi, 1991) (figure 3). Climatology of Sri Lanka behaves favorably to support the forest cover throughout the island. Sri Lanka receives rainfall from two major monsoons (south-west and north-east) and from inter-monsoon rains. The south-west monsoon (May to September) poured over 55% of the annual rainfall (GFDRR, 2011). However the present day forest cover is mainly located in low rainfall receiving flat lands of the country (figure 3)

where mean annual rainfall is less than 2500mm. The pattern of river network, mean annual rainfall, elevation, and the remaining forest in relatively dry regions of the country (figure 3) indicate clear evidences of historical flush greenery in all regions. Through the population increase and economic activities, forest cover reduced and restricted to three key regions of the country, i.e., Mahaweli River basin and northern plains, Central Hills, and Yala sanctuary in southeast. The elephant population of the country is also confined into these forest areas where boundaries are located just next to busy agricultural areas and villages.

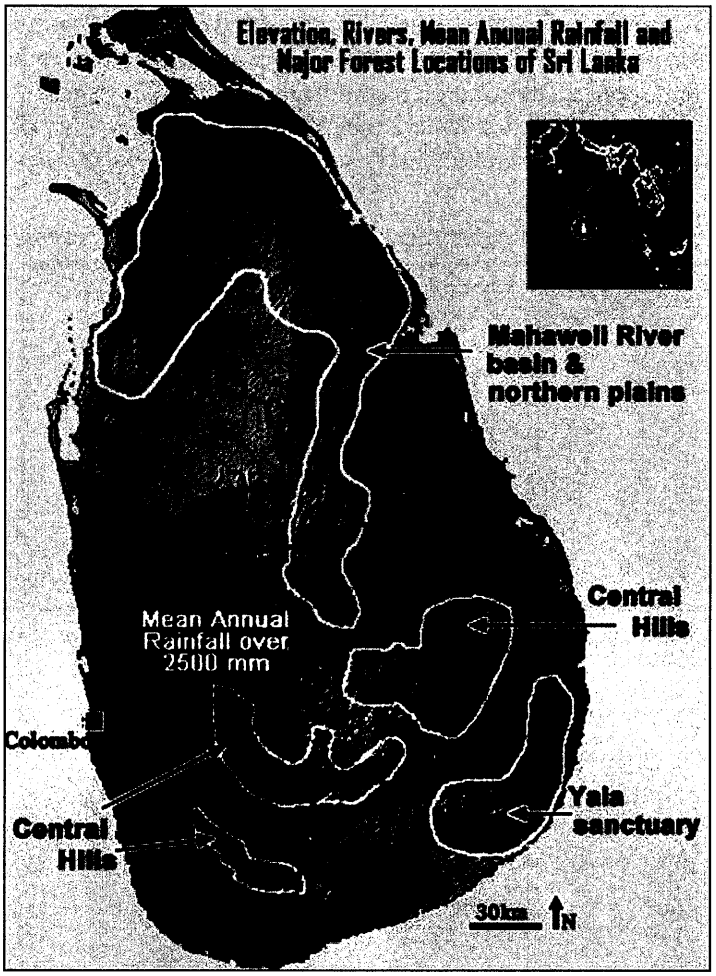

Figure 3. The central highlands, river network, mean annual rainfall and major forest locations (Mahaweli Basin, Central Hills, and Yala Sanctuary) of the island. Darker areas are high in rainfall.

The area under forest cover in recent years has given with different percentage values in different studies depending on the data source of the map, definition of the forest, and mapping methodology (Alagan, 2009; Perera & Tateishi, 1996; Rathnayake et al, 2002; Suzuki, 2007). Nearly all estimations have placed the percentage of forest cover of Sri Lanka as 25% - 30% of the total land area. However, according to the government estimations, forest cover within National parks and forest sanctuaries are gradually decreasing. Data shows this reduction from 2001 to 2009 as about 12,000 hectares (table 1). All natural and man-made changes in and around forest areas have a direct impact on elephant habitat. Therefore, assessing the limited forest cover is important for management of forests as well as to mitigate the risk of man-elephant conflict. This study investigated the applicability of MODIS 250m satellite images to establish some semi-real time information source to understand potential movements of elephants.

Table 1. Recent changes of National parks and Sanctuaries (000 of Hectares) (Source - Department of Wild Life Conservation).

Type	*2001*	*2002*	*2003*	*2004*	*2005*	*2006*	*2007*	*2008*	*2009*	*2009-2001*
National Parks	497	506	510	506	506	513	513	522	522	+ **23**

Sanctuaries	306	308	312	307	307	313	314	314	271	**- 35**

3. The Human-Elephant Conflict (HEC)

Compare to all Asian countries, Asian Elephant *(Elephas maximus)* has a very significant presence in Sri Lanka. In early 19th century, about half of Sri Lanka's estimated 12,000 elephants were forcibly eliminated by the British Colonial Government (IRI Technical Report 10-02, 2005). According to the present estimations, Sri Lanka has about 5,787 elephants which are about 10% of the total in Asian region. If the estimated elephant population divided by the land area, elephant density of India is 0.0008 and 0.006 in Thailand, while Sri Lanka's density is 0.088 (elephantcare.org, 2008). When this large number of elephants struggle for feeding grounds and food, especially in dry seasons, human-elephant conflict became a critical issue for villagers as well as elephants (figure 4).

Figure 4. Wild elephants are roaming next to farms and life of rural villagers in south-central Sri Lanka. Here, electric fence is dividing the two fractions of the conflict.

With a sharp increase of wild elephant deaths in recent years (figure 1), conflict has turned into a widely discussed topic in Sri Lanka. Various studies have investigated the conflict including elephant population and climatic and other socio-environmental aspects (IRI Technical Report 10-02, 2005; Perera, 2009; Fernando, et.al 2011; Fernando, 2001; Tilakaratne, & Santiapillai, 2002). According to these studies, number of reasons can be identified as causes to ignite of HEC.

- **Proximity of village-forest-elephant habitat**
- **Changes in long-term rainfall pattern**
- **Dryness in regions of elephant habitat**
- Increased human and other development activities closer to forests
- Behavioral changes of wild elephants

In this study, we have focused on first three facts due to the main objective of the study, "the application of satellite images".

3.1 The Closer proximity of village-forest-elephant habitat

The Close proximity of village-forest-elephant habitat can be counted as one of the prime reasons for the human-elephant conflict. Figure 5 presents a typical environment from south-central Sri Lanka to explain the close-proximity factor. The satellite image of Udawalawa, a notorious region of human-elephant conflicts shows, village, permanent, and semi-permanent farmlands are located next to secondary forest and also within 1.5km from the thick forest. Udawalawa is belongs to Southern region of elephant habitat, which has about 25% of the total elephant population (IRI Technical Report 10-02, 2005). The green area character of this

image is a typical example for most of the forest regions of Sri Lanka, which has the HEC. The proximity of forest-village character has directly affected by the fluctuations in climate conditions. Rainfall plays the direct role and increase of HEC has recorded in dry seasons (IRI Technical Report 10-02, 2005). With contrast to dryness, flood is also causing elephant deaths, especially in the eastern part of the country.

3.2 Changes in long-term rainfall pattern

The negative trend in long-term rainfall changes have discussed by Manawadu in his study, and found moderate to remarkable negative change in long-term rainfall pattern in number of districts in Sri Lanka (Manawadu & Nelun, 2008). Five dry-zone districts have identified under this negative trend, including Anuradhapura and Hambantoda where HEC is serious. This negative trend has identified by Basnayake and others too in their 2003 study on anticipated climatic change of Sri Lanka (Basnayeka at el, 2003).

3.3 Dryness in regions of elephant habitat

The relationship between dry weather and increase of elephant deaths has lengthily discussed in IRI Technical Report, which links dry season as a very important reason for increase of HEC and consequence potential high death rate of elephants. Figure adopted here from the IRI study shows this relationship (figure 6).

Figure 5. The closer proximity of village-forest-elephant habitat (image source: Google Images).

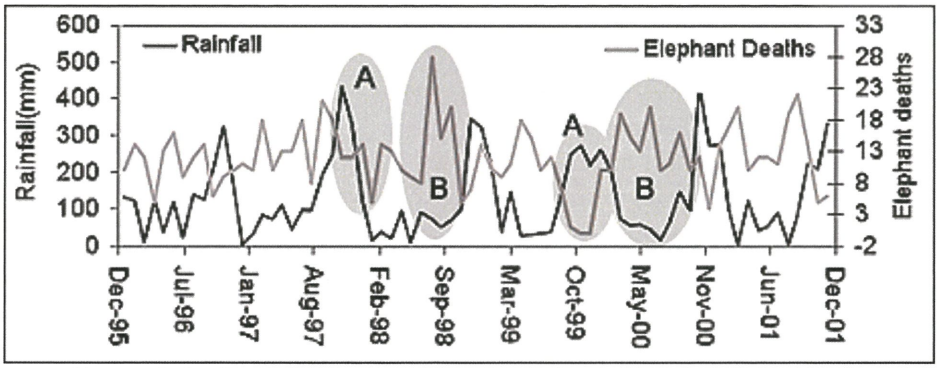

Figure 6. Death recordings of elephants have negative correlation with rainfall fluctuations. Letter A and B show two cases of high rain and low deaths and low rain and high death, respectively. (adopted from IRI Technical Report 10-02, 2005).

The first photo shows officials and villagers are struggling to transport a single-violent elephant from a conflict area to safer forest for the elephant. The second photo is showing a wild elephant is raoming next to the electric fence set by the government authorities to protect villagers and farms. With the pressure for foods in dry season, elephants started to approach villages and for finding crops. Once they used to attack villages

for food, the behavior may continue even without much drought due to the attractiveness of the crops (mainly rice, then other upland crops) (Fernando, et.al 2011). Apart from the crops, the farm wells and other water tanks in villages are converting to gathering spots for elephants when drought hits. The first photograph in figure 7 shows four elephants trapped in one of farm well. The other photos shows wildlife officials and villagers are trapping one violent elephant that killed number of villagers to transport to inner jungle.

Figure 7. Dealing with wild elephants; relocating and electric fencing.

4. Applicability of MODIS Satellite Imagery

In order to examine the applicability of satellite data in conservation of elephants, image characteristics of widely available satellite data types were checked. In recent years there are many well developed operational satellite systems are on the market to support decision-making and forest management at global and local scale (Perera et al., 1992; Eurisy report, 2011; Lehmann et al. 2012). Through the advancements of the technology, high resolution imaging sensors have been launched and the data acquired by these satellites are becoming useful for producing detailed land cover maps.

While these advantages are promising, it is extremely difficult to get cloud-free satellite imagery for Sri Lanka due to the near-perennial tropical cloud coverage over the mountains and long recurrent periods of the satellites. The high cost of finer resolution satellite images is another very significant hurdle. With regard to Sri Lanka, the country suffered 30 years long civil war which was just ended in 2009. Under this pretext data acquired by MODIS system can be suggested as a reasonable solution for regular monitoring. Table 2 presents some of the technical information of four major earth observation systems.

Table 2. Comparison of basic components of four prominent earth observation satellites.

Satellite	Recurrent	Swath	Spatial Resolution depending on the band
Landsat TM	16 days	185 km	15 to 60m
SPOT 4-5	2-3 days	60km	2.5 to 20m
ALOS	46 days	35km	2.5m
Terra/Aqua - MODIS	Daily	2330km	250 to 1000m

Source: NASA and SPOT web sites

After MODIS (MODerate- resolution Imaging Spectrometer)(MODIS, About MODIS, 2012) images became available, many scientists have successfully produced land cover maps with MODIS data or combined with other GIS (Geographic Information Sysyems) data to make use the advantages of MODIS system (Friedl et al., 2002; Hall et al., 2002: Price, 2003; Zhan et al., 2002). Geometrically corrected MODIS data products such as MODIS NDVI (MODIS, About MODIS, 2012) and true colour image data (NASA, MODIS Rapid Response Systems, 2011; Gumley et al., 2003) are available through NASA for the global community at no cost. Taking advantage of these pre-processed NASA's MODIS products and its inherited technical advantages (daily recurrent and broader swath), this study used MODIS NDVI products to conduct the forest cover assessment. The present study was partly based on a recent study published by the author on

experimenting on application of MODIS and Landsat MSS data to observe land cover changes in a selected sub-region of Sri Lanka (Perera & Tsuchiya, 2009).

5. Vegetation Monitoring and Elephant Conservation

5.1 NDVI analysis

The successful applicability of MODIS NDVI products for forest cover change detection in Sri Lanka was presented in two previous studies by the author (Perera & Tsuchiya, 2009, Perera at el, 2012). Based on those research findings, seasonal NDVI values of a selected location in south Sri Lanka (area including Udawalawe national park) was analyzed as a case study.

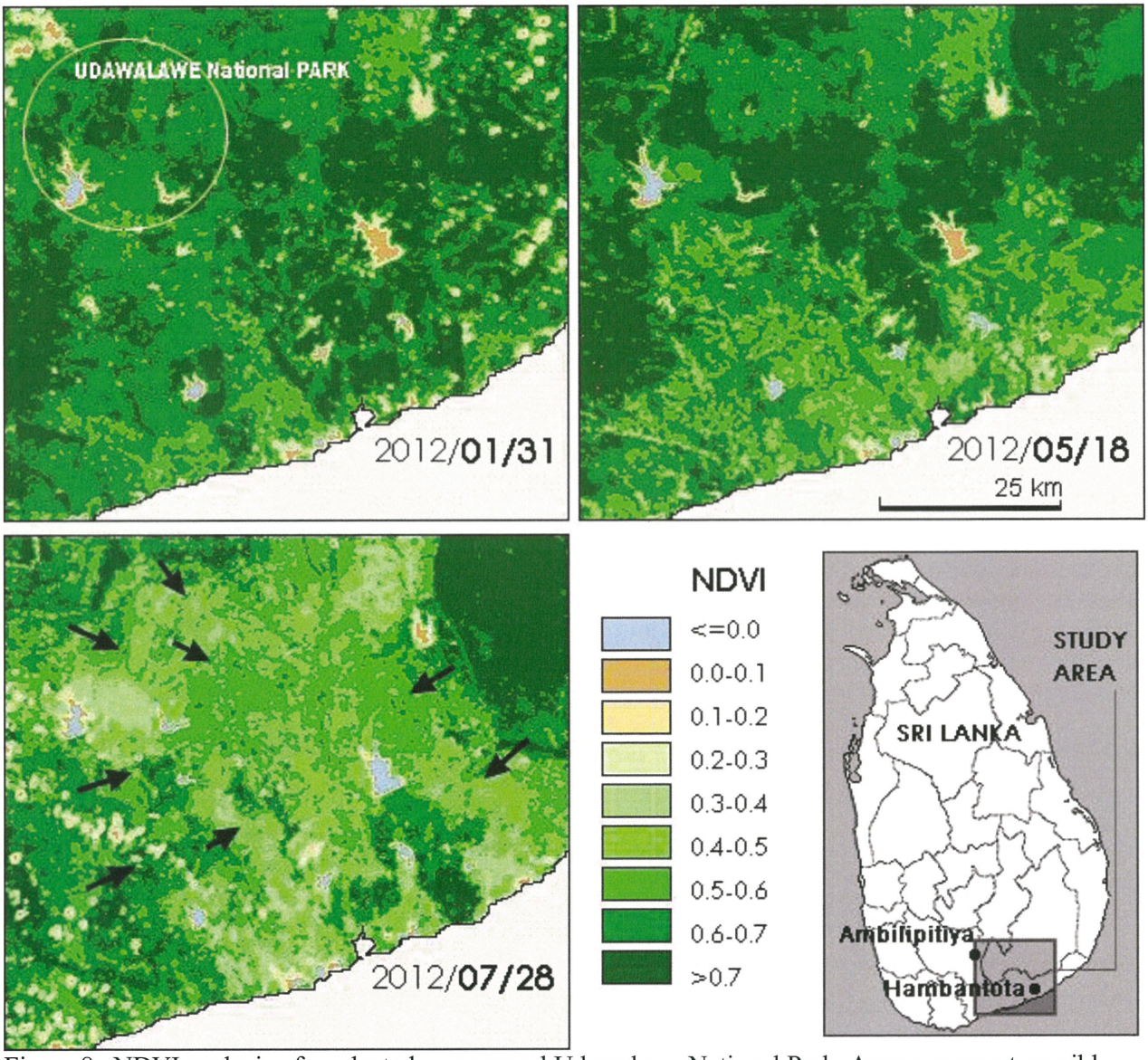

Figure 8. NDVI analysis of a selected area around Udawalawe National Park. Arrows suggest possible aggressive movement direction of elephants in dry season, when vegetation green drops.

The Udawalawa National Park is a popular spot for elephant viewing and located within the study area. Also, HECs are also severe, and only second to north-central Sri Lanka's incidents. NDVI image production process is bypassed in this study to avoid lengthily writing. Three NDVI data sets were produced and values were categorized into 9 classes (figure 8). Areas over 0.4 can be counted as high in green and are dominating in both January 31st and March 28th images. January rainfall seems low in the graph (figure 9), but January is

a wet month, due to heavy rainfall of November and December. The July 28th image is falling into dry season and central part of the region has turned into NDVI value less than 0.4. Image dates are also marked on the figure 9 graph which presents mean annual rainfall of 2 spots around the study area. The fluctuation of NDVI parallel to rainfall can be seen with regard to these three images.

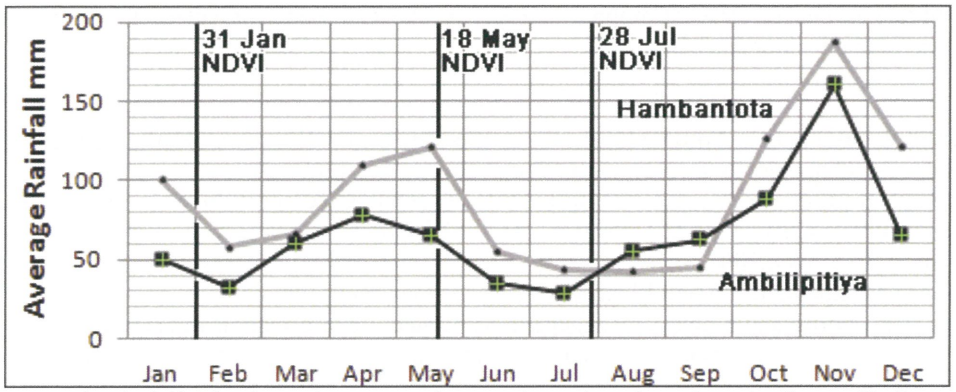

Figure 9. Mean annual rainfall of selected two weather stations (see locations in figure 8). Dates of three NDVI images presented in figure 8 are also displayed here to emphasize the relation between NDVI values and rainfall conditions.

5.2 Linking MODIS image interpretation with elephant conservation efforts

As presents in figure 8, three NDVI images have successfully showed the fluctuations in vegetation green parallel to rainfall amount. The use of NDVI for identifying potential hotspots in HEC has three assumptions;

a) Seasonal changes in greenery in Sri Lankan forests are negligible.
b) The impact of drought is successfully represented by dynamics in NDVI values.
c) Elephant attacks on villages and farmlands are increasing when the drought prolongs.

As mentioned in previous section, lower values of July NDVI image can be linked to less green vegetation in-between thick forest regions of east and west. This may caused elephants to search for alternative fresh leaves or other food, igniting conflicts with villagers. The case study result indicates the possibility of producing country-wide NDVI change detection and combined with GIS data base to establish elephant movement direction when the vegetation green fluctuates. Accordingly, NDVI provides a valuable tool through the utilization of freely available daily MODIS data to form an early warning system based on spatial information for HEC. When above mentioned three assumptions are met, the trends in NDVI values provides a clue to identify the locations of high risk or hotspots of HECs. This approach will help authorities to identify areas to be focused in elephant conservation as well as to protect villages from potential risk of elephant attack. Under future study prospect, the information and initial results found in this study can be used to buildup a logical data processing algorithm using semi-real-time NDVI products from MODIS 250m data to support HEC mitigation and elephant conservation efforts.

6. Conclusions

The applicability of MODIS satellite data to support elephant conservations plans was investigated in this study. Even though the spatial resolution of MODIS is low, its freely accessible daily data availability provided number of advantages in regular earth surface monitoring. This study mainly discussed the background information of forest cover of Sri Lanka, Human Elephant Conflict (HEC), and technical capability of identifying green area changes using MODIS data. Number of reasons for acceleration of HEC was identified and a link was established between those reasons and applicability of MODIS satellite images to extract some valuable information to support elephant conservation plans. MODIS images of a selected area in southern Sri Lanka were analyzed to produce NDVI images. Image processing aspects and justifications of suitability of NDVI for the study were discussed in details in some previous studies by the author and not lengthily repeated in this study. The NDVI images calculated from MODIS data acquired in wet and dry weather conditions showed the clear changes of green area which can be used to identify corridors of elephant movements. This approach will help authorities to identify areas to be focused in elephant conservation plans as well as to protect villages from potential risk of elephant attack. Under future

study prospects, island wide NDVI observation under wet, semi-wet and dry conditions and integration with a GIS database to buildup hotspots of HEC and establishment of potential elephant corridors can be listed.

Acknowledgement

Authors are thankful to CEReS, Chiba University, Japan, for partly funding this work under cooperative research grant. Also, special gratitude is due to Dr G. Campbel and Dr. A. Apan, Southern Queensland University, Australia, for institutional facilities and encouragements.

References

Alagan, R., 2009, Sri Lanka's Forest Cover: What We Know and What we Don't. Earthday 2009 publication, http://www.gvglobalvision.org/publications/Earth%20Day%202009.pdf

Basnayake, B.R.S.B.; Ratnasiri, J., and Vithanage, J. C., Rainfall & Temperature Scenarios for Sri Lanka under the anticipated Climate Change, AIACC Project - AS – 12 2003.

Dept of Statistics, Sri Lanka, 2001

Elephantcare.org/asiandem.htm, Asian Elephants - Elephas maximus , 2008

Eurisy report, 2011. Forest and biomass management using satellite information and services.

Fernando, P., Elephant conservation in Sri Lanka, The integration of Conservation Science and Policy, 649-651 2001

Fernando, P., Jayewardene, J., Prasad, T., Hendavitharana, and W., Pastorini, J., Current Status of Asian Elephants in Sri Lanka, Gajah 35 93-103 (2011).

FRA, 2001. Forestry Resources Assessment WP 17 under FAO, Forest Resources of Sri Lanka Country Report. http://www.fao.org/docrep/007/ad678e/ad678e00.htm (12 Dec 2011)

Friedl, M.A., McIver, D. K., Hodges, J.C.F. , Zhang, X.Y., et al. Global land cover mapping from MODIS: algorithms and early results. Remote Sensing of Environment, 83, 287-302, 2002.

GFDRR, 2011. Climate Change, Sri Lanka. Climate Risk and Adaptation Country Profile.

Hall, D.K., Riggs, G.A. , Salomonson, V.V., DiGirolamo, N.E., Bayr, K.J. 2002. MODIS snow cover products. Remote Sensing of Environment, 83, pp. 181-194 http://www.fao.org/docrep/007/ad678e/ad678e00.htm.\

IRI Technical Report 10-02, International Research Institute for Climate and Society, Climate Influences on Human - Elephant Conflict in Sri Lanka (2005).

Manawadu, L., Fernando, N., CLIMATE CHANGES IN SRI LANKA, 2008, archive.cmb.ac.lk.

MODIS, About MODIS, 2012. http://modis.gsfc.nasa.gov/about/specifications.php#1 (2012)

mongabay.com, 2006. Sri Lanka forest figures, http://rainforests.mongabay.com/20srilanka.htm

Perera, B. M. A. O. The Human-Elephant Conflict: A Review of Current Status and Mitigation Methods, Gajaha 30 41-52 (2009).

Perera, K., Tsuchiya, K., 2009. Experiment for mapping land cover and it's change in south eastern Sri Lanka utilizing 250 m resolution MODIS imageries, Advances in Space Research 43 pp. 1349–1355

Perera, L.K., Tateishi, R. 1991. Forest cover monitoring in southern hill country of Sri Lanka using Landsat MSS data. Proceedings of Annual Symposium of the Japan Society of Photogrammetry and Remote Sensing, pp. 115–120.

Perera, L.K., Tateishi, R. 1996. ACRS 1996, 1 KM Land Cover Data Base in Asia, GIS of management of forest in eastern Sri Lanka through a semi-knowledge based approach. http://www.a-rs.org/acrs/proceeding/ACRS1996/Papers/LCD96-2.htm

Perera, K., Herath, S., Armando, A., Tateishi, R., Application of MODIS Data to Assess the Latest Forest Cover Changes of Sri Lanka, Technical Commission VII/4, ISPRS Melbourne 2012.

Price, J. C. 2003. Comparing MODIS and ETM+ data for regional and global land classification. Remote Sensing of Environment, 86, pp. 491-499

Suzuki, K., 2007, Global Japanese data ranking.

Tilakaratne, N., & Santiapillai, C., The status of domesticated elephants at the Pinnawala Elephant Orphanage, Sri Lanka, Gajah 21 93-103 (2002)

Zhan, X., Sohlberg, R.A., Townshend, J.R.G., DiMiceli, C., Caroll, M.L., Eastman, J.C., Hansen, M. C., DeFries, R. S. 2002. Detection of land cover changes using MODIS 250m data. Remote Sensing of Environment, 83, pp. 336-350

Combination of L, C and X-band SAR data for continuous monitoring of land deformation in urban area by using DInSAR technique

Luhur BAYUAJI †, Ratih Fitria PUTRI ‡, and Josaphat Tetuko SRI SUMANTYO †

† Center for Environmental Remote Sensing, Chiba University
1-33, Yayoi-cho, Inage-ku, Chiba-shi 263-8522 Japan
Tel.+81-43 2903840 Fax +81-43 2903857

‡ Graduate School of Advanced Integration Science, Chiba University
1-33, Yayoi-cho, Inage-ku, Chiba-shi 263-8522 Japan

E-mail: † bayuaji@restaff.chiba-u.jp, jtetukoss@faculty.chiba-u.jp ‡ ratihfitriaputri@graduate.chiba-u.jp

Abstract Several major urban areas all over the world have been reported for suffering from land deformation. The land deformation causes buildings, properties, public facilities damages and ruin the city planning and maintenance. In this study, we apply DInSAR technique for monitoring land deformation in urban area using L, C and X-band Synthetic Aperture Radar (SAR) data by taking study site in Jakarta, Capital city of Indonesia. The purpose of using L, C and X-band data is to expose the possibility of combining different wavelength SAR data in the monitoring process, because of the discontinuation of single band SAR data availability. This study use ALOS PALSAR, ENVISAT ASAR and TERRASAR-X data during time period between 2007 and 2011.

Key words InSAR, DInSAR, land subsidence, Jakarta

1. Introduction

Differential synthetic aperture radar interferometry (DInSAR) is a technique useful for accurately detecting the ground displacement or land deformation in the antenna line-of-sight (slant-range) direction using synthetic aperture radar (SAR) data taken at two separate acquisition times [1, 2]. The DInSAR method is complementary to ground-based methods such as leveling and global positioning system (GPS) measurements, yielding information in a wide coverage area even when the area is inaccessible [3].

The area studied in the present work is Jakarta, the capital city of Indonesia. The interferograms, from L, C and X-Band, were used to investigate the land deformation on the study area during 2007 and 2011. Some data from L and C-Band was overlapped in time line. This study will highlight the specific characteristic of each frequency band in term of accuracy, error noise and decorrelation that occurs considering different sensor characteristic usage.

2. Study Area

Jakarta is located between 106°33'00"-107°00'00"E longitude and 5°48'30"-6°24'00"S latitude; in the northern part of West Java province. The area is relatively flat: in the northern and central part, topographical slopes range between 0°-2° and in the southern part; they are up to 5°. The altitude of the southernmost area is about 50 m above sea level and the other areas are lower (Figure 1A).

Figure 1B shows the geological information of the study area, which is mostly dominated by alluvial deposit. There are 13 natural and artificial (for supplying public water) rivers flowing through the city. It has humid tropical

climate with annual rainfall varying between 1500-2500 mm and is influenced by the monsoons. The nighttime population is around 8 million, which increases to 11 million during business hours since many people commute from satellite cities of Jakarta. The population (residence) density in the five districts was between 9,600-23,000 people km-2 as of the year 2000, while the most recent statistics in 2009 indicates that the values are between 12,000-19,000 people km-2 [4].

The occurrence of land subsidence in Jakarta was recognized by a Dutch surveyor as early as 1926 [5]. Scientific investigations started in 1978, and continuous investigation using leveling measurement was conducted during 1982-1999 [6]. The measurement using GPS was also undertaken during 1997-2005 [7]: however, its extension to a long-time and wide-area measurement would impose considerable effort and cost.

In this study we would like to investigate land subsidence by applying DInSAR technique on three different wavelength satellite data between 2007 and 2011.

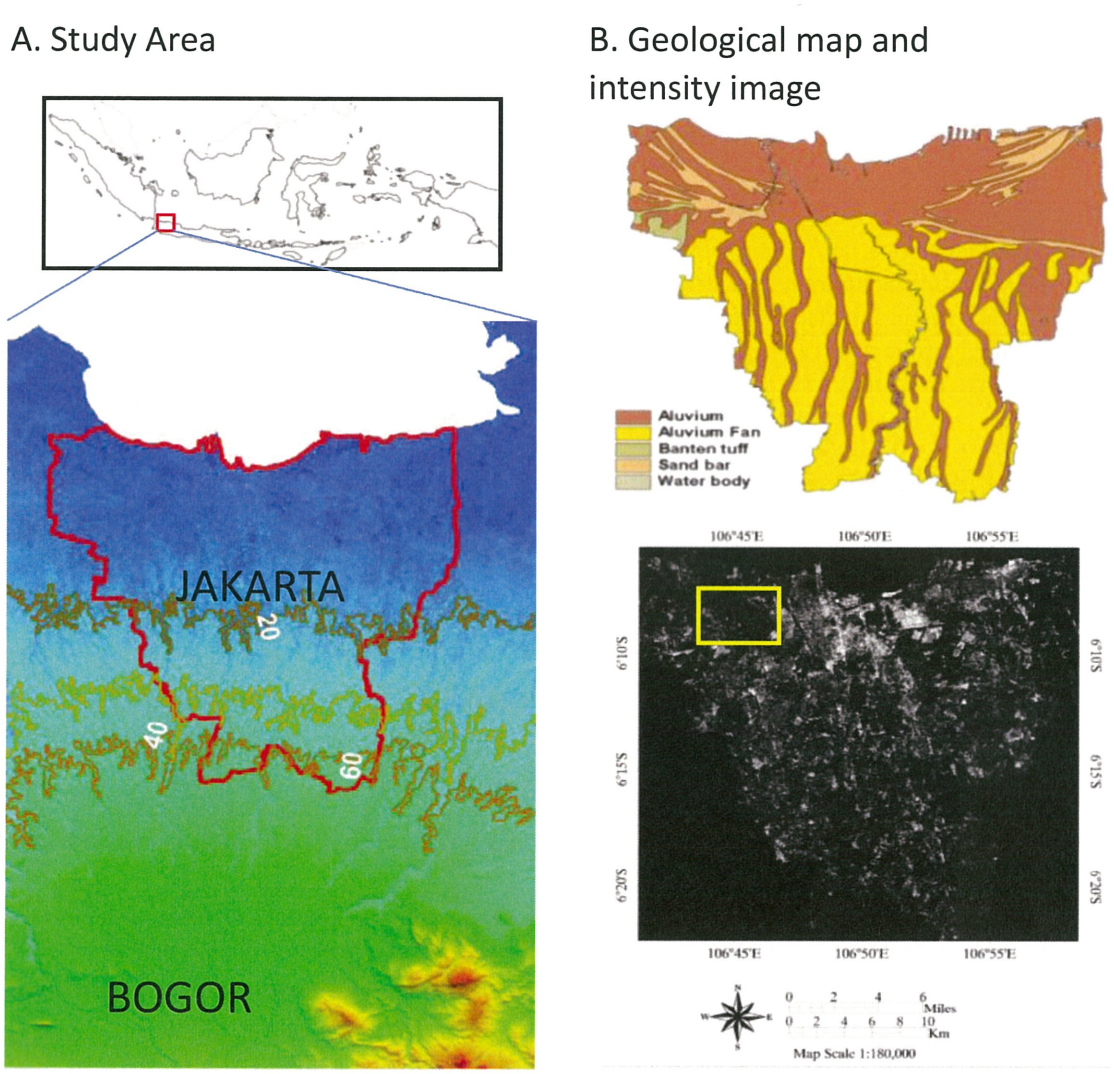

Figure 1. (A) Study area (B) Geological map and intensity image of study area

3. Type Size L, C and X-Band SAR data set

3.1. L-Band Interferometry: ALOS

The L-Band ALOS PALSAR instrument has been applied to many subsidence studies [8, 9]. In this study, ALOS has the longest wavelength (23.6 cm) and has the advantage of deeper penetration of vegetated areas that contribute to reduce the temporal decorrelation.

We analyzed the subsidence using four images between 2007 and 2009, that constructed into three pairs. All the images have been acquired from ascending orbits. The topographic-phase component was removed using 90-m DEM obtained from the Shuttle Radar Topography Mission (SRTM) version 4.1 that has been processed with hole-filled algorithm.

3.2. C-Band Interferometry: Envisat

The C-Band Envisat Advanced SAR (ASAR) sensor has been on operation mode since 2002 and has been used in may subsidence analysis [10, 11]. The wavelength is about 5.6 cm that give a temporal decorrelation over vegetation area compared to L-Band data of ALOS PALSAR. We exploited five images between 2007 and 2009 with ascending orbit. Four pairs have been constructed and have overlapped with ALOS PALSAR data interferometry.

3.3. X-Band Interferometry: TERRASAR-X

The ability of TERRASAR-X data to analyze subsidence in urban area has been proved in [12]. In this study, even though the TERRASAR-X has the shortest wavelength (3.1 cm), it has the highest spatial resolution compared to other data and become its advantage.

The TERRASAR-X data is the only data that has descending orbit in this study. We processed one pair of TERRASAR-X data between 2010 and 2011. This is the newest available data in this study

The timeline of obtained SAR for all satellites can be found in figure 2, while in Table 1, we report their pair, spatial baseline and temporal baseline.

Table 1. List of Inteferogram pair along with spatial and temporal baseline

Satellite	Pair Number	Pair Combination		Perpendicular Baseline (m)	Temporal Baseline (week)
		Master	Slave		
ALOS	1	20070131	20080203	220	52
	2	20080203	20081105	840	39
	3	20081105	20090205	308	13
	4	20090205	20100208	401	22
	5	20100208	20101227	750	46
ENVISAT	1	20070210	20080719	124	75
	2	20080719	20080927	154	10
	3	20080927	20081206	15	10
	4	20081206	20090912	188	40
TERRASAR-X	1	20100809	20110613	110	44

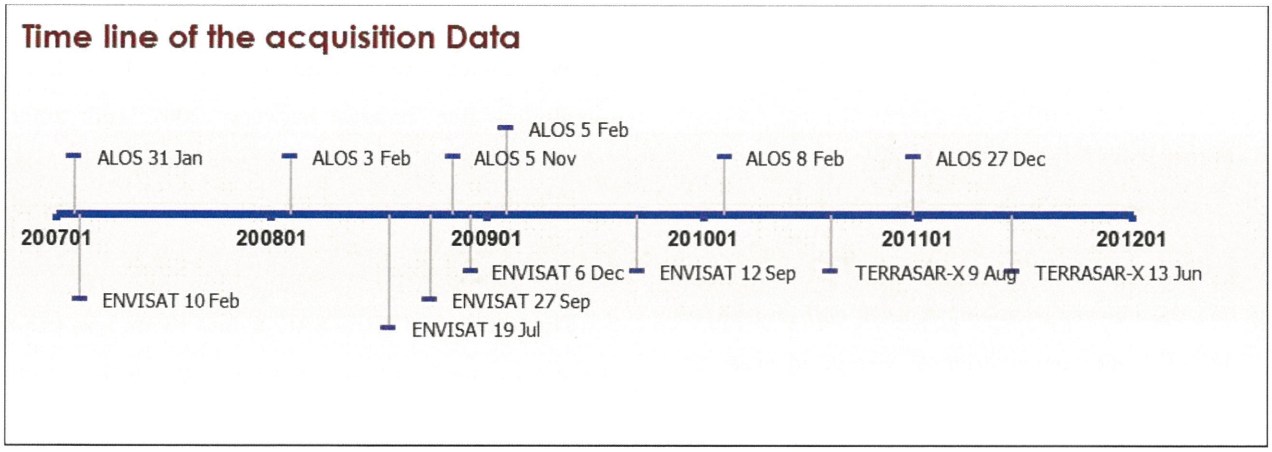

Figure 2. Time line of all processed SAR data

4. Result and Discussion

Figure 3 shows the result of DInSAR processing for all data pairs. At a glance, each pair result has less similarity compared to one another. Some pairs has good and clear fringes, some has a result with a lot of noise and many fringes that may come up from atmospheric disturbance. This result can be accepted since the data sets of this study are particularly inhomogeneous in terms of wavelength, spatial resolution, three different acquisition geometries and temporal decorrelation.

Giving a side of less similarity result, the subsidence on the northern part of Jakarta can be easily recognized. The subsidence occurrence in this area can be expected since this area formed on alluvial geological structure as seen in Figure 1B.

The discussion will go deeper to the subset area that fringes constantly appear in each pair of interferogram data. The subset area location can be seen on yellow rectangle area of Figure 1(B), hereafter called Cengkareng area.

The Cengkareng area is a newly developed residence area with more than 300 hundred households living over this area. The cause of subsidence was predicted as the result of ground water extraction, the building construction load and human activity over this area.

The land subsidence, detected by using DInSAR technique, gets worse as the temporal baseline increased. It gives the indication that the subsidence continuously occur in this area. The maximum subsidence for ALOS PALSAR pair was about 1.5 fringes and corresponds to 17.7 cm. As for ENVISAT ASAR pair, the maximum detected subsidence was about 8 fringes and correspond to 22.4 cm. Unfortunately, Cengkareng area cannot be fully covered on TERRASAR-X pair data as seen on figure 3 (J), but the available DInSAR result shows 6 fringes and correspond to 9 cm. The maximum estimated subsidence for each pairs shown in Table 2

The comparison between three pairs of DInSAR result, ALOS PALSAR pair on 20080203-20081105, ENVISAR ASAR pair on 20081206-20090912 and TERRASAR-X pair, gives similar subsidence estimation in term of same temporal baseline (about 40 weeks). The subsidence rate estimation for ALOS, ENVISAT and TERRASAR-X result was 14.2 cm, 14.6 cm and 10.6 cm, respectively, despite of incomplete DInSAR result of TERRASAR-X.

The estimation by using DInSAR result of three different satellite images showed the positive agreement in spite of similar temporal baseline. Table 2 also shows the estimated subsidence rate in cengkareng area and the result vary between 10.6-18.9 cm/year.

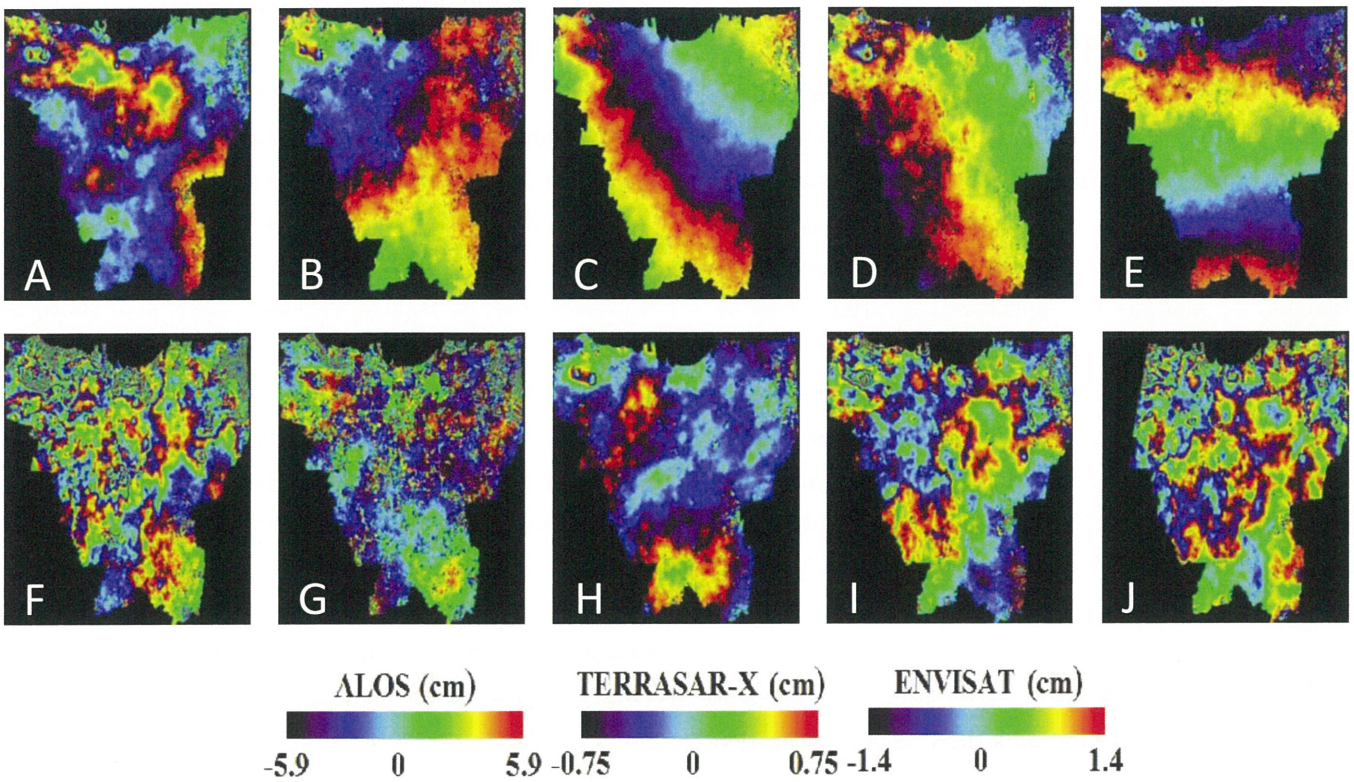

Figure 3. DInSAR result of all pairs mentioned in Table 1. (A-E) Interferogram of ALOS PALSAR data pairs (pair number 1-5 respectively). (F-I) Interferogram of ENVISAT-ASAR data pairs (pair number 6-8 respectively) and (J) Interferogram of TERRASAR-X data pair on 20100809-20110613.

Table 2. Maximum subsidence and subsidence rate estimation by using DInSAR technique

Satellite	Pair Number	Pair Combination		Cengkareng Subsidence estimation (cm)	Cengkareng Subsidence rate (cm/year)
		Master	Slave		
ALOS	1	20070131	20080203	17.7	17.7
	2	20080203	20081105	10.6	14.2
	3	20081105	20090205	4.7	18.9
	4	20090205	20100208	14.2	14.2
	5	20100208	20101227	9.4	10.7
ENVISAT	1	20070210	20080719	22.4	15.5
	2	20080719	20080927	2.8	14.6
	3	20080927	20081206	2.8	14.6
	4	20081206	20090912	11.2	14.6
TERRASAR-X	1	20100809	20110613	9.0	10.6

5. Conclusion and future work

In this study, the ability of three different wavelength satellite data has been investigated to detect monitor land subsidence over urban area. Despite of inhomogeneous data set, the result showed the agreement for Cengkareng area. From an applicative perspective, it gives the possibility to monitor the subsidence of urban area by using inhomogeneous data set.

In order to improve the analysis, the transformation to common geometry of one satellite and atmospheric effect reduction method will be conducted in the future. The GPS data will be used as validation to analyze the accuracy of DInSAR technique with the actual ground data survey.

6. Acknowledgement

The author would like to thank the PASCO Corporation for the support that has been given to this study in many ways not limited only for providing the TERRASAR-X data.

7. References

[1] S. Stramondo, C. Bignami, M. Chini, N. Pierdicca and A. Tertulliani, "Satellite radar and optical remote sensing for earthquake damage detection: Results from different case studies", International Journal of Remote Sensing, vol.27, no.20, pp. 4433 - 4447 2006.

[2] D. M. Tralli, R. G. Blom, V. Zlotnicki, A. Donnellan and D. L. Evans, "Satellite remote sensing of earthquake, volcano, flood, landslide and coastal inundation hazards", ISPRS Journal of Photogrammetry and Remote Sensing, vol.59, no.4, pp. 185-198 2005.

[3] D. Raucoules, C. Colesanti and C. Carnec, "Use of sar interferometry for detecting and assessing ground subsidence", Comptes Rendus Geosciences, vol.339, no.5, pp. 289-302 2007.

[4] Dinas Kependudukan dan Pencatatan Sipil Provinsi DKI Jakarta, "Kepadatan penduduk per wilayah kotamadya", Jakarta province government, Jakarta, 2009.

[5] H. Z. Abidin, H. Andreas, M. Gamal, R. Djaja, C. Subarya, K. Hirose, Y. Maruyama, D. Murdohardono and H. Rajiyowiryono, "Monitoring land subsidence of jakarta (indonesia) using leveling, gps survey and insar techniques", International Association of Geodesy Symposia, vol.128, pp. 561-566, 09 June 2005.

[6] R. Djaja, J. Rais, H. Z. Abidin and W. Kuntjoro, "The land subsidence of jakarta metropolitan area", in Proceedings of 3rd FIG Regional Conference for Asia and the Pacific, pp. 14, Jakarta, Indonesia, 2004.

[7] H. Z. Abidin, H. Andreas, R. Djaja, D. Darmawan and M. Gamal, "Land subsidence characteristics of jakarta between 1997 and 2005, as estimated using gps surveys", GPS Solutions, vol.12, no.1, pp. 23-32, 20 March 2007.

[8] T. Onuma and S. Ohkawa, "Detection of surface deformation related with co2 injection by dinsar at in salah, algeria", Energy Procedia, vol.1, no.1, pp. 2177-2184 2009.

[9] Y. Wang and T. R. Allen, "Estuarine shoreline change detection using japanese alos palsar hh and jers-1 l-hh sar data in the albemarle-pamlico sounds, north carolina, USA", International Journal of Remote Sensing, vol.29, no.15, pp. 4429 - 4442 2008.

[10] A. I. Calderhead, A. Martel, P. J. Alasset, A. Rivera and J. Garfias, "Land subsidence induced by groundwater pumping, monitored by d-insar and field data in the toluca valley, mexico", Canadian Journal of Remote Sensing, vol.36, no.1, pp. 9-23, 2010/02/01 2010.

[11] F. Jinghui, G. Xiaofang, G. Huadong, H. Zhengmin, G. Daqing and L. Shengwei, "Mapping subsidence in tianjin area using asar images based on ps technique", in Geoscience and Remote Sensing Symposium, 2007. IGARSS 2007. IEEE International, pp. 2975-2978, 2007.

Real Time Radar Imaging based on UAV Platforms

Helmut Essen[1],
MaXonic ® GmbH
Wachtberg, Germany
Helmut.essen@maxonic.biz

Sebastian Hantscher [2],
[2]Department Engineering and industrial Design,
Technical University Magdeburg-Stendal,
Magdeburg, Germany,
Sebastian.hantscher@hs-magdeburg.de

Abstract— **A miniaturised millimetre wave UAV-Synthetic Aperture-radar, MRUDIO, was designed, built and tested onboard a microlite aircraft and an unmanned helicopter. The design was conducted at Fraunhofer-FHR and followed the FM-CW principle, to get the highest possible average transmit power and thus the best range performance. A very flexible principle of operation, based upon multiplication of basic frequencies generated using a DDS oscillator, allows a very easy adaption of the band of operation between 35 GHz and 94 GHz. The experiments described here were conducted at an operating frequency of 94 GHz. An inertial system of high quality, based upon a fibre optic gyroscope maintained the necessary precision, to allow high resolution SAR imaging. The raw data are transmitted to the ground station using an analogue data link, where they are A/D converted, preprocessed and finally undergo a real-time SAR-focusing algorithm. Additionally to the quick-look processing the data are stored to be able to apply further high quality SAR processing. The mm-wave system can also be incorporated into a UAV-SAR developed at Iradar of Melaka (My) to serve applications with high sensitivity against small scale structures and changes at mmW-bands and better transmission through canopies of wood at lower frequencies.**

The paper describes the design principles and gives results from the flight tests.

I. INTRODUCTION

Airborne remote sensing is most important as well for civilian as for police and military applications. The inspection of disaster areas require very short reaction times to be able to take adequate means for recovering people or take other means of resilience. Another field of application is border control in land and maritime environment. To get the necessary detailed information, high-resolution multi parameter imaging of scenarios within limited areas is necessary. It is, however, of importance to be able to operate day and night and under adverse weather conditions including smoke and dust. As the Fukushima nuclear accident shows, also unmanned operation over dangerous terrain can be essential. Unmanned aircraft systems (UAS) are presently discussed for such applications, especially as carrier platforms, which allow, to carry miniaturized synthetic aperture radar systems. Millimeter-wave radars allow a very compact set-up, using MMIC technology and allows to use small antennas with adequate gain. Further, millimeter-wave radar is very sensitive to small scale variations of the scattering surfaces and give information on changes, which are not visible for classical radars at more traditional frequencies like X-band. Low frequencies, however, have other advantages, e.g. that they are able to look through canopies of wood. Consequently a combination of both SAR sensors either in parallel or dependent on the respective mission would be favorable.

A miniaturised millimetre wave radar, MRUDIO (**M**illimetre Wave **R**adar for **U**nmanned **d**irect **O**bservation), to be used as SAR onboard a small UAS was designed, and tests of such a system onboard of a small aircraft and an unmanned helicopter were conducted. The design follows the FM-CW principle, to get the highest possible average transmit power and thus the best range performance. An inertial system of high quality, based upon a fibre-optic gyroscope maintains the necessary precision to allow high resolution SAR imaging. The raw data are transmitted to the ground station where they are pre-processed and finally undergo a real-time SAR-focussing algorithm. Additionally to the quick-look processing, the data shall be stored to be able to apply further high quality SAR processing.

The system was developed to prototype status at Fraunhofer-FHR [1] and can be produced to serve a wide range of applications. At C-Band a well developed C-Band UAV SAR is available from Iradar (www.iradar.com.my) of Melaka (Malaysia). Both front-ends can be operated with the same signal acquisition and processing-hardware onboard of UAV or light aircraft. Further sensors like hyperspectral or IR as well as video sensors can be incorporated into an integrated system approach.

II. MILLIMETER-WAVE RADAR FOR UAV-SAR

Millimetre-wave radars in the 94-GHz region have been developed over several decades to serve military application mainly for seeker-heads and fuzed amunition. A well-known example is the SMART 155 mm artillery grenade [2]. Nowadays a range of other applications, mainly concerning security and safety, or automotive applications, can be served by mm-wave radars. This means, that a technology is available, which allows miniaturization of radars for applications, where only a limited payload is possible. Moreover also broadband performance can be realized with up-to-date solid-state technology, which is the key parameter for high-resolution radars. Additionally low noise performance allows to reduce transmit power without loosing signal to noise ratio and thus avoids expensive and heavy transmitter technology [3].

With this technological background, it has become possible to develop a really miniaturized millimetre-wave Synthetic Aperture Radar, able to be used onboard on-board a tactical UAV or a microlite aircraft and with real-time SAR processing.

W-band is the optimum choice for these applications, where small-scale features or chances have to be observed. Not only the required technology is available, but also the physical properties of scattering, result in a better contrast, lower speckle etc.. The scattering characteristics of targets and background in this frequency region are mainly governed by the increased relative roughness of all scattering surfaces. Sensitivity to small-scale features and changes is a prominent characteristic of this frequency band.

III. THE W-BAND RADAR FRONT-END

A miniaturized FM-CW radar operating at a centre frequency of 94 GHz has been developed, to demonstrate the capabilities of this frequency region in remote sensing. The radar uses a fixed pair of antennas, one for transmit and one for receive, without gimbal or electronic beam steering.

The main building blocks of MRUDIO-94 are:

- Airframe (Copter-UAV, Ultralight Aircraft) with remote control
- GPS-Telemetry and control computer on the ground
- On-board power supply
- Broad-band telemetry with receiver/ground-station
- Radar with fixed slotted array antennas
- Real time SAR signal processing ground station

The latest version of the MRUDIO radar uses a times-12 multiplier, allowing to build most of the RF electronics at a low frequency around 7 GHz. This gives the advantage to be able to use conventional hardware with microstrip technology, while only a few millimeter-wave components in the input- and output stages are required [4]. To maintain a low over-coupling between transmitter and receiver, a separate antenna in a special arrangement is used for each of both. The low over-coupling is mandatory to give a high dynamic range, which is necessary to detect indirect signatures. Fig. 2 shows a block diagram of the system. The photo of Fig. 3 illustrates the mechanical outline and Tab. 1 summarizes the performance data.

TABLE I. PERFORMANCE DATA OF MIRANDA RADAR

Transmit Frequency	94 GHz
Output Power	100 mW
Waveform	Linear Chirp
Chirp Length	120 ms
Bandwidth	1000 MHz
Resolution	15 cm
Polarization	H-V, H-H
Dynamic Range	60 dB

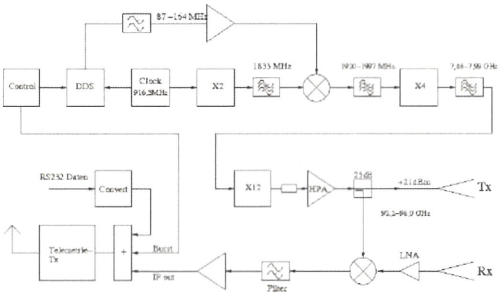

Figure 1. Block Diagram of Mrudio 94-GHz-Front-End

The high frequency components, namely the multiplier, the W-band mixer with integrated low-noise amplifier (LNA) and the high power amplifier (HPA), were developed by Fraunhofer Institute for Applied Solid State Physics (IAF). In this case, using the WR-10 frequency band, a multiplier by twelve is used. The low noise figure, high dynamic range and high gain of the devices result in a high dynamic range for the resulting SAR images.

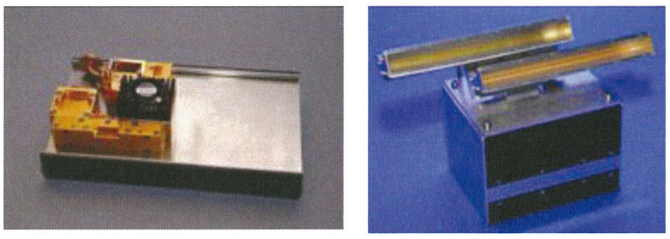

Figure 2. Photo of MRUDIO Front-End and complete Box

The waveform-generator module was especially designed for use with these components. The generator is developped using an AD 9910 DDS (Direct Digital Synthesizer). To avoid sidelobes in the spectrum, this chirp generator coveres the range from 87 MHz to 164 MHz, giving a maximum bandwidth of 77 MHz at this low frequency stage. The DDS is

synchronized by an ultra-stable master clock, which also drives other components of the front-end. This technique allows a fully coherent and stable operation, which is important to ensure the coherency within both a single chirp and series of chirps and thus enabling high resolution SAR processing over long range. The output of the waveform generation module synchronizes a signal between 7.68 GHz and 7.99 GHz. The desired output frequency is maintained by subsequent up-conversion and multiplication. By changing filter characteristics and the DDS operational mode, slightly different preprocessed frequencies can be achieved. By using different frequency multiplier modules, operational frequencies of 35 GHz, 60 GHz, 77 GHz, 94 GHz or 220 GHz and even beyond are feasible. For MRUDIO the 94-GHz band is realized.

IV. Different Carrier Concepts

In the course of the development of UAV-SAR at millimeter-wave bands different sensor carriers were tested.

A. SAR onboard Model Aircraft

As main emphasis was put to an as small as possible aircraft a model aircraft was used for the first tests. Today very reliable and sophisticated components are available for these applications, which make own developments unnecessary.

Preconditions are the ability to carry the projected maximum weight of 10 kg and a design which allows to fix the antennas at the side or below the hull. An easy access to all building blocks has to be guaranteed. In addition the motor has to be strong enough to handle the whole set-up safely with enough endurance for typical SAR missions. Although considerable progress has been made for electrical motors and power supplies for model aircrafts during recent times, the available power to handle an aircraft with the specifications discussed above would be much lower than for comparable combustion engines. It could be forseen that at least a tarmac runway would be necessary to achieve the necessary take off power. Due to these reasons a model aircraft of the type PAF [1] with a wing span of 3 m and a length of 2.5 m was chosen, equipped with a combustion engine DA 100 [2] with a nominal power of 7.3 kW. Fig. 3 shows a photo of the aircraft:

Figure 3. Photo of Model Aircraft with mmW-SAR

To be able to have quick-look capability also without SAR Processing, a slotted array antenna with narrow azimuthal beam was used. A typical quick-look image is shown in Fig. 4. It is obvious, that the image quality is quite bad and by far not related to the high bandwidth of the radar.

Detailed investigations were done to assess the most critical motion components [4]. It turned out, that it is not sufficient to employ a standard MEMS-based IMU and GPS.

Figure 4. Photo of Scene and Real-Aperture Image

B. SAR onboard Microlite Aircraft

UAVs with a weight above 20 kg are currently not allowed to fly over any terrain in Germany due to aviation legislation. Consequently system tests, which are necessary to evaluate the performance of the SAR, are difficult to perform whenever and wherever necessary. To become independent of these restrictive regulations, the SAR was put into a small, fully autonomuos pod, which can be operated with any aircraft. The Microlight aircraft, DELPHIN [4], was used to do extended flight test using this experimental aircraft. Fig. 5 shows a photo of the DELPHIN aircraft. As the data processing is done at the ground station, flights can only be conducted within the range of the data link, which is a few kilometers line of sight.

Figure 5. Photo of DELPHIN Aircraft

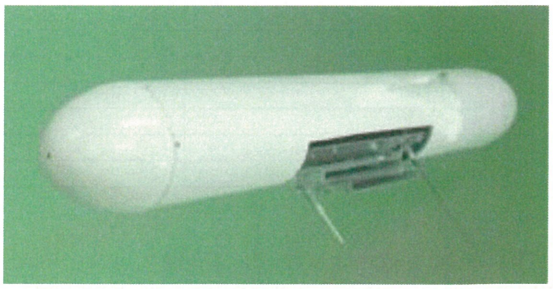

Figure 6. 94-GHz SAR in POD

The use of a bigger aircraft guarantees as well a much higher flight stability but also the use of a heavier IMU. This advantage has led to the choice of an Aerocontrol IMU based upon classical fibre gyroscope technology and thus very high precision. Fig. 7 shows a photo of the Aerocontrol IMU, which is integrated into the POD.

Figure 7. Aerocontral IMU

Many successfull flight tests have been conducted sing this carrier, which will be discussed in the following paragraph.

C. *SAR onboard Copter UAV*

Meanwhile the radar was built into the UMAT UAV owned by ESG [6], which is basically a NEO S300 helicopter built by SWISS-UAV [7]. Fig. 4 shows a photo of the NEO S-300 in flight and the built in SAR.

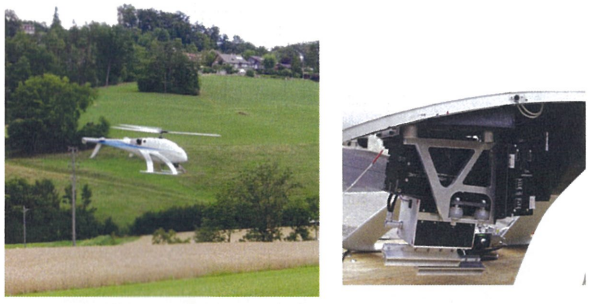

Figure 8. NEO-S300 and mmW-SAR

TABLE II. FLIGHT PARAMETERS

Flight Altitude above Ground	290 m
Velocity	31.8 m/s
Drift due to crosswind	10°
Chirp Lenght	1.08 ms
RF bandwidth	300 MHz
Antenna 3 dB Beamwidth (Az)	1.5°
Antenna 3 dB Beamwidth (EL)	12°

The radar together with the slightly bulky IMU fits very well into the copter and a campaign was conducted to test the performance of millimeter-wave SAR onboard such a carrier platform. It turned out, that rapid changes of the heading cannot be neglected for good image quality.

V. SAR IMAGING

The Measurement data from the airborne system, radar data and inertial data [8], are transferred to the ground station by a conventional analogue video data link. The data undergo a SAR imaging process in realtime. The SAR algorithm is following methods, which are well documented in the literature [9], however special refinement has to be done for the real-time processing.

The image shown in Fig. 9 is a screenshot of the real-time processing algorithm which displays the radar measurement online while performing the flight. The basic steps to process the images are:

- Read a block of data.
- Convert the IMU data.
- Synchronize the data using the burst signal which is included into the data every 2 ms.
- Calibration of the radar data with previous measurements of the radar on a calibrated corner reflector to balance non-linearities.
- Motion compensation using the IMU data
- Range transformation.
- Focusing.
- Doppler transformation.
- Projection of the processed strips for online display.

This online processor makes some simplifications which are not crucial at small wavelengths as used at mm-waves. For example the processed stripes are small and are then stitched together using a mosaicking method. Using a very accurate IMU this turns out to be no problem. Furthermore, for online processing Doppler rotation is not used at the reduced resolution. For projection of each stripe just the position on the ground for the first and last resolutional cell is calculated exactly. All pixels in between are linearly interpolated. In a final step, the image is projected on a flat earth, while the initial altitude was already defined at the start of the measurement.

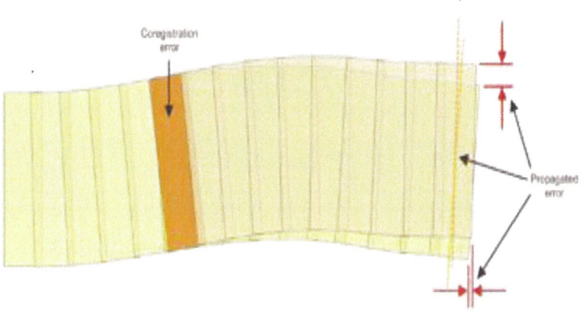

Figure 9. Mosaicking of processed Stripe

VI. SAR IMAGING

The following images show example for SAR performance at 94 GHz for different types of terrain. Fig. 10 shows an example of inhabited terrain with streets and buildings. Fig. 11 shows an industrial terrain with more tighly positioned buildings, while Fig. 12 shows an example of rural terrain with meadows and a plantation of apple trees.

Figure 10. Real-Time SAR Image of inhabited Area

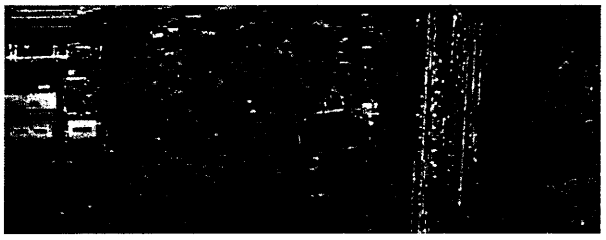

Figure 11. SAR Image of industrial Terrain

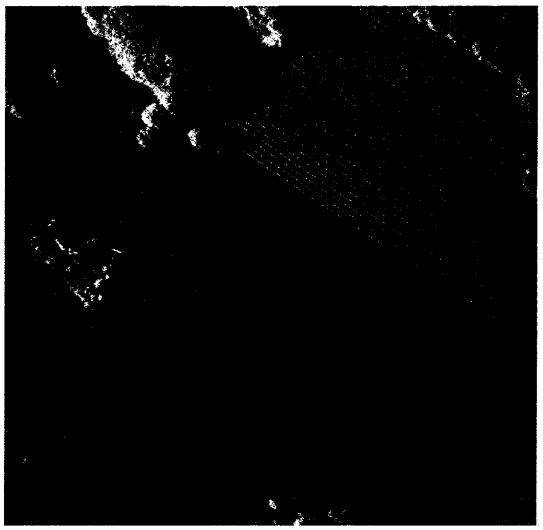

Figure 12. SAR Image of rural Terrain

All images flown with the small fixed-wing aircraft were quite good and related to the theoretical resolution given by the radar bandwidth. For flights with the NEO-S300 copter this could not be maintained for all flights. Incases, where the heading made a rapid change due to the flight dynamics of the rotary wing carrier, sectors of not sufficient data appeared, resulting in a smearing out of the images. Fig. 13 shows a respective example.

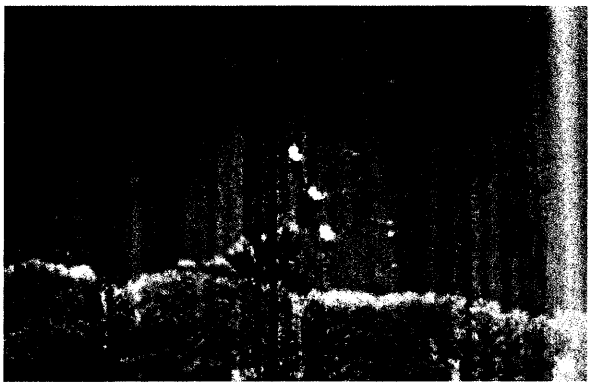

Figure 13. Real-Time SAR Image for UAV Flight with rapid Yaw Movement

VII. CONCLUSION

It could be demonstrated, that a miniaturized Synthetic Aperture Radar at 94 GHz, is well suited to be operated on board of a small UAV, like the NEO S300 copter or for ease of operation on board of any small air vehicle, like a microlite aircraft. The capability to do real time SAR processing with high resolution at a ground station at a remote location could also be demonstrated. In comparison with other radar sensors at lower frequencies like X-band, millimetre-waves have numerous advantages which make them especially suitable for investigation of small scale features, like sensing of crops also under adverse environmental conditions. They do not suffer from any dust, smoke or bad weather like EO and IR sensors do. They are also ideally suited to give the necessary guidance to ground based systems.

REFERENCES

[1] http://www.giws.de/en/smart/design.html

[2] www.fhr.fraunhofer.de

[3] H. Essen, A. Wahlen, R. Sommer, G. Konrad, M. Schlechtweg, A. Tessmann, "A very high Bandwidth Millimetre Wave Radar", Electronic Letters, Oct. 2005, Vol. 41, No 23, pp 1247, 1248

[4] S. Stanko, W. Johannes, H. Essen, R. Sommer, A. Wahlen, J. Wilcke „SAR with MIRANDA – Millimeterwave Radar using Analogue und New Digital Approach", EuRad, Manchester, 2011

[5] http://www.vlflugzeuge.de

[6] http://www.esg.de/branchen/luftfahrzeuge/beratung/

[7] www.swiss-uav.com/pdf/press_release_neo_hoehenflug_de_2010.pdf

[8] www.emt-penzberg.de/index.php?32&L=1

[9] IGI Systems, Kreuztal, Germany (igi-systems.de)

[10] H. Essen, M. Hägelen, W. Johannes, R. Sommer, A. Wahlen, M. Schlechtweg, A. Tessmann, „High Resolution Millimetre Wave Measurement Radars for Ground Based SAR and ISAR Imaging". IEEE Radar Conference, Rome, 2008

Quantitative bias estimates for tropospheric NO_2 columns retrieved from SCIAMACHY, OMI, and GOME-2 using a common standard for East Asia

Hitoshi Irie[1], Folkert Boersma[2], Yugo Kanaya[3], Hisahiro Takashima[4], Xiaole Pan[5], and Zifa Wang[6]

[1]Associate Professor, Center for Environmental Remote Sensing, Chiba University
1-33 Yayoicho, Inage-ku, Chiba 263-8522, Japan; Tel: +81-43-2903876
E-mail: hitoshi.irie@chiba-u.jp

[2]Research scientist, Royal Netherlands Meteorological Institute, Climate Observations Department
P.O. Box 201, 3730 AE De Bilt, The Netherlands; Tel: +31-30-2206618
E-mail: boersma@knmi.nl

[3]Team Leader, Research Institute for Global Change,
Japan Agency for Marine-Earth Science and Technology
3173-25 Showa-machi, Kanazawa-ku, Yokohama, Kanagawa 236-0001, Japan; Tel: +81-45-7785720
E-mail: yugo@jamstec.go.jp

[4]Assistant Professor, Department of Earth System Science, Faculty of Science, Fukuoka University
8-19-1 Nanakuma, Jounan-ku, Fukuoka 814-0180, Japan; Tel: +81-92-8716631
E-mail: hisahiro@fukuoka-u.ac.jp

[5]Postdoctral Researcher, Research Institute for Global Change
Japan Agency for Marine-Earth Science and Technology
3173-25 Showa-machi, Kanazawa-ku, Yokohama, Kanagawa 236-0001, Japan; Tel: +81-45-7785722
E-mail: xlpanelf@jamstec.go.jp

[6]Professor, LAPC, Institute of Atmospheric Physics, Chinese Academy of Sciences
Beijing 100029, China; Tel: +86-10-82084278
E-mail: zifawang@mail.iap.ac.cn

KEY WORDS: Satellite, Validation, NO_2, MAX-DOAS, Remote sensing

ABSTRACT: For the intercomparison of tropospheric nitrogen dioxide (NO_2) vertical column density (VCD) data from three different satellite sensors (SCIAMACHY, OMI, and GOME-2), we use a common standard to quantitatively evaluate the biases for the respective data sets. As the standard, a regression analysis using a single set of collocated ground-based Multi-Axis Differential Optical Absorption Spectroscopy (MAX-DOAS) observations at several sites in Japan and China in 2006-2011 is adopted. Examination of various spatial coincidence criteria indicates that the slope of the regression line can be influenced by the spatial distribution of NO_2 over the area considered. While the slope varies systematically with the distance between the MAX-DOAS and satellite observation points around Tokyo in Japan, such a systematic dependence is not clearly seen and correlation coefficients are generally higher in comparisons at sites in China. On the basis of these results, we focus mainly on comparisons over China and estimate the biases in SCIAMACHY, OMI, and GOME-2 data (TM4NO2A and DOMINO version 2 products) against the MAX-DOAS observations to be -5±14%, -10±14%, and +1±14%, respectively, which are all small and insignificant. We suggest that these small biases now allow analyses combining these satellite data for air quality studies that are more systematic and quantitative than previously possible.

1. Introduction

Three satellite sensors, SCIAMACHY (SCanning Imaging Absorption SpectroMeter for Atmospheric CHartographY) (Bovensmann et al., 1999), OMI (Ozone Monitoring Instrument) (Levelt et al., 2006), and GOME-2 (Global Ozone Monitoring Experiment-2) (Callies et al., 2000), were all in orbit together until April 2012, observing tropospheric nitrogen dioxide (NO_2) pollution on global scale and providing long-term data records (since 2002) of vertical column densities (VCDs). Observations by these satellite sensors were performed at different local times, and the diurnal variation pattern seen in the NO_2 data has been reported for various locations over the world (Boersma et al., 2008). However, the diurnal cycle observed by SCIAMACHY and OMI has been validated only over the Middle East, a region with highly active photochemistry (Boersma et al., 2009). The observations of the diurnal variation are expected to provide additional constraints to improve models, beyond a single VCD data set at a specific local time (e.g., Lin et al., 2010). The combined use of SCIAMACHY, OMI, and

GOME-2 data is desirable to improve our understanding of short-term variations in chemistry, emissions and transport of pollution. There have been, however, few studies attempting to quantify the biases in SCIAMACHY, OMI, and GOME-2 data in a consistent manner based on comparisons with independent observations. In East Asia, validation comparisons for specific satellite data sets are very limited, except for the NASA OMI standard product (Irie et al., 2009). Here we present a consistent data set based on Multi-Axis Differential Optical Absorption Spectroscopy (MAX-DOAS) observations performed at several sites in Japan and China in 2006-2011. Because MAX-DOAS provides continuous measurements during daytime, its data are used as a common reference to validate all three satellite data sets. The present work focuses on estimating representative bias between satellite and MAX-DOAS NO_2 VCD data over East Asia for each satellite data set.

2. Satellite observations

The present study targets tropospheric NO_2 VCD data from SCIAMACHY, OMI, and GOME-2, all of which are equipped with a UV/visible sensor measuring sunlight back-scattered from the Earth's atmosphere and reflected by the surface as well as the direct solar irradiance spectrum. SCIAMACHY was launched onboard the ENVISAT satellite in March 2002. It passes over the equator at about 10:00 LT and achieves global coverage observations in six days, with a spatial resolution of 60×30 km^2. OMI was launched onboard the Aura satellite in July 2004. The equator crossing time is about 13:40-13:50 LT. Daily global measurements are achieved by a wide field of view (FOV) of 114°, in which 60 discrete viewing angles (at a nominal nadir spatial resolution of 13×24 km^2) are distributed perpendicular to the flight direction. The GOME-2 instrument, launched aboard a MetOp satellite in June 2006, has a ground-pixel size of 80×40 km^2 (240×40 km^2 for the back scan) over most of the globe. With its wide swath, near-global coverage (with an equator crossing time around 9:30 LT) is achieved every day. While observation specifications are thus somewhat different between the three sensors, tropospheric NO_2 VCD data retrieved with the same basic algorithm (DOMINO products for OMI and TM4NO2A products for SCIAMACHY and GOME-2) (Boersma et al., 2004, 2007, 2011) are compared in detail with MAX-DOAS data below. The error in the satellite tropospheric NO_2 VCD data includes uncertainties in the slant column, the stratospheric column, and the tropospheric air mass factor (AMF) (Boersma et al., 2004), and can be expressed as ~1×10^{15} molecules cm^{-2} + 30% for polluted situations. Comparisons are made for the version 2 retrievals under cloud-free conditions, i.e. cloud fraction (CF) less than 20%.

3. MAX-DOAS observations

Here we briefly describe ground-based MAX-DOAS measurements - scattered sunlight observations in the UV/visible at several elevation angles between the horizon and zenith (e.g., Hönninger and Platt, 2002; Hönninger et al., 2004) - performed at three sites in Japan and three sites in China (Fig. 1). As can be seen in Fig. 1, the MAX-DOAS measurements were conducted at various levels of NO_2 pollution, covering urban (Yokosuka), suburban (Tsukuba) around Tokyo, and remote areas (Hedo) in Japan and the northernmost (Mangshan), middle (Tai'an), and southernmost (Rudong) parts of the highly polluted area in China. This set of observations extends the data set used by Irie et al. (2009) for the validation of the NASA OMI NO_2 standard product. The present study additionally uses data for 2009-2011 and data from the Mangshan and Rudong sites. The observations at Tai'an, Mangshan, and Rudong were made as part of intensive observation campaigns for a limited time period of about 1 month for each site. The instrumentation and retrieval algorithm used for all the sites have been described in detail elsewhere (e.g., Irie et al., 2008, 2009, 2011; Takashima et al., 2011a, 2011b). The retrieval utilizes absorption features by NO_2 and the oxygen dimer (O_4) at 460-490 nm. The NO_2 absorption cross section data of Vandaele et al. (1998) at 294 K were used. The quality of our DOAS analysis is supported by formal semi-blind intercomparison results indicating good agreement with other MAX-DOAS observations to within ~10% of other instruments for both NO_2 and O_4 differential slant column densities (ΔSCD) and for both the UV and visible regions (Roscoe et al., 2010). The O_4 ΔSCD values derived from the DOAS analysis are converted using our aerosol retrieval algorithm (e.g., Irie et al., 2008) to aerosol optical depth and the vertical profile of the aerosol extinction coefficient. At the same time, the so-called box AMF is uniquely determined, as it is a function of the aerosol profile. Using this AMF information and a nonlinear iterative inversion method, the NO_2 ΔSCD values are converted to the tropospheric VCD and the vertical profile of NO_2. Error analysis for the retrieved NO_2 VCDs has been done based on the method described by Irie et al.

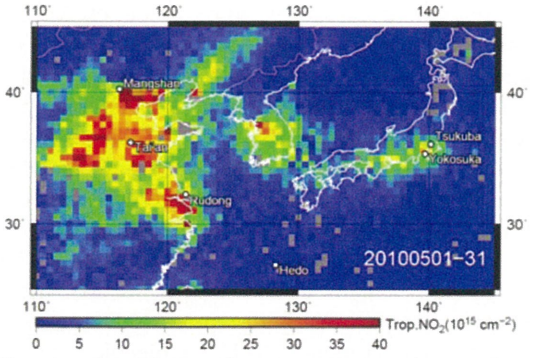

Fig. 1. Locations of MAX-DOAS observations on a monthly mean map (0.5° grid) of GOME-2 tropospheric NO_2 VCD data in May 2010.

(2011). For an NO_2 VCD of about 100×10^{14} molecules cm^{-2}, typical random errors were estimated to be 5×10^{14} molecules cm^{-2} (5%). Systematic errors due to uncertainty in the AMF determination, which is likely the dominant source of systematic error in our profile retrieval method, were estimated to be 7×10^{14} molecules cm^{-2} (7%). For the present study, additional sensitivity analysis is performed using a different fitting window for NO_2 (425-450 nm) and different NO_2 cross section data (at 220 K). The errors were estimated by a manner similar to Takashima et al. (2011b) to be about -3% (the VCD retrieved from 425-450 nm is smaller) and -23% (the VCD retrieved using the cross section at 220 K is smaller). Scaling the latter estimate to the actual temperature variation below 2 km (possibly cooled down to ~260 K at an altitude of 2 km) yields -11%. This value could be smaller, since NO_2 should be abundant near the surface, where the temperature is usually warmer than 260 K and occasionally can exceed 294 K. However, we quantified the overall uncertainty to be 14% as the root-mean squares of all the above estimated errors. The representative horizontal distance for air masses observed by MAX-DOAS was estimated to be about 10 km (Irie et al., 2011), a magnitude comparable to or better than the satellite observations. The temporal resolution was 30 minutes, which corresponds to a complete sequence of elevation angles. In the present study, a comparison is made only when the time difference between MAX-DOAS and satellite observations was less than 30 minutes.

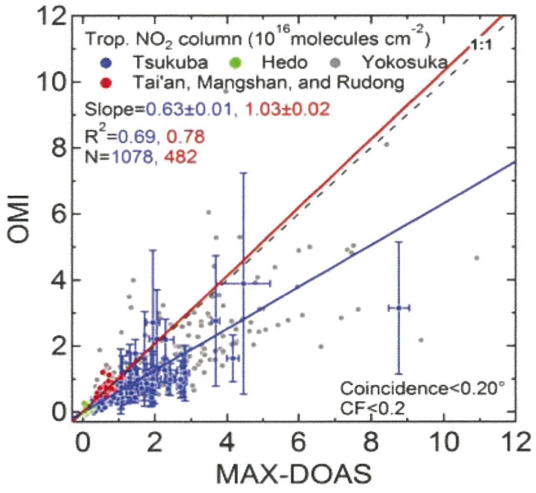

Fig. 2. Correlations between tropospheric NO_2 VCDs (10^{16} molecules cm^{-2}) from OMI and MAX-DOAS observations at a coincidence criterion (x) of 0.20°. Comparisons over Tsukuba, Hedo, and Yokosuka are shown in blue, green, and gray, respectively, and campaign-based short-term observations in China are shown in red. Error bars for both OMI and MAX-DOAS data are shown only for comparisons over Tsukuba at MAX-DOAS NO_2 VCDs larger than 1×10^{16} molecules cm^{-2}, for clarity. Linear regression analysis has been performed for the respective cases 1 (Tokyo case; blue) and 2 (Chinese case; red), where the slopes of their regression lines are constrained mainly by comparisons made around Tokyo (Tsukuba and Yokosuka) and at China sites (Tai'an, Mangshan, Rudong), respectively. Hedo data are used in both regression analyses but do not constrain the slope much, since the comparisons at other sites are made over a wide range of NO_2 VCD values. For each case, the slope, correlation coefficient (R^2), and number of data points (N) are given in the plot.

4. Results and Discussion

Here we compare MAX-DOAS observations performed in Japan and China in 2006-2011 with all three types of satellite products in a consistent manner. In Fig. 2, comparisons between MAX-DOAS and OMI tropospheric NO_2 column data are made only if the center of the OMI pixel is within 0.20° latitude and longitude of a MAX-DOAS observation point. This coincidence criterion is hereinafter denoted x. The coincidence criterion x of 0.20° is first tested here, while the comparison results could be affected by the choice of x according to the spatial distribution of NO_2 around observation sites, as discussed later. Two regression lines are shown in Fig. 2. The one shown in blue has been drawn from comparisons for Tsukuba, Yokosuka, and Hedo. The regression line shown in red was obtained from comparisons for three Chinese sites (Tai'an, Mangshan, and Rudong) and Hedo. The respective cases are called hereafter the Tokyo case and the China case. For the Tokyo case the slope is controlled mainly by data from Tsukuba and Yokosuka (both located around Tokyo), as their data are distributed over a wide range of NO_2 values compared to the Hedo data. Similarly, for the China case the slopes are controlled by data from the three Chinese sites. For comparisons over Hedo (shown in green), which is located in a remote area, both satellite and MAX-DOAS data consistently show very small NO_2 VCD values, compared to the other sites. The same features were seen for all the other cases investigated in this study. Considering this, the regression analysis has been made with the intercept forced to be zero, in order to simplify the interpretation of changes in the bias estimated from the slope of the regression line under various conditions. When the intercept is set as a variable, it is calculated to be 1.4×10^{15} molecules cm^{-2}. This is small compared to the range of NO_2 VCD data plotted in Fig. 2 but is larger than the error quoted for the satellite retrieval (~1.0×10^{15} molecules cm^{-2} + 30%). Furthermore, for example, comparisons between MAX-DOAS and GOME-2 under the same conditions as in Fig. 2 reveal that the intercept is as large as 3.0×10^{15} molecules cm^{-2} and is inconsistent with that estimated from the comparisons with OMI. We found that the intercept and therefore the slope tend to be influenced, at least when the number of comparisons is too small. This could complicate the interpretation of the change in slopes over different sensors and various coincidence criteria.

In Fig. 2, we find that the slope (± its 1σ standard deviation) is almost unity at 1.03±0.02 for the China case. The correlation coefficient (R^2) is as high as 0.78. On the other hand, for the Tokyo case the slope and R^2 are 0.63±0.01 and 0.69, respectively. When we perform the correlation analysis under conditions similar to those for the comparisons at the Chinese sites, in terms of the number of data points and season, the slope and R^2 were found to be essentially unchanged at 0.68±0.04 and 0.64, respectively. Also, analysis made under the same aerosol conditions using the MAX-DOAS aerosol optical depth (AOD) data at a wavelength of 476 nm reveals an insignificant impact by aerosols; at AOD smaller (greater) than 0.8 the slopes for the China and Tokyo cases are 1.04±0.04 (1.02±0.05) and 0.64±0.02 (0.62±0.05), respectively. The AOD threshold of 0.8 is taken from the statistics of retrieved AOD values at Tai'an, in order to evenly distribute the data to high and low AOD cases. Tai'an is the site that most contributes to the China case results for comparisons with OMI.

To investigate the cause of the difference between the slopes of the China and Tokyo cases, we make comparisons with various coincidence criteria. We test 15 different coincidence criteria: x = 0.05°, 0.10°, 0.15°, 0.20°, 0.25°, 0.30°, 0.35°, 0.40°, 0.45°, 0.50°, 0.60°, 0.70°, 0.80°, 0.90°, and 1.00°. Variations of the slope and R^2 over x are summarized in Figs. 3 and 4 for the Tokyo and China cases, respectively.

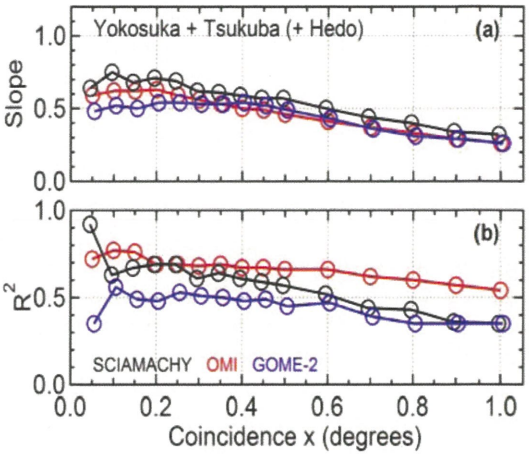

Fig. 3. (a) Slopes and (b) R^2 of the regression lines as a function of coincidence criterion x between satellite and MAX-DOAS observations for case 1 (Tokyo case)

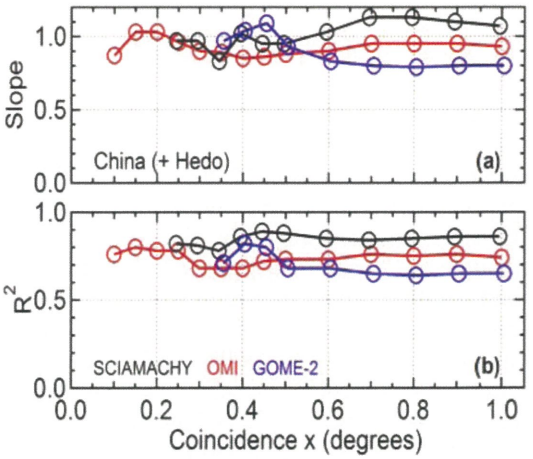

Fig. 4. Same as Fig. 3 but for case 2 (China case).

For the Tokyo case, it can be seen that the slopes of the regression lines tend to be smaller when a looser coincidence criterion is used, for all comparisons with SCIAMACHY, OMI, and GOME-2. It is thought that tropospheric NO_2 VCD values in the surrounding areas of Yokosuka and Tsukuba sites usually drop quickly, owing to limited NOx source regions. For a larger x, there should be a higher probability that the satellite footprints include clean air masses, and this can lower both the slope and R^2.

The Yokosuka site is surrounded by industrial facilities, ocean (Tokyo Bay), heavy ship activity, etc., resulting in a large range of tropospheric NO_2 VCDs but more scatter in the correlation, compared to the Tsukuba data (Fig. 2). To better address such influences of spatial inhomogeneity within a satellite pixel, validation observations covering several points in a satellite pixel at the same time would be desirable (e.g., Piters et al., 2012).

In Fig. 5, monthly-mean values of tropospheric NO_2 VCDs retrieved from satellite observations over Yokosuka are plotted. The color represents the spatial grid size for averaging; for x = 0.2°, for example, an average for NO_2 VCDs within 0.2° latitude and longitude of Yokosuka is shown. As the degree of the spatial inhomogeneity varied with time significantly, it was difficult to uniquely determine the best single choice of x as a typical spatial scale for the bias estimate.

Results of the estimated slopes and R^2 for the China case are shown in Fig. 4. Results with an insufficient number of comparisons (less than 3) at Chinese sites have been omitted. It can be seen that the slopes slowly vary with x, but the variations are not as systematic as those of the Tokyo case. R^2 values are greater than 0.6 for all comparisons and usually higher than those for the Tokyo case (Figs. 3 and 4). Furthermore, dependencies of satellite-retrieved tropospheric NO_2 VCDs on x are not as systematic as those seen at sites of the Tokyo case (not shown). These suggest that the spatial distributions of tropospheric NO_2 VCDs around the Chinese sites during the observation periods were rather homogeneous and therefore appropriate for bias estimates.

For the China case, by simply averaging the slopes over the entire x range, the biases with respect to MAX-DOAS observations are estimated to be 0±14%, -8±14%, and -10±14% for SCIAMACHY, OMI, and GOME-2, respectively (Table 1). The error is calculated as the root-sum-squares of the uncertainty of the slope and the uncertainty of the MAX-DOAS NO_2 retrieval. It is expected, however, that the validation comparison can be more precise using a stricter coincidence criterion owing to the increased probability of observing the same air masses by a satellite sensor and MAX-DOAS. Considering this, our best estimates of the biases from slopes at a strict x range

below 0.50° are -5±14%, -10±14%, and +1±14% for SCIAMACHY, OMI, and GOME-2, respectively (Table 1). Thus, we conclude that the biases are less than about 10% and insignificant for all three data sets.

Note that considering the error quoted for satellite retrievals (~1 × 10^{15} molecules cm^{-2} + 30%), the estimate biases may be invalid, at least, at NO_2 VCD values smaller than ~1 × 10^{15} molecules cm^{-2}. Also, the estimated biases could vary by changing the x range, but we note that the slopes are all less than 20% irrespective of the choice of x (Fig. 4). In the above bias estimates, the slopes for the Tokyo cases are not included as the slopes vary significantly with x. However, very similar slopes are obtained for all comparisons with SCIAMACHY, OMI, and GOME-2 in the Tokyo case (Fig. 3), supporting the conclusion that differences among biases for all sensors are small, as found from the China case. Thus, our study confirms the hypothesized consistent quality KNMI products retrieved with the new method of Boersma et al. (2011).

Finally, there is the possibility that the biases between satellite and MAX-DOAS data are not necessarily constant over location and time. To address this issue, the precise validation for MAX-DOAS retrievals and/or more systematic MAX-DOAS observations would be essential.

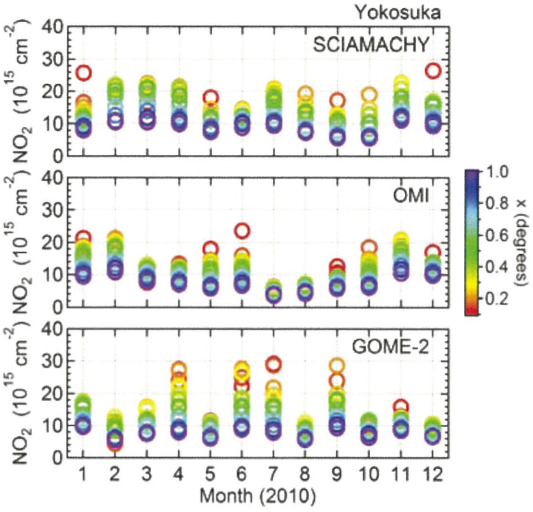

Fig. 5. Dependence of satellite-retrieved tropospheric NO_2 VCDs on the spatial grid size used for averaging (corresponding to the coincidence criterion x) around Yokosuka for each month in 2010. All available cloud-free satellite data are used.

5. Conclusions

To quantify the biases in the tropospheric NO_2 VCD data from SCIAMACHY, OMI, and GOME-2 in a consistent manner, we created a single data set from MAX-DOAS observations performed at three sites in Japan and three sites in China in 2006-2011. Regression analysis between satellite and MAX-DOAS tropospheric NO_2 VCDs showed that the slope of the regression line tends to be biased by the distance between MAX-DOAS and satellite observation points, due to a difference in the spatial representativeness between MAX-DOAS and satellite observations under loose coincidence criteria. This feature is more clearly seen around Tokyo with strong spatial gradients in air pollution. These results serve as a guideline for future satellite validation, in terms of the choice of coincidence criteria and validation sites. We recommend conducting validation observations under relatively homogeneously polluted conditions. From the slopes of the regression lines for strict coincidence criteria, we estimated biases in SCIAMACHY, OMI, and GOME-2 data to be -5±14%, -10±14%, and +1±14%, respectively, compared to the MAX-DOAS data. Thus, we conclude that the biases are less than about 10% and insignificant for all three data sets. With a consideration of these characteristics, the present study encourages the combination of these satellite data to realize air quality studies that are more systematic and quantitative than previously possible.

Table 1. Estimated Biases in Satellite Tropospheric NO_2 Products for Different Coincidence Criterion Thresholds.

Sensor	$x \leq 0.5°$	$x \leq 1.0°$
SCIAMACHY	-5±14%	0±14%
OMI	-10±14%	-8±14%
GOME-2	+1±14%	-10±14%

Acknowledgments

We thank PREDE, Co., Ltd for their technical assistance in developing the MAX-DOAS instruments. Observations at Tsukuba were supported by M. Nakazato and T. Nagai. This work was supported by the Global Environment Research Fund (S-7) of the Ministry of the Environment, Japan, and by the Netherlands Organisation for Scientific Research, NWO Vidi grant 864.09.001.

References

Boersma, K. F., Eskes, H. J., and Brinksma, E. J., 2004. Error Analysis for tropospheric NO_2 retrieval from space, J. Geophys. Res. 109, D04311, doi:10.1029/2003JD003962.

Boersma, K. F., Eskes, H. J., Veefkind, J. P., Brinksma, E. J., van der A, R. J., Sneep, M., van den Oord, G. H. J., Levelt, P. F., Stammes, P., Gleason, J. F., and Bucsela, E. J., 2007. Near-real time retrieval of tropospheric NO_2 from OMI, Atm. Chem. Phys., 7, pp. 2013-2118.

Boersma, K.F., Jacob, D. J., Eskes, H. J., Pinder, R. W., Wang, J., and van der A, R. J., 2008. Intercomparison of SCIAMACHY and OMI tropospheric NO_2 columns: Observing the diurnal evolution of chemistry and emissions from space, J. Geophys. Res., 113, D16S26, doi:10.1029/2007JD008816.

Boersma, K. F., Jacob, D. J., Trainic, M., Rudich, Y., DeSmedt, I., Dirksen, R., and Eskes, H. J., 2009. Validation of urban NO_2 concentrations and their diurnal and seasonal variations observed from the SCIAMACHY and OMI sensors using in situ surface measurements in Israeli cities, Atmos. Chem. Phys., 9, pp. 3867–3879, doi:10.5194/acp-9-3867-2009.
Boersma, K. F., Eskes, H. J., Dirksen, R. J., van der A, R. J., Veefkind, J. P., Stammes, P., Huijnen, V., Kleipool, Q. L., Sneep, M., Claas, J., Leitão, J., Richter, A., Zhou, Y., and Brunner, D., 2011. An improved tropospheric NO_2 column retrieval algorithm for the Ozone Monitoring Instrument, Atmos. Meas. Tech., 4, pp. 1905-1928
Bovensmann, H., Burrows, J. P., Buchwitz, M., Frerick, J., Noel, S., Rozanov, V. V., Chance, K. V., and Goede, A. H. P., 1999: SCIAMACHY – Mission objectives and measurement modes, J. Atmos. Sci., 56(2), pp. 127–150
Callies, J., Corpaccioli, E., Eisinger, M., Hahne, A., and Lefebvre, A., 2000. GOME-2- Metop's second-generation sensor for operational ozone monitoring, ESA Bull., 102, pp. 28–36.
Hönninger, G., and Platt, U., 2002. Observations of BrO and its vertical distribution during surface ozone depletion at Alert, Atmos. Environ., 36, pp. 2481-2489.
Hönninger, G., von Friedeburg, C., and Platt, U., 2004. Multi axis differential optical absorption spectroscopy (MAX-DOAS), Atmos. Chem. Phys., 4, pp. 231-254.
Irie, H., Kanaya, Y., Akimoto, H., Iwabuchi, H., Shimizu, A., and Aoki, K., 2008. First retrieval of tropospheric aerosol profiles using MAX-DOAS and comparison with lidar and sky radiometer measurements, Atmos. Chem. Phys., 8, pp. 341–350.
Irie, H., Kanaya, Y., Takashima, H., Gleason, J. F., and Wang, Z., 2009. Characterization of OMI tropospheric NO_2 measurements in East Asia based on a robust validation comparison, SOLA, 5, pp. 117-120, doi:10.2151/sola.2009–030.
Irie, H., Takashima, H., Kanaya, Y., Boersma, K. F., Gast, L., Wittrock, F., Brunner, D., Zhou, Y., and Van Roozendael, M., 2011. Eight-component retrievals from ground-based MAX-DOAS observations, Atmos. Meas. Tech., 4, pp. 1027-1044.
Levelt, P. F., van den Oord, G. H. J., Dobber, M. R., Malkki, A., Visser, H., de Vries, J., Stammes, P., Lundell, J., and Saari, H., 2006. The Ozone Monitoring Instrument, IEEE Trans. Geo. Rem. Sens., 44, 5, pp. 1093–1101, doi:10.1109/TGRS.2006.872333, 2006.
Lin, J.-T, McElroy, M. B., and Boersma, K. F., 2010. Constraint of anthropogenic NO_x emissions in China from different sectors: A new methodology using multiple satellite retrievals, Atmos. Chem. Phys., 10, pp. 63–78.
Piters, A. J. M., Boersma, K. F., Kroon, M., Hains, J. C., Van Roozendael, M., Wittrock, F., Abuhassan, N., Adams, C., Akrami, M., Allaart, M. A. F., Apituley, A., Bergwerff, J. B., Berkhout, A. J. C., Brunner, D., Cede, A., Chong, J., Clémer, K., Fayt, C., Frieß, U., Gast, L. F. L., Gil-Ojeda, M., Goutail, F., Graves, R., Griesfeller, A., Großmann, K., Hemerijckx, G., Hendrick, F., Henzing, B., Herman, J., Hermans, C., Hoexum, M., van der Hoff, G. R., Irie, H., Johnston, P. V., Kanaya, Y., Kim, Y. J., Baltink, H. K., Kreher, K., de Leeuw, G., Leigh, R., Merlaud, A., Moerman, M. M., Monks, P. S., Mount, G. H., Navarro-Comas, M., Oetjen, H., Pazmino, A., Perez-Camacho, M., Peters, E., du Piesanie, A., Pinardi, G., Puentadura, O., Richter, A., Roscoe, H. K., Schönhardt, A., Schwarzenbach, B., Shaiganfar, R., Sluis, W., Spinei, E., Stolk, A. P., Strong, K., Swart, D. P. J., Takashima, H., Vlemmix, T., Vrekoussis, M., Wagner, T., Whyte, C., Wilson, K. M., Yela, M., Yilmaz, S., Zieger, P., and Zhou, Y., 2012. The Cabauw Intercomparison campaign for Nitrogen Dioxide measuring Instruments (CINDI): design, execution, and early results, Atmos. Meas. Tech., 5, pp. 457-485.
Roscoe, H. K., Van Roozendael, M., Fayt, C., du Piesanie, A., Abuhassan, N., Adams, C., Akrami, M., Cede, A., Chong, J., Clémer, K., Frieß, U., Ojeda, M. G., Goutail, F., Graves, R., Griesfeller, A., Grossmann, K., Hemerijckx, G., Hendrick, F., Herman, J., Hermans, C., Irie, H., Kanaya, Y., Kreher, K., Johnston, P., Leigh, R., Merlaud, A., Mount, G. H., Navarro, M., Oetjen, H., Pazmino, A., Perez-Camacho, M., Peters, E., Pinardi, G., Puentedura, O., Richter, A., Schönhardt, A., Shaiganfar, R., Spinei, E., Strong, K., Takashima, H., Vlemmix, T., Vrekoussis, M., Wagner, T., Wittrock, F., Yela, M., Yilmaz, S., Boersma, F., Hains, J., Kroon, M., and Piters, A., 2010. Intercomparison of slant column measurements of NO_2 and O_4 by MAX-DOAS and zenith sky UV and visible spectrometers, Atmos. Meas. Tech., 3, pp. 1629-1646.
Takashima, H., Irie, H., Kanaya, Y., and Akimoto, H., 2011a. Enhanced NO_2 at Okinawa Island, Japan caused by rapid air-mass transport from China as observed by MAX-DOAS, Atmos. Environ., 45, pp. 2593-2597.
Takashima, H., H. Irie, Y. Kanaya, and F. Syamsudin, 2011b. NO_2 observations over the western Pacific and Indian Ocean by MAX-DOAS on Kaiyo, a Japanese research vessel, Atmospheric Measurement Techniques Discussion, 4, pp. 6069-6095.
Vandaele, A.C., Hermans, C., Simon, P.C., Carleer, M., Colin, R., Fally, S., Mérienne, M.F., Jenouvrier, A., and Coquart, B., 1998. Measurements of the NO_2 absorption cross-section from 42000 cm^{-1} to 10000 cm^{-1} (238-1000 nm) at 220 K and 294 K, J. Quant. Spectrosc. Radiat. Transfer, 59, pp. 171-184.

COMBINED PANSHARPENING APPROACH FOR OBJECT-BASED IMAGE ANALYSIS

Brian Johnson[1] and Ryutaro Tateishi[*2]

[1]JSPS Research Fellow, Center for Environmental Remote Sensing (CEReS), Chiba University,
1-33 Yayoi Cho, Inage Ku, Chiba Shi, Chiba, Japan; Tel: + 81-43-290-3850;
E-mail: bjohns53@fau.edu

[2]Professor, Center for Environmental Remote Sensing (CEReS), Chiba University,
1-33 Yayoi Cho, Inage Ku, Chiba Shi, Chiba, Japan; Tel: + 81-43-290-3850;
E-mail: tateishi@faculty.chiba-u.jp

KEY WORDS: image segmentation, image pansharpening, object-based image analysis, high resolution data

ABSTRACT: Intensity-Hue-Saturation (IHS), Brovey Transform (BT), and Smoothing-Filter-Based-Intensity Modulation (SFIM) algorithms were used to pansharpen GeoEye-1 imagery. The pansharpened images were then segmented in Berkeley Image Seg using a wide range of segmentation parameters, and the spatial and spectral accuracy of image segments was measured. We found that pansharpening algorithms that preserve more of the spatial information of the higher resolution panchromatic image band (i.e., IHS and BT) led to more spatially-accurate segmentations, while pansharpening algorithms that minimize the distortion of spectral information of the lower resolution multispectral image bands (i.e., SFIM) led to more spectrally-accurate image segments. Based on these findings, we developed a new IHS-SFIM combination approach, specifically for object-based image analysis (OBIA), which combined the better spatial information of IHS and the more accurate spectral information of SFIM to produce image segments with very high spatial and spectral accuracy.

1. IMAGE PANSHARPENING AND SEGMENTATION

1.1 Introduction

A large number of pansharpening algorithms have been developed in recent years. Some preserve almost all of the spatial details in the panshromatic (PAN) image band but significantly distort the information in the multispectral (MS) bands, while others preserve more accurate MS information at the cost of some reduction in spatial information. In this study, we developed a new hybrid pansharpening approach that allows for better spatial and spectral information to be extracted from an image. In this paper, we give the most important information about our hybrid pansharpening method. For further details, readers are referred to Johnson et al. (2012).

1.1 Methods

GeoEye-1 imagery was acquired of a rural area and a forested area in Ishikawa Prefecture, Japan. The imagery contained four 2m resolution multispectral (MS) bands and a 0.5m panchromatic (PAN) band. We pansharpened the two images using the four-band IHS algorithm given by Tu et al. (2004) because it was shown to lead to spatially-accurate image segmentation (Johnson et al., 2012). The pansharpened images were segmented in Berkeley Image Seg using approximately 100 different segmentation parameters. To identify the most spatially-accurate segmentation (i.e. the one with the best spatial match between image segments and real-world objects of interest), we calculated the similarity between image segments and manually-digitized reference polygons using the "D Metric" (D) from Clinton et al. (2010). For the rural image, reference polygons were digitized for buildings and individual trees, and for the forested image we digitized reference polygons of individual diseased trees. For each pansharpened image, the segmentation with the lowest D value was chosen as the most spatially-accurate segmentation. Since IHS pansharpening significantly distorts the MS information, we replaced the IHS spectral information of image segments (e.g. mean values for each band) with the spectral information from a SFIM (Liu, 2000) pansharpened image. SFIM introduces very little spectral distortion to the MS bands, but is not as efficient as IHS for preserving the spatial details of the PAN band, making it less appropriate for image segmentation (Johnson et al., 2012). The end result was a segmented image with higher spatial and spectral accuracy than what could be obtained using a single pansharpening method alone. Figure 1 shows a graphical representation of the hybrid IHS-SFIM approach.

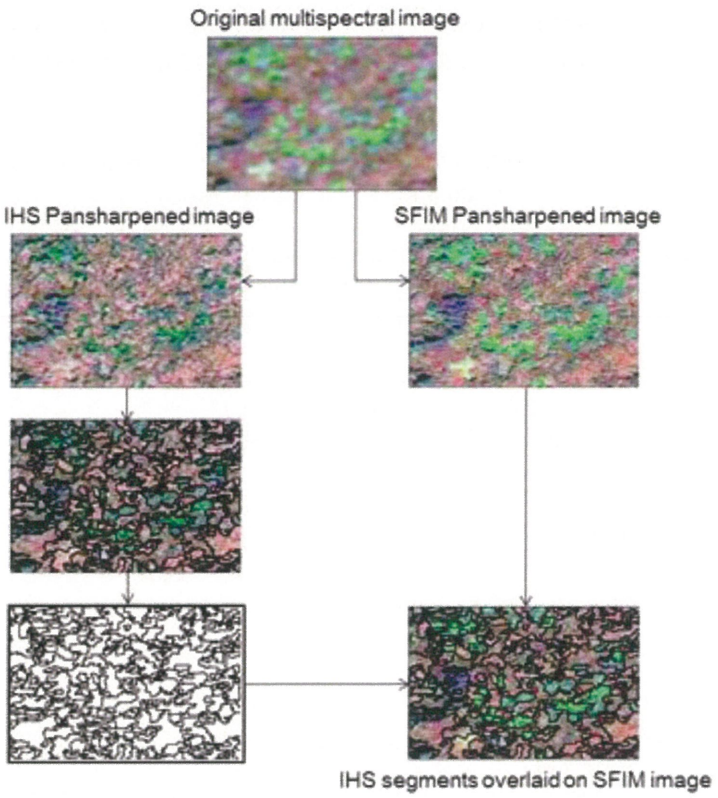

Figure 1. Graphical representation of IHS-SFIM pansharpening approach. IHS image is used for segmentation to derive polygon boundaries of objects of interest, and SFIM spectral information is extracted for each of these polygons (rather than IHS spectral information).

2. CONCLUSIONS

To combine the high spatial accuracy of IHS segments with the high spectral accuracy of SFIM pansharpened imagery, we proposed a hybrid approach developed specifically for OBIA that involves (i) overlaying the segment boundaries from the IHS image segmentation onto a SFIM image and (ii) deriving the spectral values for image segments (mean DN for each spectral band) from the SFIM imagery. We recommend users planning to process images with PAN and MS bands using OBIA to pansharpen the imagery themselves (rather than purchase pansharpened imagery directly from the image vendor) so that they can incorporate multiple pansharpening methods for their analysis. Finally, since image classification often follows image segmentation in OBIA, future studies are needed to quantitatively assess the impact that different pansharpening algorithms and our proposed hybrid approach have on classification accuracy.

2. REFERENCES

Clinton, N., Holt, A., Scarborough, J., Yan, L., Gong, P., 2010. Accuracy assessment measure for object-based image segmentation goodness. Photogrammetric Engineering & Remote Sensing, 76, pp. 289–299.

Johnson, B., Tateishi, R., Hoan, N., 2012. Satellite image pansharpening using a hybrid approach for object-based image analysis. ISPRS International Journal of Geo-Information, 1, pp. 228-241.

Liu, J., 2000. Smoothing filter-based intensity modulation: a spectral preserve image fusion technique for improving spatial details. International Journal of Remote Sensing, 21, pp. 3461–3472.

Tu, T., Huang, P., Hung, C., Chang, C., 2004. A fast intensity-hue-saturation fusion technique with spectral adjustment for IKONOS imagery. IEEE Geoscience and Remote Sensing Letters, 1, pp. 309–312.

AEROSOL PROPERTY ANALYSIS USING MULTI-WAVELENGTH LIDAR AND GROUND AEROSOL MEASURING INSTRUMENTS

Hayato Saito[1] Yusaku Mabuchi[1], Naohiro Manago[1], Gerry Bagtasa[1], Nobuo takeuchi[1], Masanori Yabuki[2], Tatsuo Shiina[1], and Hiroaki Kuze[1]

[1]Center for environmental remote sensing (CEReS), Chiba University,
1-33 Yayoi Cho, Inage Ku, Chiba Shi, Chiba, 263-8522 Japan;
E-mail: hkuze@faculty.chiba-u.jp [Hiroaki Kuze]

[2]Research Institute for Sustainable Humanosphere, Kyoto University,
Gosasho, Uji, Kyoto 611-0011, Japan
E-mail: yabuki@rish.kyoto-u.ac.jp [Masanori Yabuki]

KEY WORDS: Aerosols, Atmosphere, Lidar, Remote sensing,

ABSTRACT: Atmospheric Data Collection Lidar (ADCL) is a multi-wavelength lidar system designed for measuring tropospheric aerosols and clouds with auxiliary data from ground-based aerosol measurement instruments. In this paper, we report on the concept of aerosol and cloud retrieval based on vertical, slant-path, and plan-position indicator (PPI) lidar measurements in combination with aerosol measurements conducted with a three-wavelength integrating nephelometer, an aethalometer, and a particle counter. Such a combined approach makes it possible to study the detailed features of aerosols in the troposphere, including the aerosol-cloud interaction.

1, INTRODUCTION

Both direct and indirect effects of aerosol particles affect the Earth's radiation budget. The direct effect is due to reflection and/or absorption of radiation, leading to negative/positive effect on the radiative forcing (Coakley Jr. and Cess, 1983). The indirect effect, on the other hand, is caused by cloud particles, the formation of which is largely influenced by the role of aerosols as condensation nuclei (Jaenicke, 1993). Therefore, it is important to precisely monitor aerosol amount and property from the viewpoint of evaluating future trends in climate change. The atmospheric data collection lidar (ADCL) at the Center for Environmental Remote Sensing (CEReS), Chiba University, has been designed to carry out such monitoring of tropospheric aerosols and clouds (Mabuchi et al., 2012). Briefly, the system consists of the following three subsystems. The first subsystem is a multi-wavelength lidar system, consisting of a three-wavelength lidar, Raman lidars, a high spectral resolution lidar, and a slant-path lidar. The second subsystem is a set of ground aerosol sampling instruments, namely, a three-wavelength nephelometer, a multi-wavelength aethalometer and an optical particle counter. These instruments measure scattering/absorption properties as well as size distributions. The third category is a plan position indicator (PPI) mode lidar instrument, used to derive information on horizontal distribution of aerosols. The simultaneous measurements using these instruments enable us to make comprehensive analysis of aerosol and cloud particles without resorting to assumptions of cloud-free conditions and/or a priori knowledge on the values of wavelength dependent lidar ratio, which have so far hindered quantitative interpretation of multi-wavelength lidar signals.

2. INSTRUMENTS

ADCL has a variety of options for observing the atmosphere from different perspectives by using many wavelengths. Here we focus on aerosols extinction, scattering and particle size distribution derived from lidar and ground-based measurements. Table 1 summarizes the specifications for major lidar units, while Table 2 those of aerosol characterization instruments.

Table 1. Specification and major products of ADCL lidar units.

Type	Wavelength (nm)	Telescope (diameter (mm))	Product
Mie, Raman	355, 387, 408	Raymetrics DK 350 (350)	Back scattering
	532, 607	Meade LX 200 (350)	N2 and WV Raman
Mie	1064	Meade LX 200 (300)	
P/S	532	Meade LX 200 (300)	Depolarization ratio
HSRL	532	Meade LX 200 (250)	Lidar ratio
PPI (Mie)	349	Raymetrics DK 300 (300)	Horizontal distribution
Slant(Mie)	532	Meade LX 200 (200)	Lower vertical profile

Table 2. Specification of ground-based aerosol measurement instruments.

Instrument	Parameters
Optical Particle Counter Rion KC-22B	Particle size distribution 0.08, 0.1, 0.2, 0.3, 0.5 μ m
Aethalometer Magee Scientific AE-31	Absorption coefficient 370, 470, 520, 590, 660, 880, 950 nm
Integrating Nephelometer TSI model 3563	Scattering coefficient 450, 550, 700 nm

Below we report the results from a campaign observation conducted during 6-10 August 2012. During this period, various types of weather conditions were observed, including clear sky, cloudy, as well as rainy and humid conditions. Both the vertical (355, 532, 1064nm) and slant-path (532nm) lidar units were operated for measuring vertical and near-ground-level distributions of aerosol particles. Additionally, the PPI-mode lidar (349nm) provides the information on the homogeneity of aerosol distribution in the horizontal plane. Along with the lidar measurements, an optical particle counter, an aethalometer, and an integrating nephelometer were employed for measuring aerosol size distribution, absorption coefficient, and scattering coefficient. As explained below, these values are useful for obtaining the boundary conditions of lidar equations that are solved to retrieve the aerosol vertical profiles.

4. RESULTS AND ANALYSIS

For solving lidar equation by forward or backward inversion, (Fernald, 1984), one needs to determine the lidar ratio (S_1: extinction-to-backscattering ratio) and a reference value of extinction coefficient at certain range where aerosol scattering is negligibly small (Fernald et al., 1972). Since the value of S_1 can vary from 10 to 100 sr (Parameswaran

et al., 1991; Gobbi, 1995), accurate determination of S_1 is important for deriving the vertical distribution of aerosols extinction coefficient in an accurate way. Another problem generally encountered in a lidar observation is the existence of the non-overlapping range in the vicinity of the ground level (Kuze, 1998), since the strong signal from the near-end region would cause problems for sensitive detectors. In the ADCL configuration, this region is effectively covered by the slant-path lidar data. Besides, when generalizing slant-path lidar data, we have to assume horizontal homogeneity of the atmosphere around the observation site. The PPI-mode observation can be used to ensure the homogeneity condition (i. e. layered structure) of the aerosol distribution. Under such a homogeneous condition, the extinction profiles derived from the slant-path observation can be used to constraint the vertical lidar data.

Figure 1 shows the temporal change of aerosol extinction profiles observed on 10 August 2012. In the afternoon, clouds were observed in the altitude range of 4 to 10 km, hindering the observation of the aerosol-free region, normally above 5 or 6 km. Thus, the ground observation data in combination with the slant-path lidar data (Fig. 1b) are used to determine the boundary conditions at the near end. The homogeneity condition, on the other hand, can

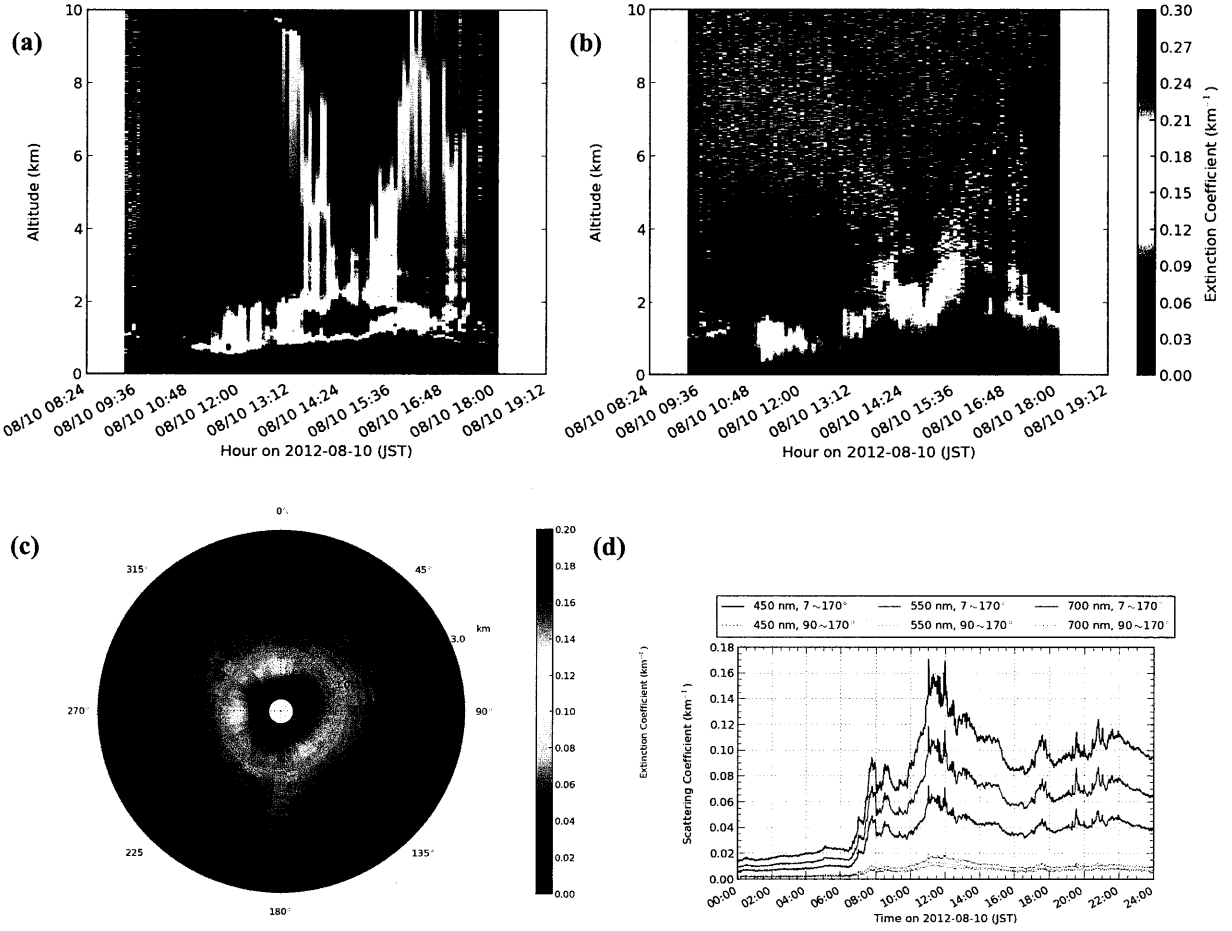

Figure 1. (a) Vertical path lidar signal and (b) slant-path lidar observation data at 532 nm wavelength. (c) PPI-mode lidar observation data at 349nm wavelength. (d) extinction coefficient measured by ground sampling instrument.

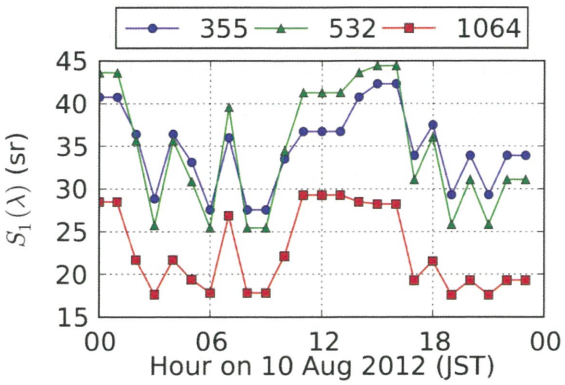

Figure 2. Temporal variation of the lidar ratio (S_1) derived for the tree lidar wavelengths (355, 532, and 1064 nm) from the ground-based measurement with the help of Mie-scattering calculation.

be ensured from the PPI-mode lidar observation (Fig.1c). The capability of ADCL for obtaining the data below clouds would be useful for the study of aerosol-cloud interaction, which is the basis for the indirect effect of aerosol particles in the radiation budget analysis. Figure 2 shows the temporal variation of the lidar ratio (S_1) derived for the tree lidar wavelengths (355, 532, and 1064 nm) from the ground-based measurement with the help of Mie-scattering calculation.

6. CONCLUSION

We have described the instrumental aspects and operation principle of the atmospheric data collection lidar (ADCL) recently installed at CEReS. The combined analysis of signals from the vertical lidar. slant-path lidar, PPI lidar, as well as ground observation data on the aerosol properties is useful for studying the aerosol and cloud optical characteristics without concerning the presence of clouds. We are planning to exploit the data from future ADCL campaigns to elucidate various aspects of aerosol particles in the Chiba area.

REFFERENCES

Fernald, F.G., B.M. Herman and J.A. Reagan, 1972: Determination of aerosol height distributions by lidar, J.Appl. Meteorol. 11, p.482,

Fernald, F. G., 1984: Analysis of atmospheric lidar observation: some comments, Appl. Opt., 23, pp.652 (1984).

Gobbi. G. P, 1995: Lidar estimation of stratospheric aerosol properties: Surface, volume, and extinction to backscatter ratio, J. Geophys. Res., 100, 11,219-11,235

Jaenicke, R, 1993: Tropospheric Aerosols in "Aerosol-Cloud-Climate Interactions", ed. P.V. Hobbs, Academic Press.

J.A. Coakley Jr. and R.D. Cess, 1983: The Effect of Tropospheric Aerosols on the Earth's Radiation Budget: A Parameterization for Climate Models, J. Atmospheric Science, 40, pp. 116-138.

Kinjo, H., H. Kuze, Y. Sakurada, and N. Takeuchi, 1999: Calibration of the Lidar Measurement of Tropospheric Aerosol Extinction Coefficients, Jpn. J. Appl. Phys., 38, pp. 293-297.

Kuze, H., H. Kinjo, Y. Sakurada, and N. Takeuchi, 1998: Field-of-view dependence of lidar signals by use of Newtonian and Cassegranian telescopes, Appl. Opt., 37, pp. 3128-3132.

Mabuchi, Y., N. Manago, G. Bagtasa, H.Saito, N. Takeuchi, M. Yabuki, T. Shiina, and H. Kuze, 2012: Multi-wavelength lidar system for the characterization of tropospheric aerosols and clouds, IGARSS TUP467.

Parameswaran. K, K.O. Rose. and B.V.K. Murthy, 1991: Relationship between backscattering and extinction coefficients of aerosols with application to turbid atmosphere, Appl. Opt., 30, 3059-3071.

Yabuki, M., H. Kuze, H. Kinjo, and N. Takeuchi, 2003: Determination of vertical distributions of aerosol optical parameters by use of multi-wavelength lidar data, Jpn. J. Appl. Phys., 42, pp. 686-694.

Surface Energy Balance Interface Software (SEBALIS) development to process satellite data and its application to the study of urban climate

Laras Tursilowati[1,2], Josaphat Tetuko Sri Sumantyo[1], Hiroaki Kuze[1], Erna Sri Adiningsih[2]
[1]Center for Environmental Remote Sensing (CEReS), Chiba University, Japan
[2]National Institute of Aeronautics and Space (LAPAN), Indonesia.

Corresponding Author: Laras Tursilowati
laras@restaff.chiba-u.jp

Abstract
In the recent study have been successfully created the Surface Energy Balance Interface Software (SEBALIS) using Visual Basic (VB) 6.0 program. This software can simplify the existing system and the formulation, facilitates data processing by reducing repetitive and complex tasks implemented with the ErMapper software. The urban climate variables have been calculated in SEBALIS are surface temperature (*Ts*), air temperature (*Ta*), net radiation (*Rn*), soil heat flux (*G*), latent heat flux (*L*), sensible heat flux (*H*), and evapotranspiration (*Etp*) for each land cover in urban areas. The development of SEBALIS lies in the additional the formulation and estimation of urban climate variables (Normalized Difference Vegetation Index (*NDVI*), relative humidity (*RH*), comfortable index (*THI*), Bowen ratio (β), and evaporative fraction (*EF*)). This SEBALIS that developed has been applied for monitoring drought in Bandung.

Keywords: SEBALIS development, Visual Basic 6.0, ErMapper, ArcView GIS, urban climate variables (*NDVI*, β, and *EF*), drought monitoring.

INTRODUCTION

The Surface Energy Balance Interface Software (SEBALIS) has been created using Visual Basic 6.0 program. This software is designed to simplify the existing system and the formulation. SEBALIS was created as a tool for supporting the research activities conducted by the National Institute of Aeronautics and Space (LAPAN)-Indonesia, and Center for Environmental Remote Sensing (CEReS) Chiba University – Japan (Tursilowati et al., 2012a). The issues concerning climate change locally, regionally and globally has been debated among scientists, economics, politics and others. Local (urban) climate change is associated with changes in land use. There is an increasing recognition of the role of cities and urban regions as key engines of economic growth, job creation and innovation – as well as their role as the major contributors to global warming. Climate impacts will result from global climate change, but how climate change impacts individual metropolitan regions will vary (OECD, 2010). Therefore, this software created to support research in the field of urban climate and its relation to land use. SEBALIS based on the Visual Basic (VB) platform that can simplify the formulation so that the utilization of other existing programs is reduced considerably in the development of simulation model. As an example, here we apply the novel VB system to analyzing the energy balance in big cities in Indonesia (Tursilowati et al., 2012a, Datta, 2008, Ford, 2009, Foxall, 2010, Halvorson, 2010, and Hassan et al., 2006).

In the previous version of SEBALIS could be process the Landsat satellite data and generate the distribution of energy balance is closely investigated over various types of land coverage including water body, forest, industry, plantations, residence, paddy fields, open land,

embankment, and cloud. The distribution presenting surface reflectance (albedo), surface temperature (*Ts*), air temperature (*Ta*), the components of energy balance (net radiation, *Rn*), soil heat flux (*G*), latent heat flux (*L*), sensible heat flux (*H*)), and evapotranspiration (*Etp*) are generated to design the necessary system models on the basis of relevant satellite images (Tursilowati et al., 2012a). In this study was conducted development SEBALIS to estimate the other climate variables, namely Normalize Difference Vegatation Index (*NDVI*), Evaporative Fraction (*EF*), and Bowen Ratio (β). *EF* and β are essential climate variables for drought monitoring (Julien et al., 2011, and Wan et al., 2004).

Drought is a problem that often arises in Indonesia during the dry season arrives. Various methods of drought monitoring with satellite remote sensing data have been implemented. Vogt et al. (1998), Niemeyer and Vogt (1999) describe concept that is the energy balance and Evaporative Fraction (*EF*) for monitoring drought in the region Sicilia. *EF* is the ratio between the energy to do with the difference in evapotranspiration net radiation with energy to move the heat in the soil. On the ground condition do not contain water, energy for Evapotranspiration (*ET*) decreased so that *EF* decreased. In this case the lower the evaporative fraction, then the drought level will be higher. The opposite of the concept of *EF* is the Bowen Ratio (*BR*), which explains that the higher the value of *BR* will be higher levels of dryness of the land (Tursilowati et al., 2012b).

METHODOLOGY

An outline, the methodology carried out by Waterfall approach. Waterfall method is, generally in use in the development of a system or application software that has long been widely known, very powerful software development methodology and consists of four phases that, in general, map to the four phases of the Kumiega-Van Vliet model analysis, design, implementation, and ongoing system testing (Van Vliet and Hendry, 2004). The methodology describes the procedure of processing of raw data and initial processing of Landsat satellite images, data extraction to urban climate variables to the analysis and visualization. In the previous study the urban climate variables consist of the albedo, *Ts*, *Ta*, surface energy balance components (*Rn*, *G*, *H*, and *L*), and evapotranspiration (*Etp*). In this study contunues estimate other climate variables, namely Normalize Difference Vegatation Index (*NDVI*), Evaporative Fraction (*EF*), and Bowen Ratio (β). Initial processing of raw image data to be output ASCII data is done by using the Er Mapper 7.1 software. Landsat data extraction for the numerical calculations performed using SEBALIS that has been developed. While the reclassification process the data until the final layout is done using the software ArcView GIS 3.3.

Chart design of Surface Energy Balance Model in this study shown as Figure 1. In Figure 1 shown in the box output, climate variables estimated in this study are marked in red color, namely *NDVI*, β, and *EF*.

The data used in the study were as follows: Landsat 7 ETM with study area covered Bandung area (Path 122, Row 065) dated 22 December 2001 with the acquisition L1G format, digital map of Bandung administration, digital maps of Bandung land use.

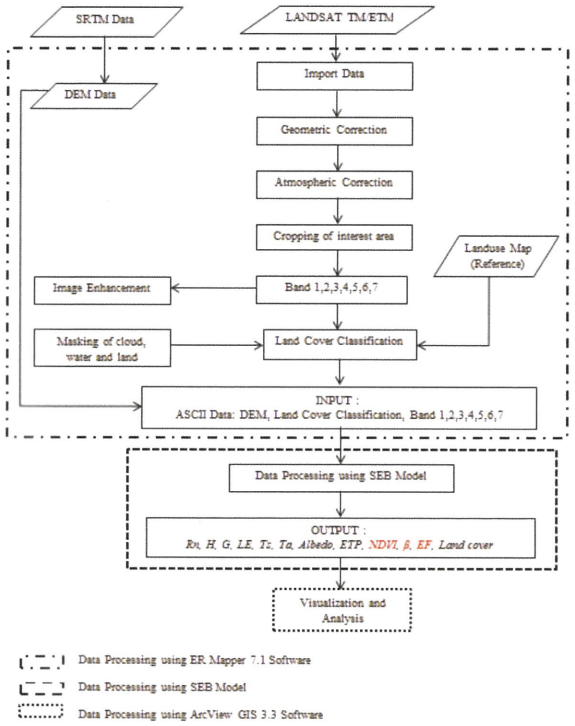

Figure 1. Chart design of Surface Energy Balance Model Interface Model

RESULT AND DISCUSSION

This SEBALIS that developed has been applied for monitoring drought in Bandung (Tursilowati et al., 2012a). The resulting output of the system: the spatial distribution map of *landcover*, *NDVI*, *β*, and *EF*.

Figure 2 is Form Display depicting the spatial distribution of *landcover* map of Bandung. In the form shown several features such as legend of seven types of land cover (residence, industry, open land, water body, plantation, paddy field, and forest), map scale, also info map will show that if we select a point on longitude 107.58 E and latitude 6.9 S with a white cursor denote a residence (Tursilowati et al., 2012a).

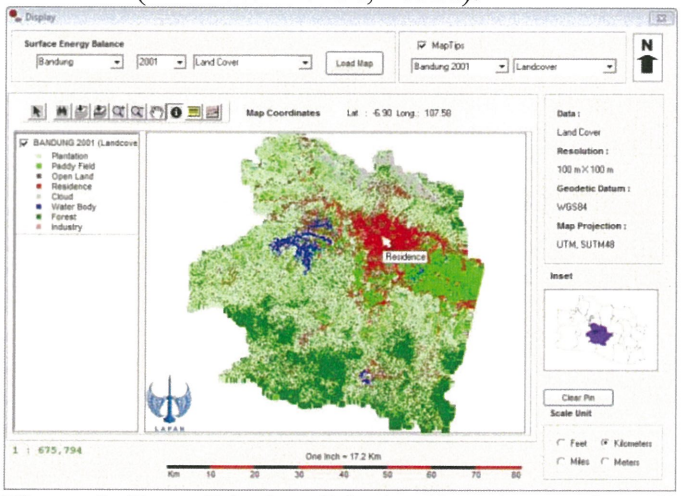

Figure 2. Form Display (Map) of Landcover (Tursilowati et al., 2012a)

Figure 3 is Form Display depicting the spatial distribution map of *NDVI* of Bandung. As in Figure 2, here also shown several features such as legend of value of *NDVI*, map scale, also info map will show that if we select a point on 107.58 °E, 6.9 °S with a white cursor denote residence with value of *NDVI* is 0.05. The high value of *NDVI* shown in the vegetation area (forest, plantation, and paddy field), otherwise low value of *NDVI* represent in the non vegetation area (residence, industry and open land).

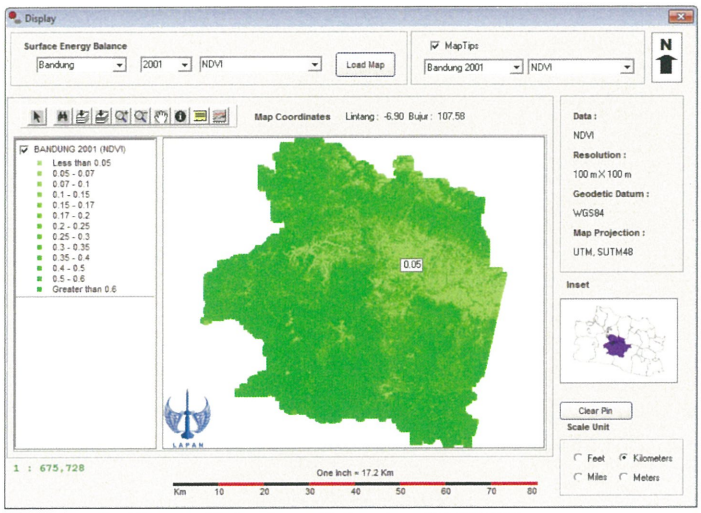

Figure 3. Form Display (Map) of *NDVI*

Figure 4 is form layer symbol that represent symbol properties for the β of Bandung. This form appears when we click the legend on the form display in Figure 2. β values are spatially depicted in Figure 4 with value from high to low are 4 in the urban areas (residence, industry and open land), 0.5 in the plantation, 0.33 in the forest, 0.25 in the paddy field, and 0.11 in the water body and cloud. This means that the urban area has potential drought is higher than other regions (Tursilowati et al., 2012b).

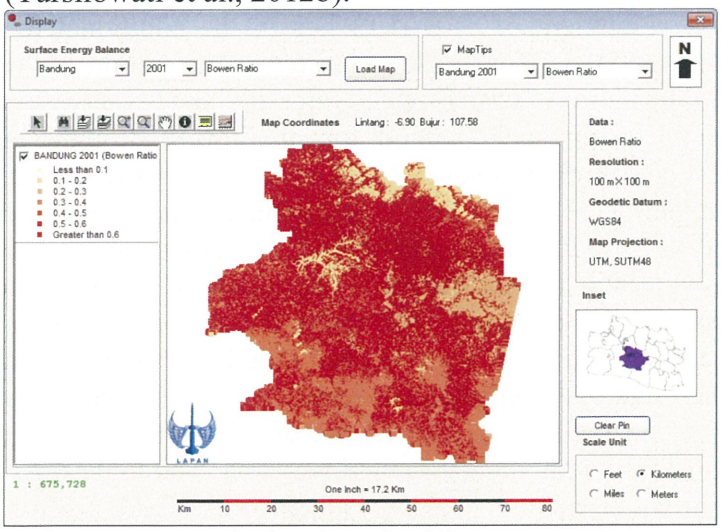

Figure 4. Form Display (Map) of β

Figure 5 is form layer symbol that represent symbol properties for the *EF* of Bandung. The opposite of the Bowen ratio, evaporative fraction is shown the level of wetness of a region.

Spatially seen that the use of the land settlements have high levels of evaporative fraction compared with vegetation and wet area. The highest *EF* value to lowest in Bandung area are 0.9 in water body and cloud, 0.8 in paddy field, 0.75 in forest, 0.67 in plantation, 0.2 in industry, open land and residence (Tursilowati et al., 2012b).

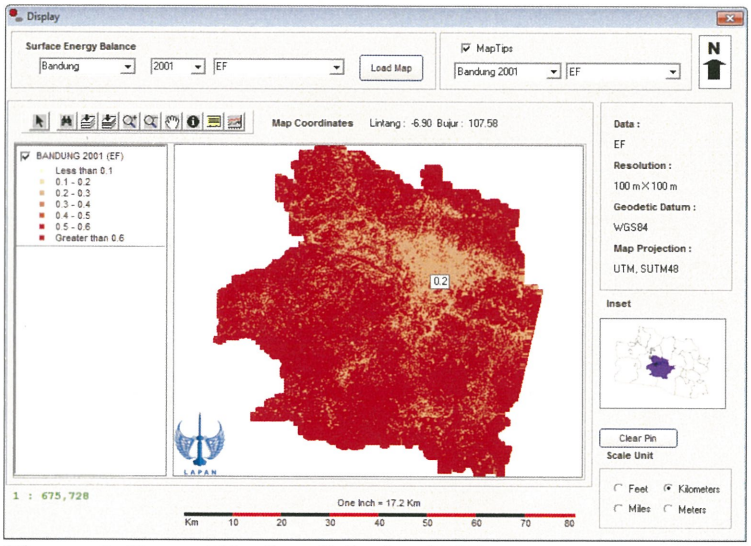

Figure 5. Form Display (Map) of *EF*

CONCLUSION

In this study has been successfully develop the Surface Energy Balance Interface Software (SEBALIS) using Visual Basic (VB) 6.0 program. This software can simplify the existing system and the formulation, facilitates data processing by reducing repetitive and complex tasks implemented with the ErMapper software. In the previous study the urban climate variables have been calculated in SEBALIS are surface temperature (*Ts*), air temperature (*Ta*), net radiation (*Rn*), soil heat flux (*G*), latent heat flux (*L*), sensible heat flux (*H*), and evapotranspiration (*Etp*) for each land cover in urban areas. The development of SEBALIS lies in the additional the formulation and estimation of urban climate variables (Normalized Difference Vegetation Index (*NDVI*), relative humidity (*RH*), comfortable index (*THI*), Bowen ratio (β), and evaporative fraction (*EF*)). This SEBALIS that developed has been applied for monitoring drought in Bandung. The output of SEBALIS represent distribution of seven types of land cover (residence, industry, open land, water body, plantation, paddy field, and forest) in Bandung. The high value of *NDVI* shown in the vegetation area (forest, plantation, and paddy field), otherwise low value of *NDVI* represent in the non vegetation area (residence, industry and open land). β values from high to low are 4 in the urban areas (residence, industry and open land), 0.5 in the plantation, 0.33 in the forest, 0.25 in the paddy field, and 0.11 in the water body and cloud. This means that the urban area has potential drought is higher than other regions. The opposite of the Bowen ratio, *EF* is shown the level of wetness of a region. Spatially seen that the use of the land settlements have high levels of evaporative fraction compared with vegetation and wet area. The highest *EF* value to lowest in Bandung area are 0.9 in water body and cloud, 0.8 in paddy field, 0.75 in forest, 0.67 in plantation, 0.2 in industry, open land and residence.

This software could be developed and further refined that can be used to process satellite data are integrated and practically appropriate to user needs.

REFERENCES

Datta, A. (2008). Process Engineering and Design Using Visual Basic, CRC Press, Taylor & Francis Group, Boca Raton, FL, USA.

Ford, J.L., JR. (2009). Microsoft visual Basic 2008 Express Programming for the absolute beginner, Course Technology a part of Cengage Learning, Boston, USA.

Foxall, J. (2010). Sams Teach Yourself: Visual Basic 2010 in 24 Hours, Pearson Education, Inc., Indiana, USA.

Halvorson, M. (2010). Microsoft Visual Basic 2010 – Step by Step, Microsoft Press, Washington, USA.

Hassan, A.B., Abolarin, M.S., Jimoh, O.H. (2006). The Application of Visual Basic Computer Programming language to Simulate Numerical Iterations, Leonardo Journal of Sciences, p. 125-136.

OECD. (2010). Cities and Climate Change. OECD Publishing.

Halvorson, M. (2010). Microsoft Visual Basic 2010: Step by Step, Microsoft Press, Washington, USA.

Julien, Y., Sobrino, J.A., Mattar, C., Ruescas, A.B., Mimenez-Munoz, J.C., Soria, G., Hidalgo, V., Atitar, M., Franch, B., and Cuenca, C. (2011), Temporal analysis of normalized difference vegetation index (NDVI) and land surface temperature (LST) parameters to detect changes in the Iberian land cover between 1981 and 2001, International Journal of Remote Sensing, 32:7, p. 2057-2068.

Niemeyer, S., and Vogt, J.V. (1999). Monitoring the Moisture Status of The Land Surface in Sicily Using an Energy Balance Approach, Space Application Institute. Joint Research Centre of The European Commission TP 441, I-21020 Ispra (VA), Italy.

Tursilowati, L., Sumantyo, J.T.S., Kuze, H., and Adiningsih, E.S. (2012a). Improved Data Processing of Landsat Satellite for Urban Climate Studies, Research Journal in Engineering and Applied Sciences (RJEAS), 1:4, p. 229-234.

Tursilowati, L., Sumantyo, J.T.S., Kuze, H., and Adiningsih, E.S. (2012b). Surface Energy Balance Method into Remote Sensing Application and GIS for Drought Monitoring in Bandung, Indonesia, Journal of Emerging Trends in Engineering and Applied Sciences (JETEAS), 3(3): 394-400.

Van Vliet, B., and Hendry, R. (2004). Modeling Financial Markets: Using Visual Basic.NET and Databases to Create Pricing, Trading, and Risk Management Models, Mc Graw Hill, USA.

Vogt J.V., Viau, A.A., Beaudin, I., Niemeyer, S., and Somma, F. (1998). Drought Monitoring From Space Using Empirical Indices and Physical Indicators. Proceedings International Symposium on "Satellite-Based Observation, Tunisia, 23-27 Nov., pp: 1-9.

Wan, Z., Wang, P., and Li, X. (2004). Using MODIS Land Surface Temperature and Normalized Difference Vegetation Index products for monitoring drought in the southern Great Plains, USA. Int. J. Remote Sensing, 25:1, p. 61-72.

Estimation of rice production based on LAI images by MODIS data in West Java

Chiharu Hongo[1], Gunardi Sigit[2], Koshi Yoshida[3], Masayasu Maki[4],
Koki Honma[5], Kazuo Oki[6], Hiroaki Shirakawa[7] and Takaaki Furukawa[8]

[1]Associate Professor, Center for Environmental Remote Sensing, Chiba University
1-33 Yayoi Cho, Inage Ku, Chiba shi, Chiba, Japan; Tel: +81-43-2903832;
E-mail: hongo@faculty.chiba-u.jp
[2]Officer, Regional Office of Food Crops Service West Jawa Province, Indonesia
E-mail:gunsigit@yahoo.com
[3]Associate Professor, College of Agriculture, Ibaraki University
E-mail: ayoshida@mx.ibaraki.ac.jp
[4]Assistant Professor, Urban and Environmental Engineering, Kyoto University
E-mail: maki@envinfo.uee.kyoto-u.ac.jp
[5]Lecturer, Graduate School of Agriculture, Kyoto University
E-mail: homma@kais.kyoto-u.ac.jp
[6]Associate Professor, Institute of Industrial Science, University of Tokyo
E-mail: kazu@iis.u-tokyo.ac.jp
[7]Associate professor, Graduate School of Environmental Studies, Nagoya University
E-mail: hiroaki.shirakawa@gmail.com
[8]Technical assistant, Center of Environmental Remote Sensing, Chiba University
E-mail: furukawa@chiba-u.jp

KEY WORDS: rice production, MODIS, LAI, Indonesia

ABSTRACT: Rice is one of the most important agricultural crops in Indonesia and also a primary food resource for more than three billion people in the world. However, because of a worldwide serious problem on food shortages due to climate change, it is necessary to evaluate the potential of rice production and estimate rice yield in Indonesia. Cianjur, a study area, is located in the West Java, Indonesia, at 7°03' S latitude and 106°60' E longitude. This area is famous for the rice production and is one of areas where the decrease of agricultural productivity is much concerned. Satellite remote sensing has been used widely and extensively and is now recognized as a powerful and effective tool for monitoring rice growth and the rice production.

In this study, images of leaf area index (LAI) by Moderate Resolution Imaging Spectroradiometer (MODIS) acquired from 2003 to 2008 were used to evaluate the rice growth and also construct an equation of the rice yield per unit of a paddy field in Cianjur. As a result, it is suggested that a weekly change of LAI indicates two times of rice production in a year, and the average LAI of the 2 times production is correlated with the rice yield per unit ($r=0.527$, $p<0.05$). Thus, this indicates that the rice yield per unit can be estimated through the following equation: $y = 0.632479x + 3.049962$, where y is the rice yield per unit size of a paddy field and x is the average LAI of 2 times production, and the standard error of estimation is 0.77.

1. INTRODUCTION

The environmental conservation and food production is one of the most critical issues that we have to make best efforts to solve from now on in every country. The remote sensing agricultural research, especially related to rice production and rice field management is very important for Asian countries, because rice is the staple food for the people and, on the other side, Asian agriculture frequently suffers from heavy losses caused by meteorological events. Considering these matters, it is a good idea to develop an efficient rice cultivation support system based on a concept of the precision agriculture which can effectively increase the rice production and also realize the environmental conservation.

In this study, to assess the feasibility of the estimating rice yield using remotely sensed data, the investigation of the relation between annual rice production from the agricultural statistical data and cumulative LAI derived from MODIS LAI 8days composite data was carried out in west Jawa, Indonesia.

2. METHOD

2.1 Study site

The study was conducted in 6 sub-districts (Kecamatan Cilaku, Sukaluyu, Bojongpicung, Ciranjang, Karangtengah, and Cianjur) located in the north east of Kabupaten Cinajur, west Jawa, Indonesia (longitude 106°21'E-107° 22'E, latitude 6°42S-7°25'S) (Fig. 1).

2.2 Data for analysis

(1) MODIS/Terra＋Aqua Leaf Area Index/
FPAR8-day L4 Global 1km SIN Grid V005 (2003-2008) (46 composite data)
(2) Aqua/Terra MODIS and SPOT VEGETATION rice paddy map at IIS, U-Tokyo, Japan (1999-2007, 1km resolution)
(3) Administrative boundary GIS data
(4) Agricultural statistics data from 2003 to 2008 which was published by BPS

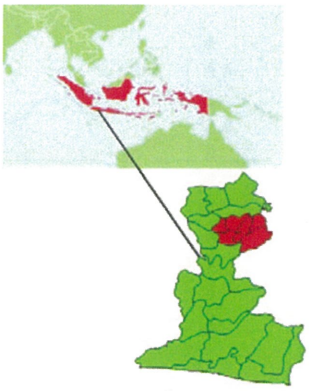

Fig. 1 Study site

2.3 Procedure

Figure 2 show that the procedure of data analysis.

First, the leaf area index composite data (LAI), the SPOT data and the ASTER data were rectified using the administrative boundary GIS data by the nearest neighbor resampling algorithm using the selected ground control points. Secondly, a supervised classification was applied to these rectified images to distinguish the paddy fields, and the mask file of paddy fields was created. Data on cumulative LAI value of paddy fields from October, 2001 to September, 2008 were calculated, and the data was added to the GIS of administrative boundary. Finally, the tabulate area analysis was executed using the LAI data and the agricultural statistic data to analyze the seasonal trend of LAI and the relationship between the annual rice production and LAI.

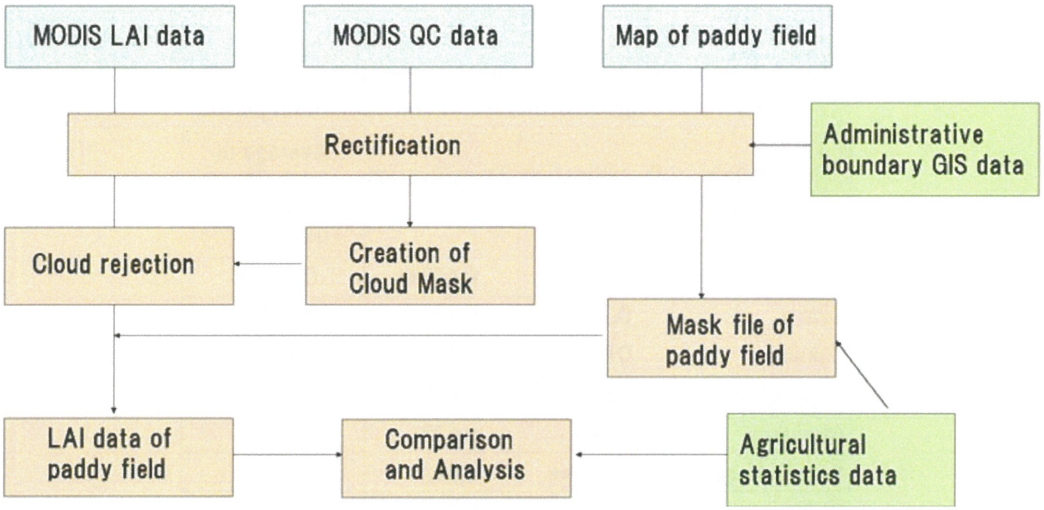

Fig.2 Procedure

3. RESULTS AND DISCUSSION

The seasonal trend of averaged LAI in all sub-districts (Kecamatan) is shown in Figure 3. There are two minimum values in a year. These seasons correspond to the harvesting season of rice crop around the test site. Table 1 shows the relationship between annual rice production per unit and the average LAI of 1st and 2nd cultivation period. The result shows significant positive correlation between the annual rice production and the cumulative LAI of the first cultivation period and the second cultivation period($n=36$)($p<0.01$ and $p<0.05$). The correlation coefficient of the first cultivation period is higher than the second cultivation period. As a result, it is suggested that a weekly change of LAI indicates two times of rice production in a year, and the average LAI of the 2 times production is correlated with the rice yield per unit ($r=0.527$, $p<0.05$).

Figure 4 shows the relationship between the average LAI and the annual rice production per unit. The rice yield per unit can be estimated through the following equation:

$y = 0.632479x + 3.049962$

where y is the rice yield per unit size of a paddy field and x is the average LAI of 2 times production
The standard error of estimation is 0.77.

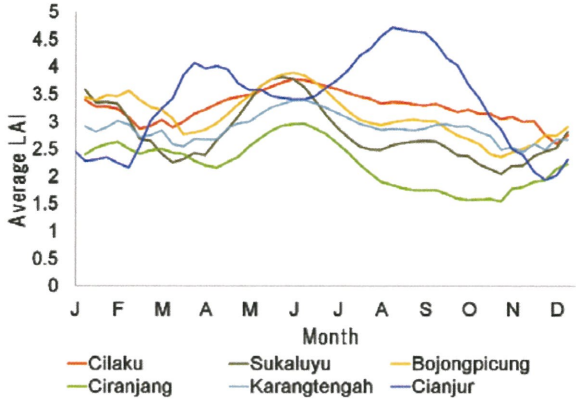

Fig. 3 Seasonal trend of averaged LAI

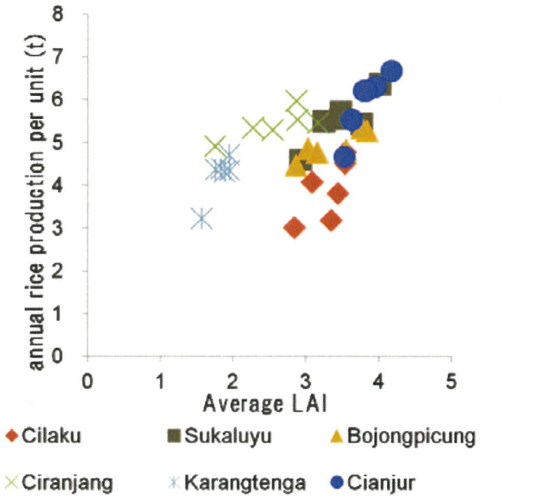

Fig. 4 Relationship between the average LAI and the annual rice production

Table 1 Relationship between annual rice production per unit and the average LAI of 1st and 2nd cultivation period

sub-districts (Kecamatan)	1st cultivation period	2nd cultivation period	Average of 1st & 2nd cultivation period
All sub-districts	0.576**	0.449**	0.527**
Cilaku	0.707	0.466	0.693
Sukaluyu	0.823*	0.710	0.872*
Bojoingpicung	0.804	0.893*	0.891
Ciranjang	0.788	0.673	0.753
Karangtengah	0.949**	0.649	0.883*
Cianjur	0.867*	0.764	0.901**

(* :p<0.05 ** :p<0.01)

4. CONCLUSION

It was possible to estimate the annual rice production of 2008 using the average LAI of 1st and 2nd cultivation period from 2003 to 2007. This study indicates that the cumulative LAI of remotely sensed data is applicable to the estimation of rice production amount in wide areas, and the creation of each estimation equation for the irrigated paddy fields and the rain fed paddy fields will contribute to improvement of the estimation accuracy of the annual rice production.

ACKNOWLEDGEMENT

This research is supported by Environment Research and Technology Development Fund, Ministry of the Environment, Japan (The assignment number: E1104).

AN OBJECT-BASED APPROACH FOR TROPICAL FOREST CLASSIFICATION USING ALOS PALSAR 50M ORTHORECTIFIED MOSAIC DATA

-----PART 1. COMPARISON OF DIFFERENT METHODS FOR SLOPE CORRECTION

Mi Lan[1], Nguyen Thanh Hoan[2] and Ryutaro Tateishi[3]

[1]Graduate student, Center for Environmental Remote Sensing (CERes), Chiba University,
1-33 Yayoi Cho, Inage Ku, Chiba Shi, Chiba, Japan; Tel: + 81-43-290-2964;
E-mail: miran@graduate.chiba-u.jp

[2]Researcher, Center for Environmental Remote Sensing (CERes), Chiba University,
1-33 Yayoi Cho, Inage Ku, Chiba Shi, Chiba, Japan; Tel: + 81-43-290-2964;
E-mail: hoanrs@gmail.com

[3]Professor, Center for Environmental Remote Sensing (CERes), Chiba University,
1-33 Yayoi Cho, Inage Ku, Chiba Shi, Chiba, Japan; Tel: + 81-43-290-2964;
E-mail: tateishi@faculty.chiba--u.jp

KEY WORDS: PALSAR mosaic, slope correction, tropical forest

ABSTRACT: Because of the capacity of observing land cover information in any weather, microwave sensor is good at monitoring forest change especially in the tropical area. In this study, Japanese ALOS PALSAR 50m orthorectified mosaic data will be used for extracting the distribution of forest in Kalimantan as a free product. However, we have to consider a big problem caused by the effects of terrain slope. Therefore, we compared two existing slope correction methods for PALSAR 50m mosaic data, and applied the better one to complete the terrain slope calibration in this paper.

1. INTRODUCTION

Recently, more and more researchers start to use synthetic aperture radar imagery to extract forest distribution because of the advantage that it can observe the ground information in day and night, and will not be affected by the cloud. Since Advanced Land Observing Satellite was sent by Japan in 2006, PALSAR has been applying for mapping forest and non-forest area over global as a new full polarization radar. However, for improving the accuracy of classification result, we have to make terrain slope calibration which always be seen as a common problem of SAR image at first.

PALSAR 50m orthorectified mosaic dataset is a free calibrated product generated by three agencies of JAXA, JRC, and JPL to cover the global continents (Shimada, 2008). But for keeping the characteristics of topography, slope correction had not be done in this dataset (Shimada, 2008). To this aim, we choose Kalimatan (Upper Left: 108d29'54.0357"E, 7d30'06.2023"N, Lower Right: 119d30'04.5082"E, 4d52'00.2057"S) as study area, and compared two existing theoretical approaches which developed through the variation of local incidence angle (Rokhmatuloh, 2012 and Akatsuka, 2009) only for ALOS PALSAR 50m orthorectified mosaic data.

2. Methodology

2.1 Data Acquisition

ALOS PALSAR 50m orthorectified mosaic dataset--- HH polarization and HV polarization are used as main data in this study. For calibrating geometric problem and calculating local incidence angle, we used SRTM 90m as DEM data, and Landset TM/ ETM images as the database.

2.2 Study flow

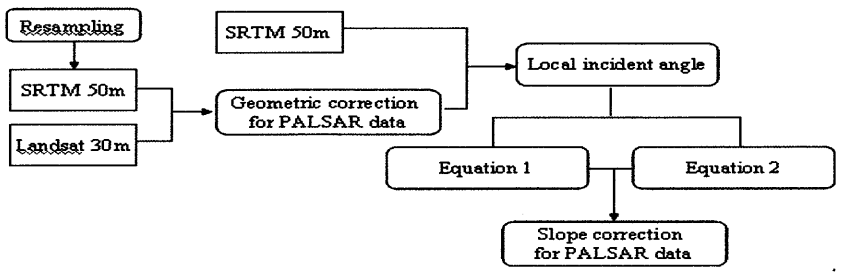

Figure 1. Flow chart of this study

2.3 Compare with existing slope correction formulas

2.3.1 Local incidence angle and equations

Local incidence angle is calculated with aspect image and slope image for each pixel from SRTM DEM data as the first parameter. (T. Castel. Et al.)

$$\cos\theta_{loc} = \cos\alpha\cos\theta - \sin\alpha\sin\theta\cos(\beta - \Phi) \quad \text{(Eq. } \theta\text{)}$$

In this equation, local incidence angle θ loc is given by its incidence angle θ (34.3℃), viewing azimuth angle Φ (188.16℃), local slope α and aspect angle β.

Next, using calculated local incidence angle to apply for two different existing slope correction theoretical methods according to calibrating the backscatter coefficient of the PALSAR image.

$$Rc = R/(\cos^2\theta_{loc} - \cos^2 34.3)) \quad \text{(Eq. 1) [4]}$$

R is the original SAR image value, Rc is the value of corrected SAR image.

$$\sigma\,corr = \sigma * \sin(loc)/\sin(Iref) \quad \text{(Eq. 2) [3]}$$

σ is original backscatter coefficient of PALSAR image, σ corr is the backscatter coefficient after slope correction. Iref is the radar incidence angle at the center of the image which is 34.3° for PALSAR data used in this formula. (Rokhmatuloh, 2012)

2.3.2 Results of the analysis made from different landforms

Figure 2.~Figure 4. show the analysis results made from the training data took from flat area, black area and bright area but the same type of forest on Google Earth.

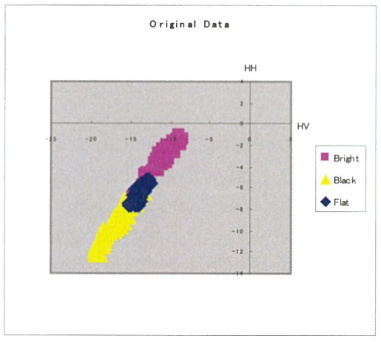

Figure 2. Analysis from original data

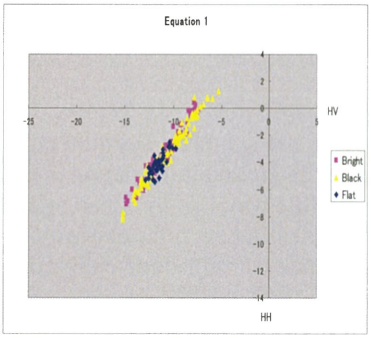

Figure 3. Analysis from the corrected result of Eq.1.

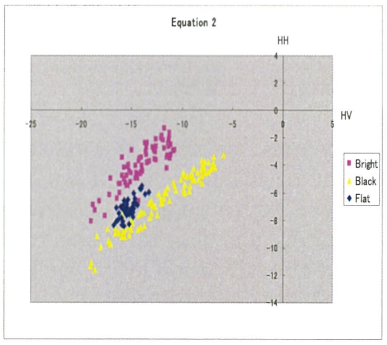

Figure 4. Analysis from the corrected result of Eq.2.

3. Conclusions

In this study, for getting an accuracy forest map, we compared two existing slope calibration approaches before classification. After analysis from different topography but same type of training data, we can know the Eq.1. is better for correcting slope problem of PALSAR 50m orthoretified mosaic data. In addition, geometric correction also should be applied to this dataset.

References from Journals:

[1] Shimada, M., Isoguchi, O., Rosenqvist, A., 2008. PALSAR CALVAL AND GENERATION OF THE CONTINENT SCALE MOSAIC PRODUCTS FOR KYOTO AND CARBON PROJECTS, IEEE, pp. I-17- I-20.

[2] Shimada, M., Isoguchi, O., Rosenqvist, A., 2008. Continent scale PALSAR mosaic products for Kyoto and Carbon Project. IEICE Technical Report, pp.81-85.

[3] Rokhmatuloh, Hendri Murfi an Ryutaro Tateishi, 2012, Support Vector Maching (SVM) for classification of forest and non forest derived from ALOS PALSAR data. Report and Proceedings of ALOS Application and Verification Project in Indonesia. pp. 18-25.

[4] Akatsuka, S., Takeuchi, W., Rakwatin, P. and Sawada, H., 2009. Evaluation of slope correction effects on ALOS PALSAR mosaic data set. *Proceeding of Japan Society of Photogrammetry and Remote Sensing*. pp. 151-154.

[5] T.Castel, A. Beaudoin, N. Stach, N. Stussi, T. Le Toan & P. Durand, 2001, Sensitivity of space-borne SAR data to forest parameters over sloping terrain. Theory and experiment, International Journal of Remote Sensing, pp. 2351-2376.

The improvement of the accuracy of global landcover map by using existing global land cover maps

Naijia Zhang[1] and Ryutaro Tateishi[2]

[1]Graduate student, Graduate School of Engineering, Chiba University,
1-33 Yayoi Cho, Inage Ku, Chiba Shi, Chiba, Japan; Tel: + 81-43-2902964;
E-mail: Z_N_J@graduate.chiba-u.jp

[2]Professor, Graduate School of Advanced Integration Science, Chiba University
1-33 Yayoi Cho, Inage Ku, Chiba Shi, Chiba, Japan; Tel: + 81-43-2903850;
E-mail: tateishi@faculty.chiba-u.jp

KEY WORDS: GLCNMO, global land cover

ABSTRACT: Many investigators need and use global land cover maps for a wide variety of purposes. But, a global land cover project always costs a long time; and its accuracy is not so high. As a result, comparison of then different land cover maps is difficult and information about their relative utility is limited.

1. Background

A global land cover project always costs a long time; and its accuracy is not so high. As a result, comparison of then different land cover maps is difficult and information about their relative utility is limited.
Global Land Cover by National Mapping Organizations (GLCNMO) was produced in 2008 (http://www.cr.chiba-u.jp/databaseGGI.htm). It has 20 land cover classes defined using the Land Cover Classification System (LCCS). Until now, six global land cover projects have been produced. (IGBP-DISCover, UMd, MODIS LC, GLC2000 and GLOBCOVER)
This study aimed to extract the reliable areas from the four existing global land cover maps (MODIS LC, GLC2000, GLCNMO and GLOBCOVER). The data users and producers may use this reliable area map to analyze existing global land cover maps as a reference data. For producers, who can conveniently use the highly reliable areas to collect training data or some other findings; and may pay more attention to the lowly reliable areas in the future work.

2. Methodology

The existing global land cover products that based on different remote sensing data have different legends. So, the first step is to reconcile the different legends (Table 1). Certainly, the combination is not the only choice but mainly based on the classification system that GLCNMO has.

Table 1: The seventeen aggregated classes for the four land cover products

New legends	GLCNMO	MODIS LC	GLC2000	GLOBCOVER
1. Broadleaf Evergreen Forest	1	2	1	40
2. Broadleaf Deciduous Forest	2	4	2	50
3. Needleleaf Evergeen Forest	3	1	4	70
4. Needleleaf Deciduous Forest	4	3	5	N/A
5. Mixed Forest	5	5	6	100
6. Tree Open	6	8	3	60,90
7. Shrub	7	6,7	11,12	110,120,130
8. Herbaceous, single layer	8	10	13	140
9. Herbaceous with sparse tree / shrub	9	9		
10. Sparse Vegetation	10	N/A	14	150
11. Cropland	11,12	12	16	11,14
12. Cropland / other vegetation mosaic	13	14	17,18	20,30
13. Mangrove	14	N/A	8	170
14. Wetland	15	11	7,15	160,180
15. Bare area	16,17	16	19	200
16. Urban	18	13	22	190
17. Snow/Ice	19	15	21	220
18. Water Bodies	20	17	20	210

Than, The information provided by each of these individual maps by considering four levels of agreement is synthesized as follows:

Level 1: No agreement in each dataset. (1-1-1-1)

Level 2: The first two datasets are in agreement and the other two are also in agreement, but for different aggregated classes; only two of the four datasets are in agreement. (2-2 or 2-1-1)

Level 3: Agreement between three datasets. (3-1)

Level 4: Agreement between all the four datasets. (4)

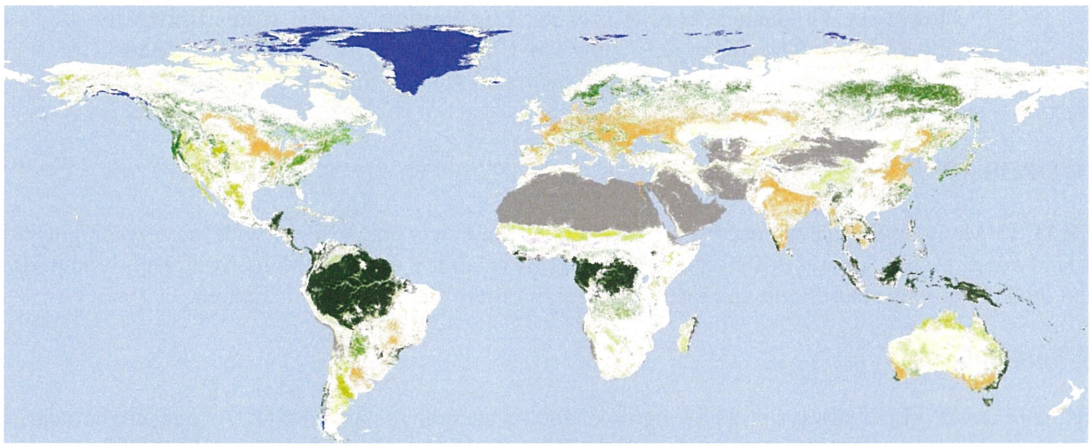

1	Broadleaf evergreen forest
2	Broadleaf deciduous forest
3	Needleleaf evergreen forest
4	Needleleaf deciduous forest
5	Mixed forest
6	Tree open
7	Shrub
8	Herbaceous
9	Herbaceous with sparse tree / shrub

10	Sparse vegetation
11	Cropland
12	Cropland / other vegetation mosaic
13	Mangrove
14	Wetland
15	Bare Area,consolidated(gravel,rock)
16	Urban
17	Snow / ice
18	Water bodies

Fig 1 Reliable area extracted from four land cover products (MODIS LC, GLC200, GLCNMO, GLOBCOVER)

We treat the parts of Level 3 and Level 4 as the highly reliable part, called reliable area (Fig 1).

3. Conclusions and analyses

We validated the reliable area (Fig 1). Totally, about 500 random validation points have been picked between 17 classes (except class 18: water). As a result, the total accuracy of the reliable area is above 90%.

This study just points out integrated information of the existing global land cover maps. The ultimate goal is just to help the next land cover project plan as a reference.

References

[1] M.Herold, R.Hubald, and A.Di Gregororio, 2009. Translating and evaluating land cover legends using the UN Land Cover Classification System (LCCS), GOFC-GOLD Report No. 43, June 2009.

[2] Global Map Version 1.3 Specifiations, Revised at 14th ISCGM meeting Cambridge, 14 July 2007.

Land over change detection using multi-temporal MODIS data

Kalibinuer Yishamiding 1[*a] and Ryutaro Tateishi 2[b]

a Graduate student, Graduate School of Science, Chiba University,
1-33 Yayoi Cho, Inage Ku, Chiba Shi, Chiba, Japan; Tel: + 81-43-2902964;
E-mail: kalibinuer23@gmail.com

b Professor, Center for Environmental remote sensing, Chiba University
1-33 Yayoi Cho, Inage Ku, Chiba Shi, Chiba, Japan; Tel: + 81-43-2903850;
E-mail: tateishi@faculty.chiba-u.jp

KEY WORDS: Land cover, NDVI image differencing, Change vector analysis, Deforestation

ABSTRACT: Monitoring the location and distributions of land cover changes is important for environmental protection and management, its change is a key to many diverse applications such as forestry, hydrology, and agriculture. Continues time series MODIS data gives major advancement for land cover related project over large geographic region. This study focuses on the use of coarse spatial resolution MODIS time series data (16-day composite) for Eurasia land cover change detection between the year 2003 and 2008, aim to serve an alarm where rapid land cover conversation can be analyzed with higher resolution remote sensing data and find out better change detection method which suitable for global project. In this study three change detection methods were evaluated: Normalized difference vegetation index image differencing (NDVI), Change vector analysis using Tasseled cap transformation (TCT), Change vector analysis using NDVI and Bare soil index (BI).To setting the threshold for possible changed area in each change detection method several scene from Landsat image and Google earth was used as reference data. Three methods compared each other by the performance on different type of land cover change extraction visually. As a result NDVI image differencing method is suitable for detection of forest clear cut and change vector analysis is good for the detection of burnt area and recovered area. Land cover change detection map was created which shows the follow changes: (1)Tropical forest transformation to agriculture land was mainly detected in south east Asia region;(2)Burnt area and vegetation recovered area were detected in north part of Eurasia;(3)Large vegetation decreasing was detected in middle east region which caused by the changing of the weather condition.

1. INTRODUCTION

Land cover change monitoring is an important field in global environmental change research. Remote sensing is a valuable data source from which land-use/land-cover change information can be extracted efficiently. Land cover change detection is the process of identifying differences of an object or phenomenon by observing it at different times (Singh, 1989). Timely and accurate change detection of Earth's surface features provides the foundation for better understanding relationships and interactions between human and natural phenomena to better manage and use resources (D.lu, 2004). Essential part of land cover change detection is using multi-temporal data sets and applies digital change detection analysis. However to choose a suitable digital change detection method for a specific area is very difficult. Previous land cover change detection is mainly based on high resolution remote sensing data for regional scale change detection. Numerous authors have described good methods for regional land cover change detection with high accuracy by using high resolution data. However, at continental or global scale high resolution huge amount of data that makes it difficult and expensive to implement analysis. Course resolution data such as MODIS is often useful and more practicable for many types of change detection. How to choose a suitable method is still problematic in global land cover change detection with course resolution data. Change detection by using course spatial resolution data is need more ancillary data and the detected areas are mostly sensitive to annual climate fluctuation and just one type of change detection method may not proper for different type of change. Therefore, the objective of this study is to choose an efficient method for global land cover change detection using MODIS data. The first experiment will be the land cover change detection between the year 2003 and 2008 on Eurasia continent with three type of change detection method.

2. STUDY SITE

The study area for this research is Eurasia continent, covers roughly between 9° and 80° latitude and between 12 ° and 180° longitude. The major environmental problems in Eurasia region are rapid land cover change along with forest fire, tropical forest deforestation by human activity, coastal zone damage. Significant changes in land

cover in Eurasia, coupled with climate change, will likely affect a number of important sectors, such as forestry, agricultural systems and the coastal zone, and may have significant societal impacts.

3. DATA

(1)Global MODIS 2003(spatial resolution1km) and MODIS 2008(spatial resolution 500m) 16-day composite time series dataset, cloud free 16-day composite with 7spectral bands. These datasets were processed by the center for environmental remote sensing (CEReS) at Chiba University. (2) MODIS Water mask (spatial resolution 250m) from University of Maryland GLCF (Global Land Cover Facility) is used to exclude false change information from the result image which caused by open water body. (3) Landsat data from University of Maryland GLCF (Global Land Cover Facility) is used as reference data.(4)MODIS burned area monthly 500m product is used to visually evaluate the result of detected burned and recovered area.

4. CHANGE DETECTION METHOD

Remote sensing change detection techniques can be classified in two main categories: pre-classification and post-classification change methods. Pre-classification methods can further be characterized as being spectral or phenology based. Originally, the post-classification approach was considered to be the most reliable method because it can demonstrate the type of the change directly. Factors that limit the application of post-classification change detection techniques are the cost, consistency, time consuming, accuracy of the classified image. Numerous pre-classification change detection approaches have been developed and refined to provide optimal performance over the greatest possible range of ecosystem conditions. These semi-automated digital data processing approaches include image-based composite analysis, and principal components analysis (PCA). The most commonly applied data transformations applied include band rationing, NDVI, and the tasseled-cap transformation. Recent techniques have been applied that can interpret data transformation results using change vector analysis (CVA) to indicate the magnitude and nature of change. Determination of change direction is also important in selecting appropriate change detection techniques. Some techniques such as image differencing can only provide change/non-change information, while some techniques such as post classification comparison can provide a complete matrix of change directions, but for the global scale land cover change it is hard to use post classification method because of the low accuracy of the classified image. In this research, Normalized difference vegetation index image differencing (NDVI), Change vector analysis with tasseled cap transformation (TCT), Change vector analysis with NDVI and Bare soil index (BI) were applied to see the performance on large area change detection.

4.1 Normalized vegetation index image differencing

NDVI is an effective normalized index which can enhance the difference among spectral features and suppress topographic and shade effects. Therefore, the difference of NDVI between two dates has the potential to detect land cover change (Lu et al., 2005).Due to its simplicity and efficiency, this method is widely used in change detection analysis. In this study first step, the time series NDVI data is extracted from MODIS 2003 and 2008 data red band (band1) and near infrared band (band2) by the following equation:

$$NDVI= (band2-band1)/(band2+band1) \quad (1)$$

In second step, Maximum value composite (MVC) NDVI image is produced from each data set, difference image was created by simple subtraction between two years MVC NDVI image pixel by pixel. In differencing image, most of the pixels have the NDVI value of 0 or near to 0; these pixels are considered as unchanged pixel. There are also some pixels exist which have the value of greater or smaller than 0, changes may occurred in such places. Threshold for changed and unchanged pixel could be decided by Landsat data and Google earth historical data.

4.2 Change vector analysis with TCT transformation

The first step of the CVA method was to apply Tasseled Cap transformation, which generates the components Greenness, Brightness and wetness. Multi temporal data is very useful for seasonal change analyses, but a large number of spectral bands are an obstacle for precise analysis of the land cover change between two dates. The tasseled cap transformation provides a mechanism for data volume reduction with minimum information loss, and its spectral features can be directly associated with the important physical parameters of the land surface. The greenness band associated with the amount and vigor of vegetation, and Brightness, associated with variations of soil reflectance. The position variation of the same pixel during different data determines the magnitude and direction of the spectral change vectors. By setting different threshold, different type of changed area could be extract. Tasseled Cap transformation done for each period by using the coefficients for MODIS data (Lobser, 2007).

To minimize change detection error introduced by seasonal differences, maximum greenness and brightness value were extracted. Change magnitude and angle is calculated by following equation:

$$M = \sqrt{(Gr_{2008} - Gr_{2003})^2 + (Br_{2008} - Br_{2003})^2} \tag{2}$$

$$\alpha = \arctan\left(\frac{Gr_{2008} - Gr_{2003}}{Br_{2008} - Br_{2003}}\right) \tag{3}$$

M: The magnitude of change vector (Euclidean distance)
α : The direction of change vector
Gr_{2003}, Gr_{2008}, Br_{2003} , Br_{2008} are the greenness and brightness for the year 2003 and 2008.

4.3 Change vector using bare soil index (BI)

NDVI and BI index are usually used in CVA method to stress the vegetable class and bare soil class that are the main classes of land covers of natural surface. BI is calculated from MODIS data red(band1), near-infrared (band2), blue regions(band3) short wave infrared(band6), of period 13(July 12th).

$$BI = \frac{(band1 + band6) - (band2 + band3)}{(band1 + band6) + (band2 + band3)} \tag{4}$$

The calculation of magnitude and direction of change vector are the same way as the formula (2), (3).

6. DISCUSSION AND CONCLUSION

(1) NDVI Image differencing method was simple and straightforward and interpreting the results were easy. However, this technique will enhance random noise and to set precise threshold for change and no change area needs more reference data. For differencing image, by visually interpretation of Landsat image, the pixel which have the differencing NDVI value bigger than +0.16 extracted as positive changed area, and smaller than -0.12 extracted as negative change area. As a result, main vegetation negative change area detected from the tropical forest region which is the result of deforestation. At the same time, large negative change area detected in Middle East arid region which is caused by the climatic factor. To separate the vegetation change which is the result of climatic factor from other vegetation change, wetness band (represent for interrelationship of soil and vegetation moisture) from TCT is used in this step. Water body change is also detected in result image, but considering of the variable nature of the water bodies, MODIS water mask product was used to mask the water area. This method has poor quality while detecting the forest burned area and recovering area.

(2) Change Vector Analysis technique demonstrate the capacity to detect and stratify different types of changes. By giving proper threshold to the magnitude and direction of change vector image, can separately extract the vegetation burned area, vegetation recovered area and deforestation. In this method burned area and vegetation recovered area detected in north part of Eurasia very clearly. But in the case of extracting deforestation area the result is not as good as the NDVI image differencing method.

(3) Change vector analysis with NDVI and BI method has the same result as NDVI method while detecting deforestation, but over performed while detecting burned area and performed poor on detecting vegetation recovered area.

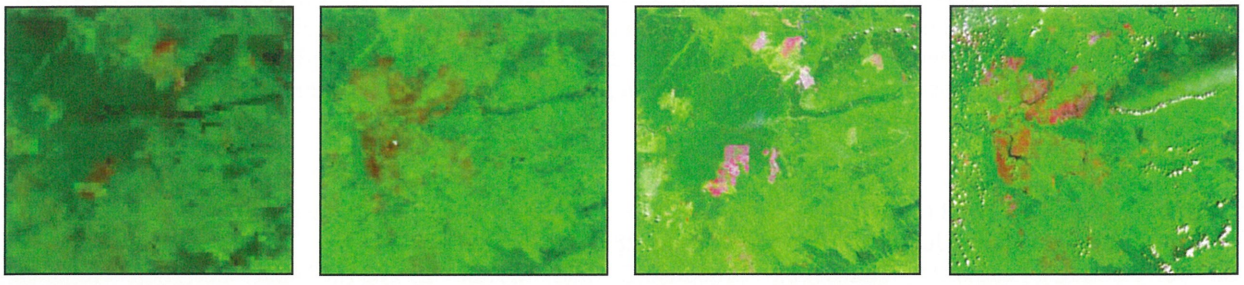

(a) (b) (c) (d)

Fig.1. (a)and (b) are MODIS 500m images acquired on July 12,2003 and July 11,2008 (RGB 6,2,1 band).(c) and (d) are Land sat ETM+ images acquired on June 22,2004 and Oct 23,2008(RGB 7,4,3 band).The pink areas in both images are the areas where the conversion of tropical forest to agriculture land is happen.

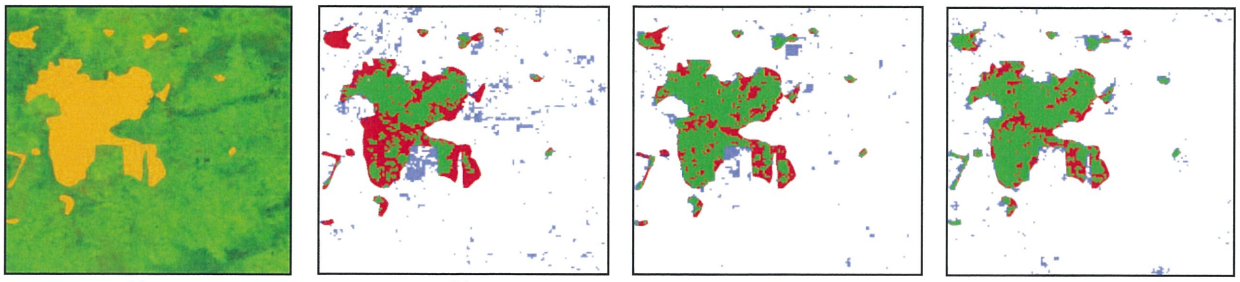

(a) (b) (c) (d)

Fig.2. (a) Reference data of deforested area extracted by comparing two land sat ETM+ image visually showed in orange color; (b)Result of the NDVI image differencing method); (c) Result of the change vector analysis by TCT method; (d).Result of the change vector with NDVI and BI method. The green color indicates the deforested area in result image mach with the reference image. Red color indicated the area which did not extracted, blue color indicate the area that over extracted comparing to the reference image

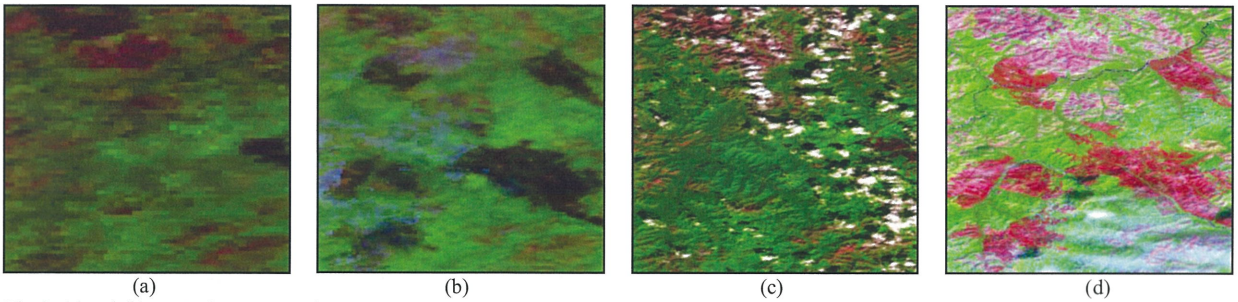

(a) (b) (c) (d)

Fig.3. (a)and (b) are MODIS 500m images acquired on July 12,2003 and July 11,2008 (RGB 6,2,1bands), the dark purple areas in the image are the areas burned by fire .(c) and (d) are Land sat ETM+ image acquired on Aug 23,2003 and Aug 23,2008(RGB 7,4,3 bands).The pink areas in 2008 image is the burned area.

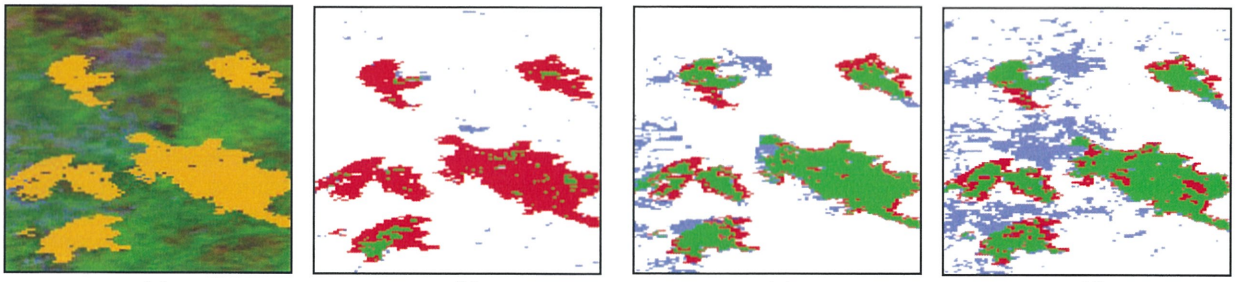

(a) (b) (c) (d)

Fig.4. (a) MODIS burned area product showed in orange color; (b)Result of the NDVI image differencing method); (c) Result of the change vector analysis with TCT method; (d).Result of the change vector with NDVI and BI method. The green color indicates the burned area in result image mach with the reference image. Red color indicated the area which did not extracted, blue color indicate the area that over extracted comparing to the reference image.

Each change detection method has its advantages and limitations while extracting different land cover change. The land cover change such as the conversion of forest to agriculture land can be extracted by using NDVI image differencing method or change vector analysis with NDVI and BI method. The area of vegetation decreasing caused by forest fire and vegetation recovering after the fire can be extracted by change vector analysis with TCT. For both change detection method accuracy assessment is an important and difficult part. Especially in large area land cover change detection study, it is difficult to evaluate the result quantitatively due to the difficulty of acquisition a large amount of historical data. Future work will be concentrated on the validation of the change detection result. For a given research purpose, when the remotely sensed data and study areas are identified, selection of an appropriate change detection method has considerable significance in producing a high-quality change detection product.

References

Lobser,s.E and cohen, W.B.(2007),MODIS tasseled cap: land cover characteristics expressed through transformed MODIS data. International Journal of Remote Sensing, 28:22,5079-5101

Lu corresponding author,D., Mausel,P., Brondizio,E. and Moran, E.(2004),Change detection techniques. International Journal of Remote Sensing 25:12, 2365–2401.

Singh.A., 1989, Digital change detection techniques using remotely sensed data. International Journal of Remote Sensing 10, 989–1003.

A NEW GLOBAL URBAN MAP USING MULTI SOURCE GEOSPATIAL DATA

Dong Xuan Phong[*1] , Ryutaro Tateishi[2] , Nguyen Thanh Hoan[3] and Toshiyuki Kobayashi[4]

[1,4]Graduate student, Graduate School of Science, Chiba University,
1-33 Yayoi Cho, Inage Ku, Chiba Shi, Chiba, Japan; Tel: + 81-43-290-2964;
[1]E-mail: dongxuanphong@chiba-u.jp, dxpvn@yahoo.co.jp
[4]E-mail: kobayashit@graduate.chiba-u.jp

[2]Professor, Center for Environmental Remote Sensing (CEReS), Chiba University
1-33 Yayoi Cho, Inage Ku, Chiba Shi, Chiba, Japan; Tel: + 81-43-290-3860;
E-mail: tateishi@faculty.chiba-u.jp

[3]Doctor, Center for Environmental Remote Sensing (CEReS), Chiba University
1-33 Yayoi Cho, Inage Ku, Chiba Shi, Chiba, Japan; Tel: + 81-43-290-2964;
E-mail: hoanrs@gmail.com

KEY WORDS: New Global Urban Map, Comparison, Mapping, GLCNMO 2008

ABSTRACT: Urban Area is an important class of Global Land Use/Land Cover Map. Global Urban Mapping is always difficult because of the different definition of "urban area" in different countries. In remote sensing, "urban area" is often best defined as population density distribution, as percentage of impervious surface, nighttime light. Green fields and water bodies (such as a big park or a golf course) were not considered as urban. In this study, urban area was mapped using multi-source geospatial data of 2008 year such as Population Distribution and Density, DMSP-OLS (The Defense Meteorological Satellite Program's Operational Linescan System) nighttime lights, MODIS data and Estimate the density of constructed Impervious Surface Area (EstISA) data of 2010 year. Information from all data sources was combined to create a final map of urban area and compared with fine resolution Landsat ETM+ and Google Earth image. The Global Urban Map 2008 produced was compared with some other existing global maps such as GLC2000, GLOBCover2004_2006 and GLCNMO 2003 (version 1). Results of the comparisons showed that it was newer and better than other existing maps for the purpose of urban mapping. This study describes recent progress in producing reliable representations of urban areas at 500m resolution, a part of the project of GLCMNO version 2. Green areas in urban, rural areas and water bodies were better excluded from urban areas by Global Urban Map of GLCNMO 2008 than by GLCNMO 2003. The objective of this study was improving the mapping method by GLCNMO 2003 using automated urban mapping classification and monitoring urban areas at continental and global scales using multi-source Geospatial Data and MODIS data.

1. INTRODUCTION

Currently, the importance and impact of urban area is greater than ever before. More than 50% of population on the Earth now lives in cities, towns and settlements (UN, 2008). Urban areas have profound environmental impacts, including urban heat island effects, conversion and fragmentation of natural ecosystems, loss of agricultural land, contamination of air, soil and water, increased water use and runoff, and reduced biodiversity (Pickett et al., 1997; El Araby, 2002; Alberti, 2005; hepherd, 2005). Urban areas are the primary source regions of anthropogenic carbon emissions (Svirejeva-Hopkins et al., 2004), global models of climate and biogeochemistry include only relatively crude representations of urban areas (Pataki et al., 2006). In a relatively short period of time, urbanization has emerged as a top environmental issue facing many parts of the Earth (Montgomery, 2008). An additional two billion people are expected to arrive in cities by 2050, with nearly 90% of this growth expected in developing countries. Clearly, the impact of urban areas on the human population and the global environment is significant, and will become even more pronounced in the future (Mills, 2007).

Previous studies of urban areas from remote sensing have consistently relied on fine resolution data (Landsat, SPOT, ASTER), which limits these studies to small areas and too expensive for most researchers to acquire and process at continental to Global scales. The six known existing continental scale maps of urban areas include : (1) IGBP DISCover (Loveland et al.,2000) by the U.S. Geological Survey (USGS) using 1 km monthly Advanced Very High Resolution Radiometer (AVHRR) Normalized Difference Vegetation Index (NDVI) composites covering 1992–1993; (2) Global Land Cover map by the University of Maryland (HANSEN. M. C.,2000) using 1 km spatial resolution data for 1992–1993 from the AVHRR; (3) GRUMP (Global Rural Urban Mapping Project); (4) GLC2000 (IES,2000) by the European Space Agency using SPOT VEGETATION data of 2000; (5) GLCNMO by Chiba University (Alimujiang Kasimu,Tateishi, 2008) using MODIS 1 km data of 2003; (6) GLOBCover by the European Space Agency (ARINO, 2007) using MERIS 300m data of 2005.

Table 1 : Review of existing Global Urban Maps

Abbreviation	Organization	Definition of urban or urban-related feature	Data of year	Spatial resolution	Production year	Extent (km^2)
IGBP DISCover	U.S. Geological Survey (USGS)	Urban and Built-up	1992–1993	1 km	1997	NA
Global Land Cover	University of Maryland	Urban and Built-up	1992-1993	1 km	1997	NA
GRUMP	Center for International Earth Science Information Network	Urban extent	1998	1 km	2002	3 524 000
GLC2000	European Space Agency	Artificial surfaces and associated areas	2000	1 km	2004	308 000
GLOBCover	European Space Agency	Artificial surfaces and associated areas (urban areas >50%)	2004-2006	300m	2007	313 000
GLCNMO	Chiba University	Urban and Built-up	2003	1 km	2008	NA

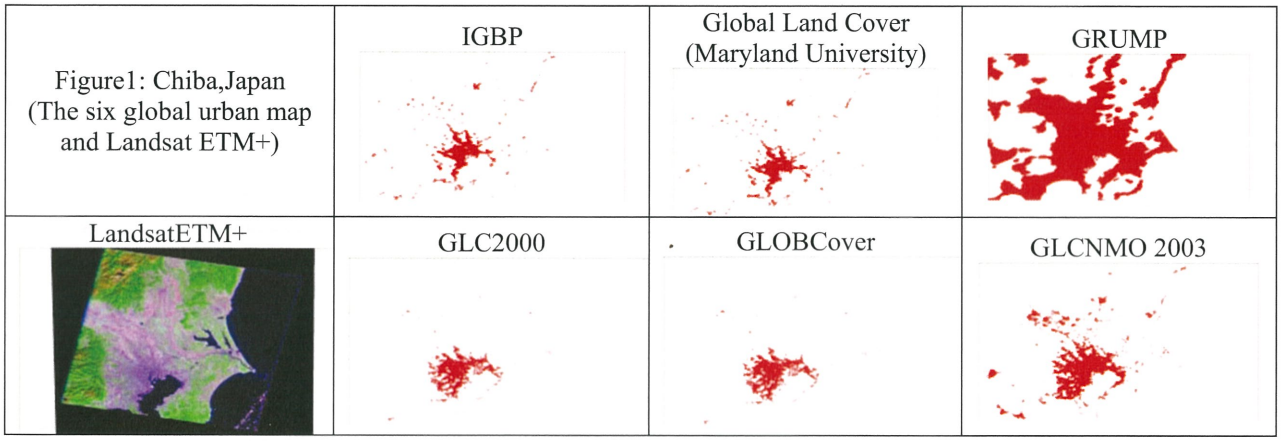

In this paper we present results from an effort to create a new global map of urban, built-up and settled areas. This work builds on previous mapping efforts using Moderate Resolution Imaging Spectroradiometer (MODIS) data at 1 km spatial resolution and multi-source geospatial data (GLCNMO 2003), which is included as part of the project of GLCMNO (Global Land Cover by National Mapping Organization). Here we address weaknesses in the first map as well as several limitations of contemporary global urban maps by developing a methodology that relies solely on newly released Global Urban Map of GLCNMO 2008 using MODIS 500-m resolution data. Specifically, a supervised decision-tree classification algorithm is used to map urban areas using region-specific parameters.

2. USED DATA

Data	Organization	Spatial resolution	Production year	Reference/Source
Population Data (LandScan 2008 Global Population Database 2008)	Geographic Information Science and Technology (GIST)	1km	2008	http://www.ornl.gov/sci/landscan/
Nighttime lights Data:DMSP-OLS	National Geophysical Data Center(NGDC).	1km	2008	http://www.ngdc.noaa.gov/dmsp/
MODIS 2008	CEReS, Chiba University	500m	2008	CEReS, Chiba University
EstISA : Estimate the density of constructed Impervious Surface Area	National Geophysical Data Center(NGDC).	1km	2010	http://www.ngdc.noaa.gov/dmsp/download_global_isa.html
GDP per capita	The International Monetary Fund (IMF)		2008	http://www.imf.org/

2.1. Gridded population density (PD) data of 2008

In this global analysis, population distribution and density data at a spatial resolution of 1km was downloaded from the LandScan global population dataset. The LandScan dataset was compiled on a 30" x 30" latitude/longitude grid. Census counts were apportioned to each grid cell based on likelihood coefficients, which are based on proximity to roads, slope, land cover, nighttime lights, and other information (Dobson,J.E,2000). This monograph is part of series of reports that explain and illustrate methods for applying spatial analysis techniques to investigate urban distribution of the world.

2.2. DMSP-OLS data of 2008

Artificial lighting is a unique indicator of human activity that can be measured from space. The Defense Deteorological Satellite Program's Operational Linescan System (DMSP-OLS hereafter DMSP) collects imagery at night and has a number of unique features that meet the needs of wide-scale, frequently repeated surveys of urban growth. A nighttime lights map was obtained from National Geographical data Center produced using time series data for the year 2008, where pixel values are the average digital number for the year. The human settlements product represents the stable lights in which clouds, gas flares, lightning and other ephemeral and extraneous signals have been screened out leaving only "city lights" (Elvidge, 2001). The products are 30 arc second grids, spanning -180 to 180 degrees longitude and -65 to 65 degrees latitude.

2.3. MODIS-NDVI data of 2008

Spatio-temporal distribution of vegetation is a fundamental component of the urban environment. Vegetation influences urban environmental conditions and energy fluxes by selective reflection and absorption of solar radiation (Gallo,K. P.,1993). Vegetation index data was acquired by MODIS-Moderate Resolution Imaging Spectroradiometer - system includes two satellites: Terra and Aqua. The MODIS 2008 dataset is a cloud free 16-day composite with 7 spectral bands and a 500 m spatial resolution. This dataset was processed by the Center for Environmental Remote Sensing (CEReS) at Chiba University . NDVI was calculated. A Maximum Value Composition (MVC) was then applied to all NDVI images with the aim of selecting pixels less affected by clouds and other atmospheric perturbations (HOLBEN,1986).

2.4 EstISA (Estimate the density of constructed Impervious Surface Area) data of 2010

This data present the global inventory of the spatial distribution and density of constructed impervious surface area (ISA). Examples of ISA include roads, parking lots, buildings, driveways, sidewalks and other manmade surfaces. While high spatial resolution is required to observe these features, the new product reports the estimated density of ISA on 1 km^2 grid based on two coarse resolution indicators of ISA – the brightness of satellite observed nighttime lights and population count.(Christopher D. Elvidge , 2007)

2.5 GDP per capita data of 2008

Gross domestic product based on purchasing power parity per capita data of 2008 from The International Monetary Fund (IMF) . This data is used to divide the countries into 4 groups according to level of development. It is the basic index for distinguishing characteristics of urban areas.

3. METHODOLOGY

3.1 Definition of urban area

Global Urban Mapping is always difficult because of the different definition of "urban area" in different countries. It is important to provide a clear conceptual framework of the urban environment for regional and global mapping studies. "Urban area" is a depiction of land use, and includes commercial, industrial, residential and transportation land use types, because these classes are most functional for urban planners and practitioners. These classes are distinct from land cover, which is defined as the physical attributes, composition, condition and characteristics of the Earth's surface. Urban areas are heterogeneous mixtures of land cover types, and may contain any number of vegetated (grass, shrubs, and trees) and man-made surfaces (cement and asphalt). In this study, a definition of urban areas based on physical attributes: urban areas are places that are dominated by the built environment. The 'built environment' includes all non-vegetative, human-constructed elements, such as buildings, roads, runways, etc. (i.e. a mix of human-made surfaces and materials), and 'dominated' implies coverage greater than or equal to 50% of a given landscape unit (here, the pixel) (Schneider et al., 2010). Pixels that are predominantly vegetated (e.g. a park) are not considered urban, even though in terms of land use, they may function as urban space. Although 'impervious surface' is often used to characterize urban areas within the remote sensing literature (Ridd, 1995), this study prefer the more direct term 'built environment' because of uncertainty and scaling issues surrounding the impervious surface concept (Small, 2003; Small & Lu, 2006; Stow et al., 2007). In remote sensing, "urban area" is often best defined as population density distribution, as percentage of impervious surface, nighttime light. Green fields and water bodies (such as a big park or a golf course) were not considered as urban.

Finally, this study also define a minimum mapping unit: urban areas are contiguous patches of built-up land greater than 1 km^2.

3.2 Data processing

In this section, a methodology for creating continent scale map of urban area using multiple sources of input data is described. The methods involved 5 main steps as shown in Fig.2.

First step is preprocessing. Population Density, DMSP and EstISA Data at spatial resolution of 1km were downloaded. Then they were resembled from "spatial resolution of 1km" to "spatial resolution of 500m".

Secondly, "Gross domestic product based on purchasing power parity (PPP) per capita GDP 2008" data is used to divide the countries into 4 groups according to level of development. It is the basic index for distinguishing characteristics of urban areas

Thirdly, each continent (Eurasia, Africa, North America, South America, Oceania) with 4 groups of level development, threshold gridded population density data, nighttime lights (DMSP) and Density of constructed Impervious Surface Area (EstISA) data with a reference of fine resolution Landsat ETM+.

Fourthly, using maximum MODIS-NDVI data of 23 periods exclude green areas in the urban area. This research generate NDVI_Max with the maximum algorithm as expressed in (Eq.1)

$$NDVI\_Max=Max\{NDVI\_1, NDVI\_2,\ldots,NDVI\_23\} \quad (Eq.1)$$

Where, NDVI_1, NDVI_2,…,NDVI_23 are the multi-temporal MODIS-NDVI images acquired staring from 2008/01/01 to 2009/01/02.

Fifthly, DMSP and Density of constructed Impervious Surface Area (EstISA) are used to exclude rural areas around urban. In this way, information from all three data sources was combined to create a final map of urban area and compared with fine resolution Landsat ETM+ and other existing global urban maps.

Figure 2 : Flowchart of urban mapping methodology

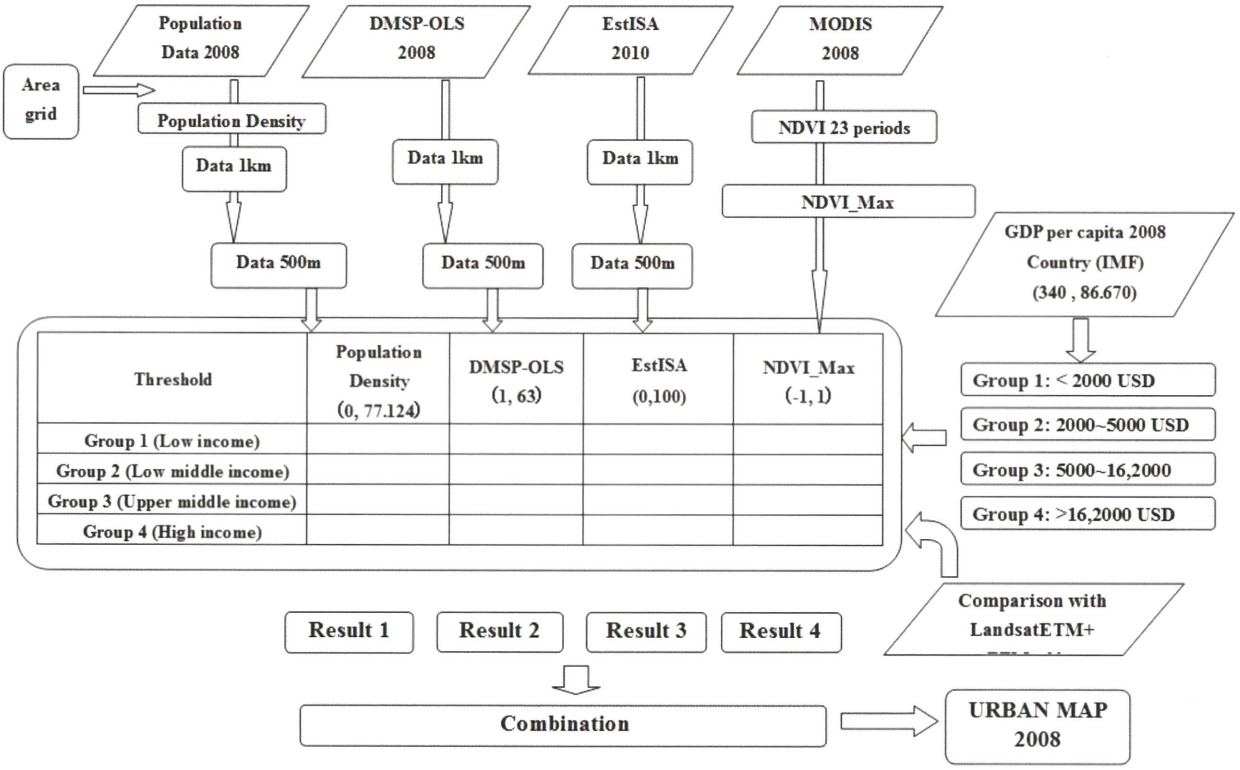

Regions	Threshold	Population Density (0, 77.124)	DMSP-OLS (1, 63)	EstISA (0,100)	NDVI_Max (-1, 1)
Eurasia	Group 1 (Low income)	800	5	3	0.52
	Group 2 (Low middle income)	800	10	5	0.62
	Group 3 (Upper middle income)	500	15	7	0.72
	Group 4 (High income)	500	20	10	0.82
Africa	Group 1 (Low income)	800	3	3	0.42
	Group 2 (Low middle income)	800	5	5	0.47
	Group 3 (Upper middle income)	500	10	7	0.52
	Group 4 (High income)	500	15	10	0.57
North America	Group 1 (Low income)	800	5	3	0.52
	Group 2 (Low middle income)	800	10	5	0.62
	Group 3 (Upper middle income)	500	15	7	0.72
	Group 4 (High income)	500	20	10	0.82

South America	Group 1 (Low income)	800	5	3	0.52
	Group 2 (Low middle income)	800	10	5	0.62
	Group 3 (Upper middle income)	500	15	7	0.72
	Group 4 (High income)	500	20	10	0.82
Oceania	Group 1 (Low income)	800	3	3	0.52
	Group 2 (Low middle income)	800	5	5	0.62
	Group 3 (Upper middle income)	500	10	7	0.72
	Group 4 (High income)	500	15	10	0.82

4. RESULTS

The GLCNMO Urban Map 2003 results are quite accurate in continental and national scales. However, misclassified pixels occurred when compared with Landsat ETM+ and high-resolution urban map from Google earth. Especially in developed region like Europe, some residential area with lots green or near big parks were misclassified as green area. In addition, the scale of cities in developing countries is different from the rest of the word, so that most small cities in Asia are not represented. But this product Global Urban Map 2008 can do it better, specifically it can exclude green areas in the urban area is better than GLCNMO 2003.

Figure 3 : Excluding green areas in Nagoya Higashiyama Park.

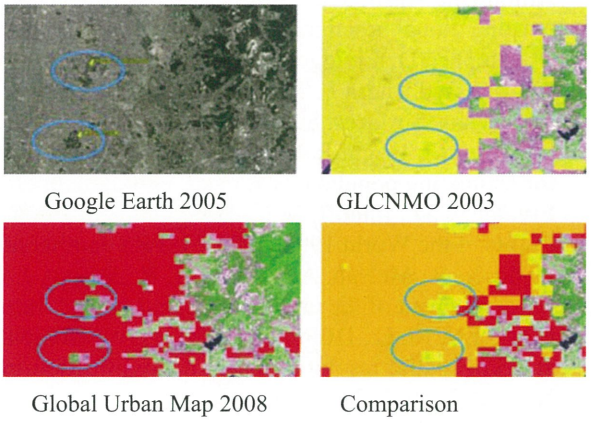

The Urban map produced in this study was compared with some other existing global maps such as GLC2000, IGBP, GLOBCover, GRUMP, GLCNMO 2003. Results of the comparisons show that product of this study, Global Urban Map 2008, is newer and better than other existing maps for the purpose of Urban mapping.

Figure 4: Comparisons 1 (Urban area in Ha Noi, Viet Nam)

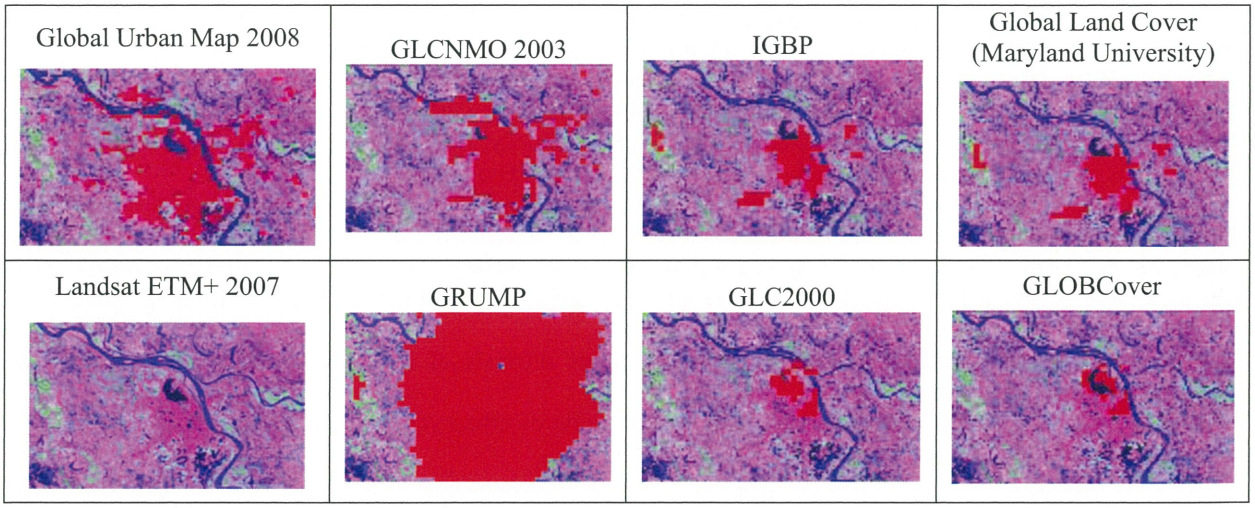

Figure 5: Comparisons 2 (Urban area in Jakarta, Indonesia)

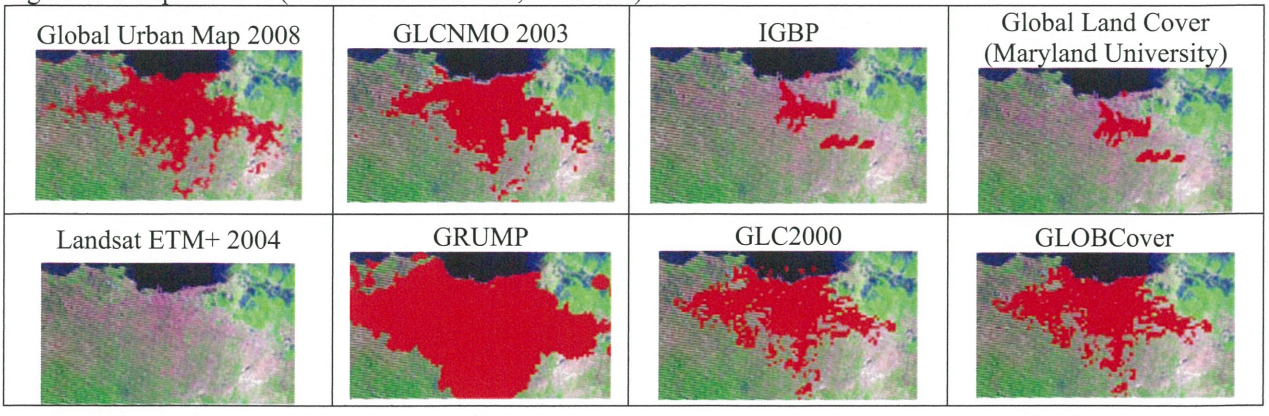

Acknowledgments

This work was supported by JSPS Grant-in-Aid for Scientific Research, KAKENHI (22220011).

References :

ARINO, O., GROSS, D., RANERA, F., BOURG, L., LEROY, M., BICHERON, P., LATHAM, J., GREGORIO, A. D., BROCKMAN, C., WITT, R., DEFOURNY, P., VANCUTSEM, C., HEROLD, M., SAMBALE, J., ACHARD, F., DURIEUX, L., PLUMMER, S., WEBER, J., GLOBCover: ESA service for Global Land Cover from MERIS. International Geoscience and Remote Sensing Symposium (IGARSS), pp. 2412 – 2415, 23-28 July 2007.

Alimujiang Kasimu and Ryutaro Tateishi, 2008, GLCNMO global urban mapping, validation and comparion with existing global urban maps, Journal of the Remote Sensing Society of Japan, 28(5), pp.427-440.

Christopher D. Elvidge , Benjamin T. Tuttle , Paul C. Sutton , Kimberly E. Baugh ,Ara T. Howard , Cristina Milesi , Budhendra L. Bhaduri and Ramakrishna Nemani, 2007. Global Distribution and Density of Constructed Impervious Surfaces. Sensors 2007, 7, pp. 1962-1979.

Dobson,J.E., Bright,E.A., Coleman, P.R., Durfee,R.C., and Worley,B.A,"LandScan, A global population database for estimating populations at risk," Photogrammetric Engineering and Remote Sensing, 2000 , 66(7),pp. 849-857.

Elvidge, C.D., Imhoff, M.L., Baugh, K.E, Hobson, V.R., Nelson, I.,Safran, J, Dietz, J.B, & Tuttle, B.T, "Nighttime Lights of the World,1994–1995," ISPRS Journal of Photogrammetry and Remote Sensing,2001, 56, pp.81–99.

Gallo, K. P., McNab, A. L., Karl, T. R., Brown, J. F., Hood, J. J., and Tarpley, J. D., "The use of a vegetation index for assessment of the urban heat island effect," International Journal of Remote Sensing, 1993,14, pp.2223- 2230.

HANSEN. M. C., DEFRIES, R. S., TOWNSHEND, J. R. G. and SOHLBERG, R., Global land cover classification at 1 km spatial resolution using a classification tree approach. International Journal of Remote Sensing, Vol. 21, No. 6 & 7, pp. 1331–1364, 2000.

HOLBEN, B.N. , 1986: Characteristics of maximum value composite Images from temporal AVHRR data. International Journal of Remote Sensing., 7,pp. 1417-1434.

IES (Institute for Environment and Sustainability), Global Land Cover 2000, 2010. Available online at: http://ies.jrc.ec.europa.eu/our-activities/global-support/Global Land Cover 2000.mht (accessed 18 Aug. 2011)

LOVELAND, T. R., REED, B. C., BROWN, J. F., OHLEN, D. O., ZHU, Z., YANG, L. and MERCHANT, J. W., Development of a global land cover characteristics database and IGBP DISCover from 1 km AVHRR data. International Journal of Remote Sensing, vol. 21, no. 6 & 7, pp. 1303–1330, 2000.

Mills, G. (2007). Cities as agents of global change. International Journal of Climatology,27, 1849–1857.

Montgomery, M. (2008). The urban transformation of the developing world. Science,319, 761–764.

Pataki, D. E., Alig, R. J., Fung, A. S., Golubiewski, N. E., Kennedy, C. A., McPherson, E. G.,et al. (2006). Urban ecosystems and the North American carbon cycle. Global Change Biology, 12, 2092–2102.

Pickett, S., Burch, W., Dalton, S., Foresman, T., Grove, M., & Rowntree, R. (1997). A conceptual framework for the study of human ecosystems in urban areas. Urban Ecosystems, 1, 186–199.

Ridd, M. K. (1995). Exploring a V-I-S (vegetation-impervious surface-soil) model for urban ecosystem analysis through remote sensing − Comparative anatomy for cities. International Journal of Remote Sensing, 16, 2165–2185.

Small, C. (2003). High spatial resolution spectral mixture analysis of urban reflectance. Remote Sensing of Environment, 88, 170–186.

Small, C.,&Lu, J. (2006). Estimation and vicarious validation of urban vegetation abundance by spectral mixture analysis. Remote Sensing of Environment, 100, 441–456.

Schneider, A., Friedl, M A., Potere, D., Mapping global urban areas using MODIS 500-m data: New methods and datasets based on urban ecoregions, Remote Sensing of Environment 114 (2010), pp. 1733–1746.

Stow, D., Lopez, A., Lippitt, C., Hinton, S., & Weeks, J. (2007). Object-based classification of residential land use within Accra, Ghana based on QuickBird satellite data. International Journal of Remote Sensing, 28, 5167–5173.

Svirejeva-Hopkins, A., Schellnhuber, H. J., & Pomaz, V. L. (2004). Urbanised territories as a specific component of the global carbon cycle. Ecological Modelling, 173, 295–312.

United Nations Department of Economic and Social Affairs, Population Division (2008).World Urbanization Prospects: The 2007 Revision. : United Nations Publications.

The Relationship between Outbreak of Asian Dust and Ground Condition in East Asia

Feifei Cui[1] Akihiko Kondoh[2] Nobumitsu Tsunematsu[3]

[1]Graduate School of Science, Chiba University
(〒263-8522 1-33 Yayoi-cho, Inage-ku, Chiba-shi, Japan)
E-mail: saihihi@gmail.com

[2]Center for Environmental Remote Sensing, Chiba University
(〒263-8522 1-33 Yayoi-cho, Inage-ku, Chiba-shi, Japan)
kondoh@faculty.chiba-u.jp

[3]National Research Institute for Earth Science and Disaster Prevention
(〒305-0006 3-1,Tennodai,Tsukuba-shi,Ibaraki-ken,305-0006,Japan)

KEY WORDS: Remote sensing, Asian Dust, SPOT/VGT, Ground Condition, NDVI, Duration

ABSTRACT: According to the observation total days of dust in Japan, which has been made public by the Japan Meteorological Agency, the observation days are greatly different depending on the age. The number of dust events observed in Japan increased in 2000, and continued to 2002, following sharp drop in 2003. There must be a factor in such a rapid change. It is thought that the factor includes which on an atmospheric side and the ground level side. In this study, we will focus on the state of the ground condition, aim to clarify the change in the ground level, which corresponds to the change of the dust observation days. So we discussed the relationship between outbreak of dust and the ground condition, with monitoring the state of ground lever by satellite data and analyzing the change by meteorically data.

1. INTRODUCTON

In East Asia, Dust is called yellow sand, and spring in particular has much outbreak. Not only from a scientific viewpoint but also from a standpoint of environmental problems, it is considered as an important problem to discuss the generation factor. It is thought that although dust is a natural phenomenon, the human activities are related to the outbreak. The number of dust events observed in Japan increased in 2000, and continued to 2002, following sharp drop in 2003. There must be a factor in such a rapid change. We discussed the relationship between outbreak of dust and the ground condition, with monitoring the state of ground lever by satellite data and analyzing the change by meteorically data.

2. DATA AND METHODS

As satellite data, we used SPOT/VEGETATION 1km 10-day data, which can be downloaded free of charge from the following URLhttp://free.vgt.vito.be/. Each data file is comprised 10-day maximum-value c omposite (MVC) NDVI bands. The sensor has 4 spectral bands: blue, red, near-infrared (NIR) and mid-infrared (MIR). We can extract the information on the snowfall and vegetation from this band data. The red and NIR bands are used to characterize vegetation with normalized difference vegetation index NDVI=(NIR-R)/(NIR+R). The foliation of vegetation made the period a map each year by expediently using NDVI=0.1 as a threshold. And the red and MIR bands are used to characterize snow with normalized difference snow index NDSI= (MIR-R)/(MIR+R). 0.2 was used as a threshold based on Kondo and Suzuki (2005) for the identification of the snowfall region and non-snowfall region.

3. RESULTS

In the semiarid area in East Asia, the period of bare land is able to be made a map by taking the difference of thaw and foliation each year. There seems to be a good correlation between the two when the length of the bare land is compared with the dust observation total days each year. We choice the meteorological observing station in Inner Mongolia of China, do the same as before. As the result, when the length of bare land was long, the dust observation was high.

4. DISCUSSION

As a statistic of the yellow sand outbreak using SYNOP data, in the year of the longer bare land duration, the thaw was earlier, and the average temperature of spring was higher. Therefore, it is thought that is related between the earlier thaw and the higher temperature of the snow melting period. On the other hand, the foliation in the year of earlier thaw is later. In East Asia spring is dry season when precipitation is a little. In the semiarid area, the growth of herbs depends on the moisture condition (Kondoh et al.,2005). Therefore, in the year of earlier thaw, it is possible that dryness controls the germination and growth of the herbs vegetation.

5. CONCLUSIONS

It was similar to the result of last year to here, but as a result of having added more detailed examination, it became clear that an earth surface characteristic to be concerned with yellow sand outbreak every area was different, that, in addition, inter-annual variations was big. Therefore, adding the examination of the topography condition and the consideration of ecology zone, the reexamination result of the yellow sand outbreak condition will be reported from a viewpoint of time and space.

REFERENCES

Akihiko KONDOH, Rikie SUZUKI(2005): Snowcover Mapping and Its Interannual Variation in Northern Eurasia. Journal of Japan Society of Hydrology & Water Resources 18(6), 696-703.

Akihiko KONDOH, Ichirow KAIHOTSU(2005): Preliminary Analysis on the relationship between vegetation activity and climatic variation in Mongolia. Journal of Arid Land Studies 14(4), 209 -218.

Study on the spatial-temporal variations of soil moisture in arid region of East Asia

Mei SUN*, Akihiko KONDOH+,Ichirow KAIHOTSU#

*Graduate School of Science, Chiba University,Japan
1-33 Yayoi Cho, Inage Ku, Chiba Shi, Chiba, Japan; Tel: + 81-43-2902969;
E-mail: sunmeijp@garaduate.chiba-u.jp
+Professor,Center for Environment Remote Sensing,Chiba University,Japan
1-33 Yayoi Cho, Inage Ku, Chiba Shi, Chiba, Japan; Tel: + 81-43-2902969;
E-mail: kondoh@faculty.chiba-u.jp
#Professor,Graduate School Of Integrated Arts and Sciences,Hiroshima University,Japan
1-7-1 Kagamiyama KU, Chiba Shi, Higashihiroshima, Japan; Tel: + 81-82-4240758;
E-mail: kaihotu@hiroshima-u.ac.jp

KEY WORDS: AMSR-E soil moisture,precipitation,

ABSTRACT: Soil moisture plays a very important role in earth's water cycle. In East Asia,there are so many different areas like desert,semiarid ,steppe and so on. Study on these leads to understand more about climate and land surface change in the future. Mircrowave remote sensing is a effective method to measure soil moisture in large areas. AMSR-E(Advanced Microwave Scanning Radiometer for EOS) is a sensor which provides timely,long-term,quality informations on land hydrology. In this study, we use AMSR-E(Koike Ver.5.31)soil moisture dataset and APHRODITE 's Water Resources (Asian Precipitation-Highly-Resolved Observational Data Integration Towards Evaluation)dataset, validate the AMSR-E(Koike Ver.5.31) soil moisture dataset, and analyse the temporal-spatial variations of soil moisture in arid regions of East Asia.

This study shows two areas of China, XinJiang and Inner Mongolia as a example. We make soil moisture maximum value image of month and soil moisture minimum value image of month. And we find the difference by the two values subtraction.

As a result, soil moisture maximum value of month minus soil moisture minium value of month is very large in arid region,and soil moisture memory is small. Soil moisture memory ,in essence the fact that soil can"remember "a wet or dry anomaly long after the condition responsible for the anomaly are forgotten by the atmosphere(Randal D.Koster 2001).AMSR-E(Koike Ver.5.31) can capture the characteristics of soil moisture in arid regions very well .In the temporal ,among four seasons, summer can show the better correlation between soil moisture and precipitation. In winter possiblly because there is snow on the ground and the reason will be clarified in the next research. In the spatial,the correlation between soil moisture and precipitation is lower in west inner mongolia than east part.(west part is dry than east part in inner mongolia). According to APHRODITE's feature, near APHRODITE observation point the correlation between soil moisture and precipitation is higher,far from the APHRODITE observation point the correlation between soil moisture and precipitation is lower.No doubt soil moisture is also be affected by many factors,like vegetation, surface temperature and so on.Their relationship will be analyzed in the next step.

1. Introduction

Soil moisture play a very important role in water cycle,especially in arid area.In East Asia,there are so many different areas like desert,semiarid ,steppe and so on. Study on these leads to understand more about climate and land surface change in the future. Microwave remote sensing with satellite is a very effective method to measure soil moisture in large area with short recurrent time.

2. Study area

China(Inner Mongolia)

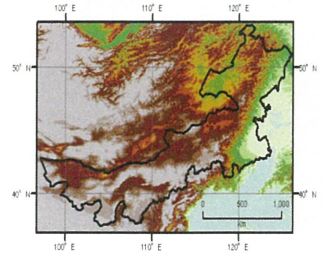

China(Xinjiang)

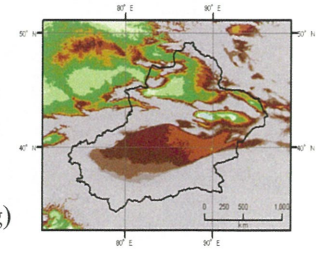

3. Data

AQUA AMSR-E(Advanced Microwave Scanning Radiometer for EOS) Soil Moisture data(ver. koi531), temporal resolution is everyday, spatial resolution is 0.125°. It's used for the regional observation of soil moisture.Research Institute for Humanity and Nature offer APHRODITE`s Water Resources （Asian Precipitation Highly-Resolved Observational Data Integration Towards Evaluation） .Using data period is from 2003 to 2007.Elevation data is from GTOPO30.

4. Objective

To validate the AMSR-E soil moisture(Koike Ver.5.31), and also to clarify the temporal and spatial variation of soil moisture in the arid regions of east Asia. This study shows two areas of China, XinJiang and Inner Mongolia as a example.

5. Result

5.1 Relationship between soil moisture and precipitation

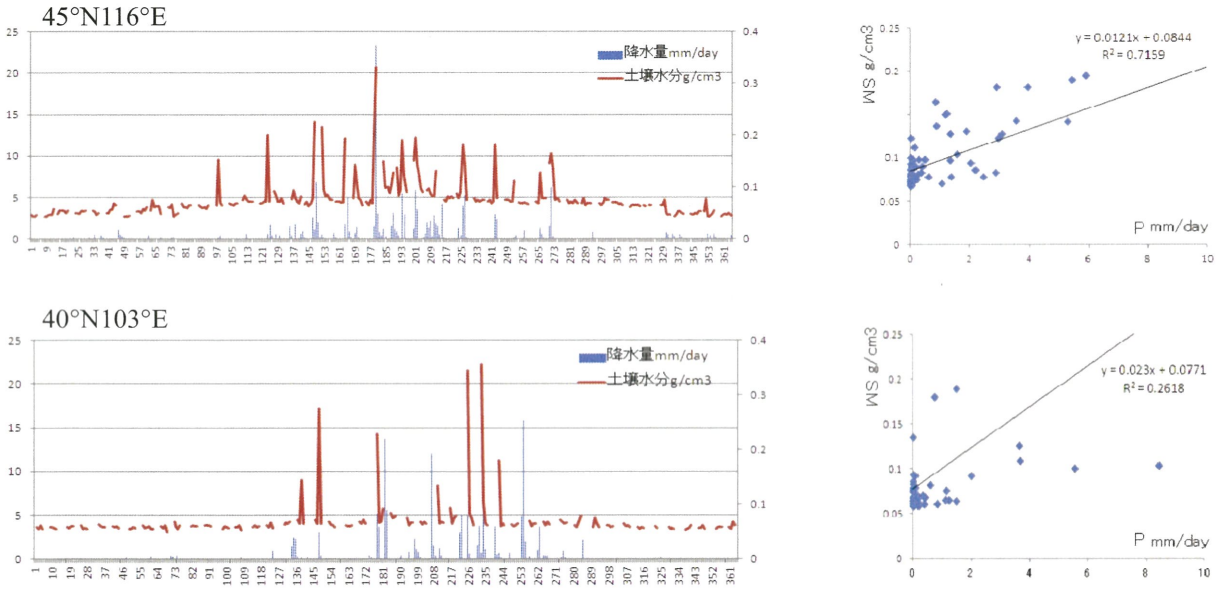

The figures show soil moisture and precipitation at Inner Mongolia （45°N116°E) and （40°N103°E) in 2005. .Correlation is higher in west Inner Mongolia than east Inner Mongolia.

5.2 Satellite images of AMSR-E soil moisture in different seasons

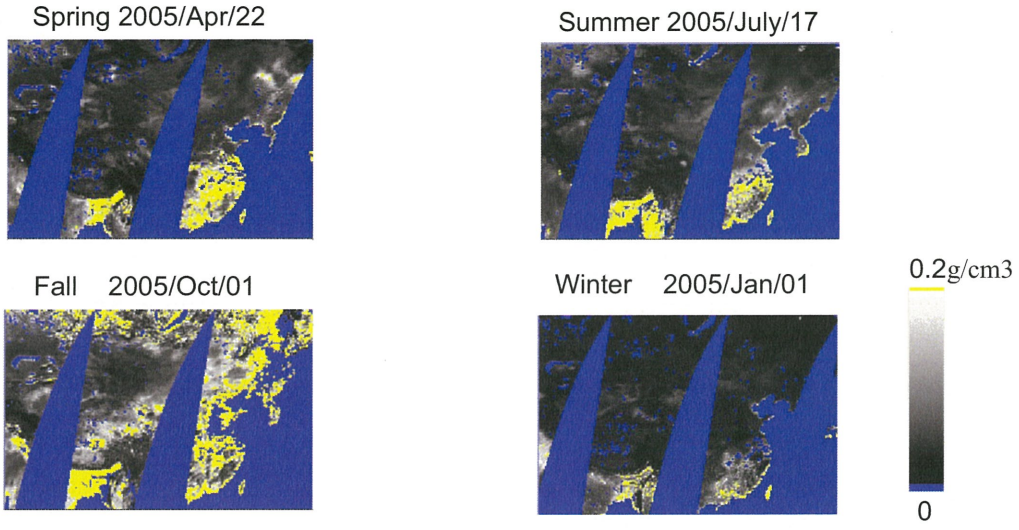

From satellite images can see soil moisture value is higher in summer ,and in winter the value is smaller.AMSR-E soil moisture estimation is good and useful for surface soil moisture monitoring over a large scale.

5.3 Variation of AMSR-E Soil moisture value in one month

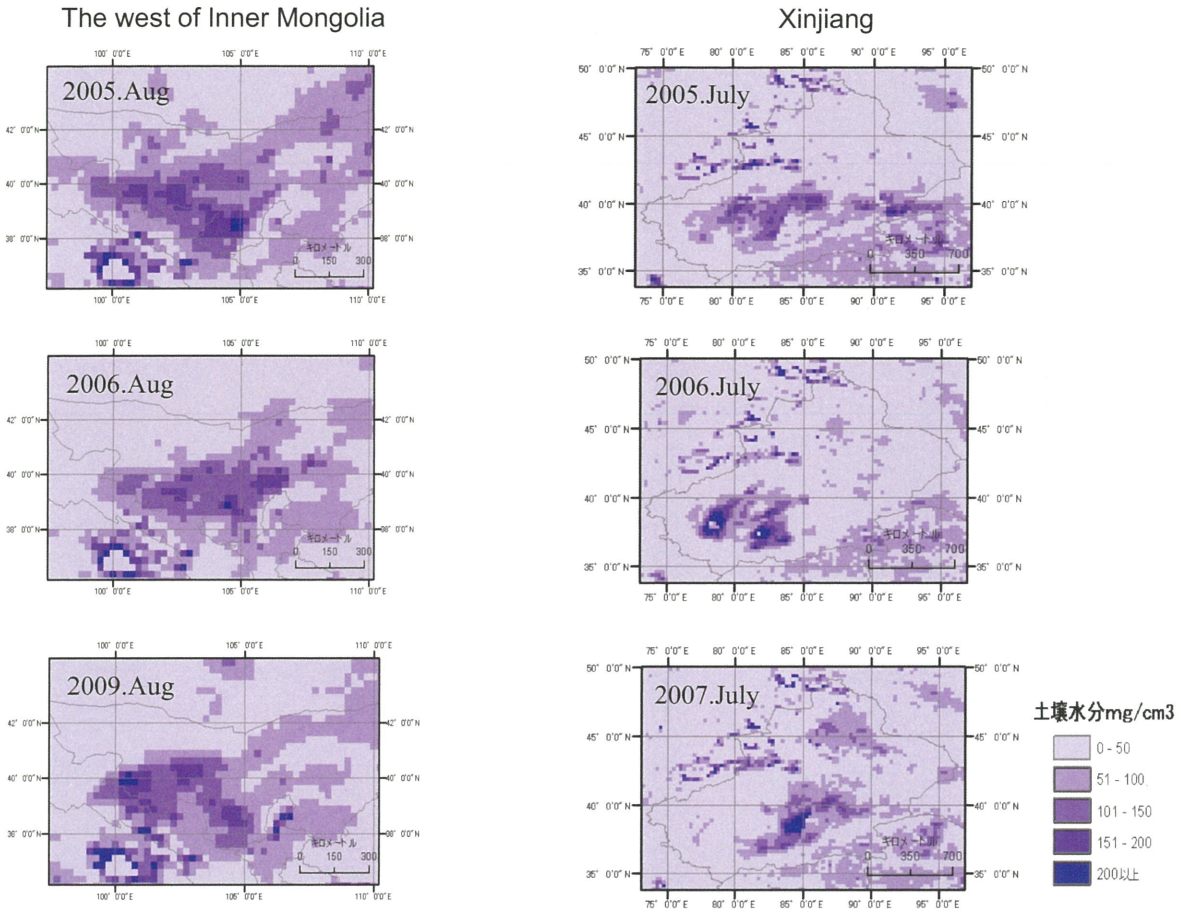

The six figures show that month change of soil moisture in different years in west of inner Mongolia and Xinjiang.Variation of AMSR-E Soil moisture value in one month is big in arid areas. AMSR-E can monitor soil moisture in arid area very well.

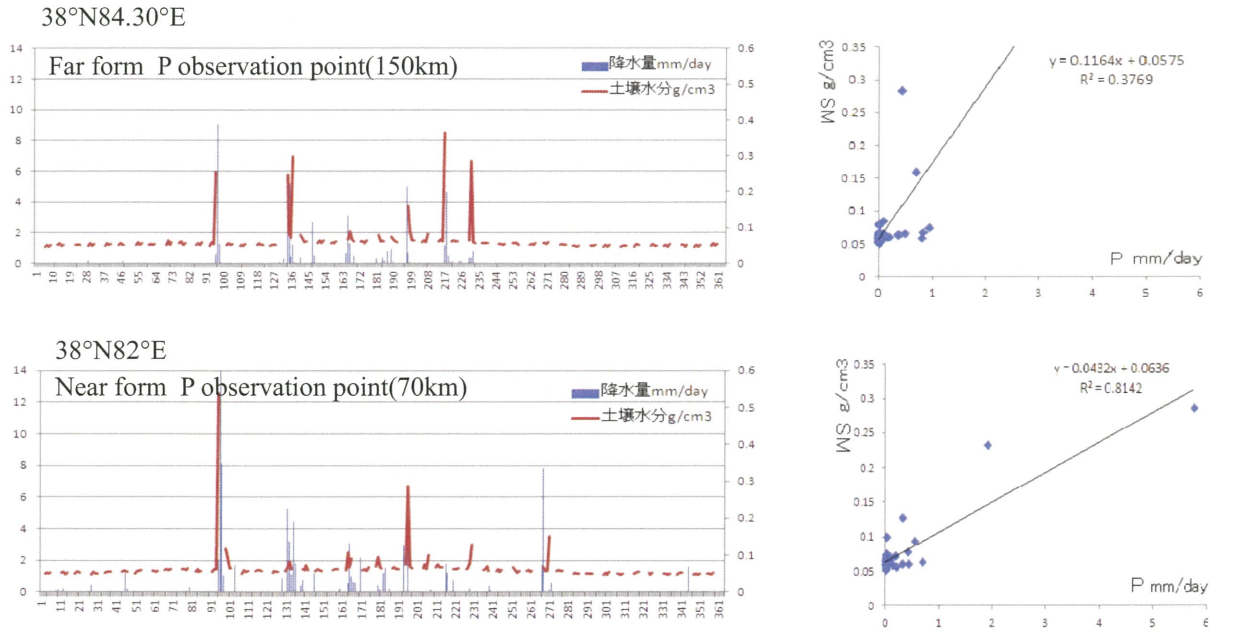

Correlation between soil moisture and precipitation at Xinjiang（38°N84.30°E)and（38°N82°E)in 2005

The correlation between soil moisture and precipitation in temporal change,among four seasons, summer can show the better,and in spatial change,that is lower in west inner Mongolia than east part. Near from APHRODITE observation points show higher correlation between soil moisture and precipitation.

ASSESSMENT OF SOIL SALINITY IMPACT ON COASTAL AGRICULTURE DUE TO CLIMATE CHANGE

Taru Lata Shapla,[1,2] Motaleb Hossain Sarker[3] Mohammed Ali Bhuyian[4], and Hiroaki Kuze[2]

[1]*Department of Agro-forestry & Environmental Science , Sher-e-Bangla Agricultural University, Dhaka- 1207, Bangladesh, tarulatashapla@yahoo.com*

[2]*Center for Environmental Remote Sensing, (CEReS), Chiba University, 1-33 Yayoi-cho, Inage-ku, Chiba 263-8522,Japan, hkuze@faculty.chiba-u.jp*

[3]*Center for Environmental and Geographic Information Services, Dhaka- 1212, Bangladesh. motalebsarker@gmail.com*

[4]*Department of Water Resources Engineering, Bangladesh University of Engineering and Technology (BUET), Dhaka-1000, Bangladesh.*

ABSTRACT

This paper presents an assessment of the spatial and temporal distributions of soil salinity in the coastal region of Bangladesh. The severity levels are evaluated using geographic information system (GIS) analysis as the major source of information. The result shows that a total of 1,82,310 ha new land is affected in the region by various degrees of soil salinity during a three-decade period from 1973 to 2000, which is about 28% increment of the total salinity area compared to the initial area in 1973. The spatial extent of salinity has shown an increasing trend, with noticeable changes in soil salinity from coastal areas to northern areas. Considerable salinity has reached the Magura district, about 240 km north from the coast. Furthermore, it has been found that different districts of Bangladesh such as Khulna, Bagerhat, Barguna, Satkhira, Barisal have been affected by different degrees of soil salinity, due presumably to sea level rise caused by global climate change. As a result, the crop productivity in some of these districts has decreased at an alarming level. The results of this study will help the decision makers and planners to consider sustainable social, agricultural, environmental and water resources management plans in and around the coastal region of Bangladesh.

KEYWORDS: Soil salinity, coastal soil, soil degradation, sustainable, climate change and GIS.

1. INTRODUCTION

Salinity is an important issue in the coastal region of Bangladesh. Due to the presence of salinity in water and soil, the people of the region are suffering from water shortage for drinking, irrigation, agriculture and other uses. Ecology in the southwest region, in particular, has become a great concern. Furthermore, agriculture is the major sector of the economy of Bangladesh and the southwest region of the country is suitable for growing rice. Out of 1.14 million hectares of coastal and offshore lands, about 0.37 million hectares of arable land have been badly affected in the greater Khulna region by various degrees of salinity in different cropping seasons (NWMP, 2001). Most of the lands remain fallow in the dry season and no crop grows due to salinity hazard and lack of freshwater (BARC-BRRI, 2001). Besides salinity, in a relatively recent development, it is found that about 138,600 ha of land are under shrimp farming in this ecologically sensitive region (EGIS, 2001a). Out of that, about 42,550 ha, 36,500 ha, and 49,550 ha of lands of Satkhira, Khulna and Bagerhat districts, respectively, are under Bagda shrimp cultivation. Because of these trends, the biodiversity of coastal region including the Sundarbans (the largest mangrove forest of the world) are under greater threat, and many species of flora and fauna are becoming extinct. Thus, the spatial and temporal change in the distribution of salinity is one of the important aspects for developing the environmental management plan (Haque A.U. 2009, Panaullah 1993).

Nowadays, climate change has become an important issue worldwide. In 1990, Intergovernmental Panel on Climate Change (IPCC) estimated that with a business-as-usual scenario of greenhouse gas emission, the average temperature would be 3.3°C warmer by the end of the 21st century, with a range of uncertainty between 2.2 and 4.9°C (Warrick et al., 1993). With such a rise in temperature, sea level will rise because of the thermal expansion of sea water and melting of polar ice. In Bangladesh, sea level rise will cause land erosion, salinity intrusion and loss in biodiversity.

2. METHODOLOGY

The major sources of data and information are Soil Resources Development Institute (SRDI), Bangladesh Water Development Board (BWDB), Water Resources Planning Organization (WARPO), Center for Environmental and Geographic Information Services (CEGIS), and Bangladesh Agricultural Research Council (BARC), as well as internet sites. All the spatial (GIS) data were converted into the same geographic projection (Bangladesh Transverse Marcator or BTM) system so that they have nearly the same spatial and temporal coverage.

The spatial data were analyzed using ArcGIS, and attribute data (including time series data) were analyzed using Microsoft Access and Excel. The advanced tools of ArcGIS (e.g. Spatial Analyst and Geo-statistical Analyst) have been used for performing the GIS analysis. The secondary GIS data from SRDI, CEGIS and WARPO were also

used to prepare the salinity maps. Then, the spatial and temporal variations of soil salinity distributions were analyzed through visual as well as digital interpretation.

3. RESULTS AND DISCUSSION

Spatial distribution of soil salinity: Figure 1(a) shows the spatial distribution of soil salinity in 1973 based on the GIS analysis of the SRDI data. Here it can be observed that highly saline areas, defined with the soil electric conductivity of more than 15 dS/m, are spreading in most of the southwestern districts including Satkhira, Khulna, and Bagerhat. Figure 1(b) depicts the result of more recent study (SRDI, 2009): in this figure, it is found that some of the new lands of Pirojpur, Barguna, Patuakhali, Bhola have been affected. In addition, inland regions such as Jessore, Narail, Gopalganj, Jhalokati, Barisal, and Madaripur districts are affected by different degrees of soil salinity, which could reduce the crop productivity therein.

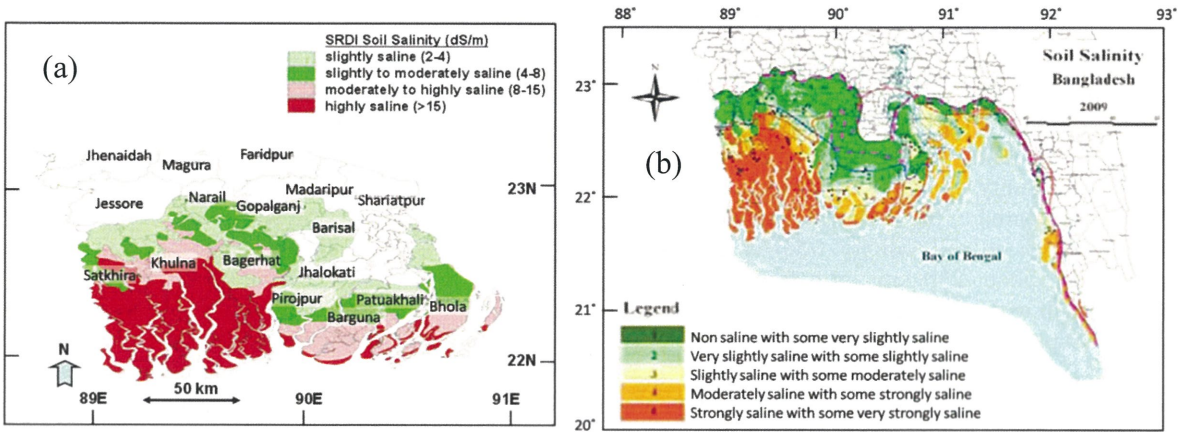

Figure 1. Spatial distribution of dry season soil salinity: (a) maximum soil salinity in 1973 and (b) in 2009.

Table 1. Different classes of soil salinity areas in 1973 and 2009 (source: SRDI)

Different classes of soil salinity areas (dS/m)	Salinity affected area in 1973 (ha)	Salinity affected area in 2009 (ha)
Highly saline (> 15)	20700	281340
Moderately to highly saline (8-15)	49100	225420
Slightly to moderately saline (4-8)	341730	271800
Slightly saline (2-4)	242120	92470
Total salinity area	**653650**	**871030**

Temporal distribution of soil salinity: Table 1 summarizes the changes in the area coverage for different soil salinity levels between 1973 and 2009. It is noticeable that highly saline areas with conductivity of more than 15 dS/m have increased by a factor of 13.6 during a period of 36 years, due presumably to the sea level rise coupled with land subsidence effects in the coastal districts.

Furthermore, temporal and spatial statistics are illustrated in Figs. 2(a)-(c). Figure 2(a) indicates that the total soil salinity area, defined as the area with conductivity of more than 2 dS/m, has increased substantially in 1997, but slightly decreased in 2000 and again increased in 2009. The decrease in 2000 could be attributed to the increased freshwater flow through Ganges-Gorai system after its restoration in 1999 (EGIS, 2001b).

District-wise distribution of soil saline areas for the year 2000 is shown in Fig. 2(b). Most of the soil salinity areas are in the districts of Bagerhat, Barguna, Khulna, Patuakhali and Satkhira, which are covering around 80% of the total saline areas in total. Around 30% is affected in the Bhola district, while in Madaripur, Gopalganj, Jhalokati, Jessore and Barisal, the percentile is less than 20%.

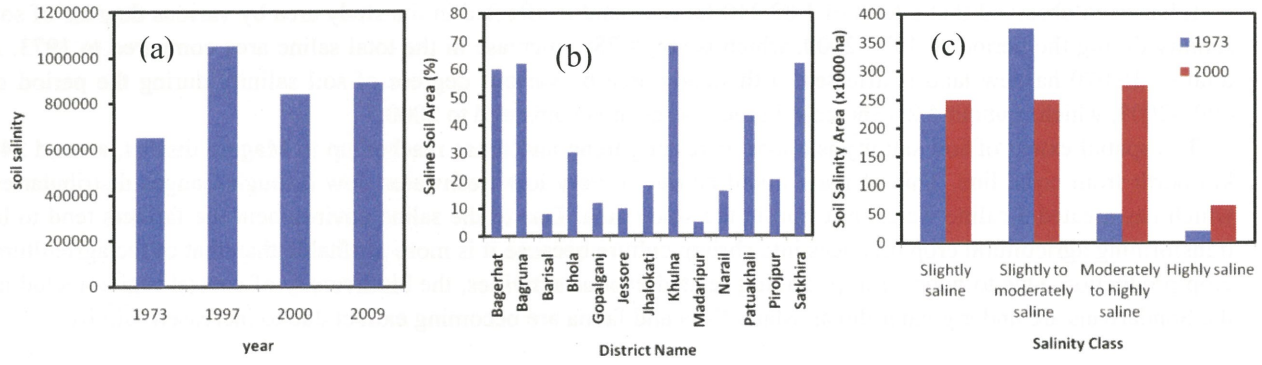

Figure 2. Soil salinity statistics: (a) Year-wise comparison of total area affected with soil salinity (more than 2 dS/m), (b) district wise salinity distribution in 2000, and (c) comparison of soil salinity between 1973 and 2000.

According to a previous study (Sarker, 2005), it was found that about 182,300 ha new land had been affected by various degrees of soil salinity during the last three decades (Figure 2c). Possible reasons for this trend are freshwater withdrawal from upstream, introduction of brackish water shrimp cultivation, faulty management of sluice gates, regular saline tidal water flooding in unpoldered areas, capillary rise of soluble salts from saline groundwater table at shallow depth, etc.

Table 2: Yield performance of non-rice crops irrigated by saline water in the coastal area (Mondal, 2001)

Name of crops	Maximum yield (t/ha)	Electrical conductivity (dS/m)		Yield loss, %
		Irrigation water	Soil	
Wheat	2.45	1.55-1.80	4.00-4.85	25
Burley	2.17	1.55-1.80	4.00-4.85	29
Millet (Kaon)	1.07	1.50-1.80	4.00-4.75	12
Cheena (Bogai Kanchi)	1.46	1.50-2.00	4.85-4.90	22
Maize (Shuvra)	3.95	1.50-2.00	5.80-6.20	45
Chick pea	0.78	1.50-2.00	3.75-4.95	-

Table 3: Yield loss at different growing stages of rice irrigated by saline water (Das and Mehrotra, 1971).

Growth stage of rice	Yield loss, %			
	EC = 3 dS/m	EC = 8 dS/m	EC = 14 dS/m	EC = 21 dS/m
Early stage	0	50%	75%	96%
Reproductive stage	0	0	10%	52%

***Impact of soil salinity in the study area*:**

Both groundwater and soil salinity have severe impact on the environment of studied areas. For groundwater salinity exceeding 3.0 dS/m, farmers cannot grow crops in the winter season well. The maximum yield and yield loss of non-rice crops due to salinity were evaluated by Mondal (2001), as shown in Table 2. Also, Das and Mehrotra (1971) conducted a research on the yield loss of modern varieties of rice due to salinity, as reproduced in Table 3. Salinity intrusion due to sea level rise will decrease agricultural production by unavailability of fresh water and soil degradation. Salinity also decreases the terminative energy and germination rate of some plants (Rashid *et al.*, 2004; Ashraf *et al.*, 2002).

From a study conducted by the World Bank (2000), the increased salinity from a 0.3-m sea level rise will cause a net reduction of 0.5 million metric tons of rice production. Sea level rise will also affect coastal agriculture, especially rice production in Bangladesh in the following two ways: (i) the salinity intrusion degrades soil quality that decrease or inhibit rice production and (ii) hence, the rice fields are converted into shrimp ponds, total production of rice decreases due to decreased rice field areas (Rahman *et al.*, 2000).

Chiba University, Japan